COATING THICKNESS MEASUREMENTS AND DEFECT

CHARACTERIZATION IN NON-METALLIC COMPOSITE MATERIALS BY

USING THERMOGRAPHY

A Dissertation

by

HONGJIN WANG

Submitted to the Office of Graduate and Professional Studies of
Texas A&M University
in partial fulfillment of the requirements for the degree of

DOCTOR OF PHILOSOPHY

.

Chair of Committee,	Sheng-Jen Hsieh
Committee Members,	Hong Liang
	Sy-Bor Wen
	Jun Zou
Head of Department,	Andreas A. Polycarpou

December 2016

Major Subject: Mechanical Engineering

ABSTRACT

Thermography is a non-destructive testing method (NDT), which is widely used to guarantee the quality of non-metallic materials, such as carbon fiber composite, anti-reflection (AR) film, and coatings. As other NDT methods do, thermography determines a defective area based on the signal difference between suspected defective areas and defective-free areas. Two unavoidable effects are decreasing the credibility of thermography detection: one is uneven heating, and the other is lateral diffusion of heat. To solve this problem, researchers have developed various reconstruction methods. Restoring methods are known to have the capacity to reduce the effect of heat-flux lateral diffusion by de-convoluting a point spread function either along a temporal profile or a spatial profile to process captured thermal images. These methods either require pre-knowledge with depth or are not effective in detecting deep defects. Here we propose a spatial-temporal profile-based reconstruction method to reduce the effect of uneven heating and lateral diffusion. The method evaluates the heat flux deposited onto tested samples based on surface temperature gathered under ideal conditions. Then the proposed method is tested in three real applications – in defect detection on semi-transparent materials, on semi-infinite defects (coatings) and anisotropic materials. The method is evaluated against existing methods. Results suggest that the proposed method is effective and computationally efficiently over all the reconstruction methods reviewed. It reduces the effect of uneven heating by providing a good approximation to the input heat flux at the ending image of the sequence.

TABLE OF CONTENTS

LIST OF FIGURES

LIST OF TABLES

CHAPTER I

INTRODUCTION AND BACKGROUND OF THE RESEARCH [1]

The chapter here introduces the background of the research, including the significance of the problem, the nature of the research, including the definitions of terms used in thermography, and an overall outline of following chapters. The entire chapter is divided into three sections: the first section provides the importance of the research by introducing the cost issues in inspection, production yield and product failures due to insufficient coating and minute defects; the second section introduces the nature of thermography detection and coating measurements and the definitions of terms in thermography, and explains the terms used in the research; and the last section will illustrate the overall outline of the rest part of the proposal.

---

[1] Part of the data reported in this chapter is reprinted with permission from:
(1) "Non-metallic coating thickness prediction using artificial neural network and support vector machine with time resolved thermography" by Hongjin Wang, et.al. 2016. *Infrared Physics & Technology*, Volume 77, July 2016, Pages 316-324, ISSN 1350-4495,Copyright [2016] by Elsevier B.V. or its licensors or contributors
(2) "Using active thermography to inspect pin-hole defects in anti-reflective coating with k-mean clustering" by Hongjin Wang, et.al , 2015. *NDT & E International*, Volume 76, Pages 66-72, ISSN 0963-8695, Copyright [2015] by Elsevier B.V. or its licensors or contributors
(3) "Evaluating the performance of artificial neural networks for estimating the nonmetallic coating thicknesses with time-resolved thermography" by Hongjin Wang, et al, 2014. *Optical Engineering*, Volume 53, 083102 , Copyright[2014] by SPIE
(4) "Comparison of step heating and modulated frequency thermography for detecting bubble defects in colored acrylic glass" by Hongjin Wang and Sheng-jen Hsieh. *2015 Proceeding of SPIE 9485 Thermosense: Thermal Infrared Applications XXXVII*, Page number 94850I, Copy right[2015] by SPIE

I.1 Background of the research

Non-metallic materials are widely used in the industries. Their qualities are required to be strictly controlled. Comparing to metallic materials, non-metallic materials may have several advantages: easy to be visual transparent; resistant to the chemical corrosions and less density [1-3]. For example, polymeric coatings are widely used in packaging [4, 5] Another example is anti-reflection film, which usually made by adhering several non-metallic layers together. Carbon fiber composites are used in aircrafts, wind turbines and cars as structure materials to resist pressure, static or dynamic loads, twists, or other forces.

Failure of these materials to function as designed brings in losses in both money and human lives. Defects can also be very expensive for the producers. Federal Aviation Regulations require all the product providers to report defects in components (FAR Part 21 section 3). Failing to do so will cost the provider double charges. Thus, there certainly is a justifiable reason to investigate defects detection in carbon fiber composites. The pin-hole defects in optical films like Anti-reflection films invokes customer complaints. The coating thickness is well controlled in order to make sure the coated materials functions as required. Therefore, to reduce the cost due to production failure, a testing in quality control process is applied before the products follow into markets.

Non-destructive testing (NDT) is developed in order to save cost on quality control since the product yields are decreased by destructive testing methods [6]. NDT allows the manufacturers to low down the cost of quality control since the nondestructive detection will not reduce the tested products' qualities after tests. What's more, nondestructive

detection will allow in-situ detection during manufacturing process so that technicians may find abnormal processes at an early stage.

The basic principle behind a successful NDT technology is that the defect will change the amplitude, the frequency, the phase angle of the inputted wave-like signal by reflection, refraction or, even, absorption. The wave-like signal used in the NDT can be optical light, x-ray, elastic wave, ultrasound wave, ultra-violent wave, alternative electrical field, magnetic field and infrared wave.

Eddy currency and magnetic detection are widely used in the pipeline corrosion due to its cost efficiency. However, the main problem of these two technologies is that they have limited capacity in defect shape recognition.

The optical inspection uses optical light as a source. The basic idea that surface cracks, scratches, voids or surface unevenness will change the original routine of the light source. The defect will be detected by using a CCD camera or optical radiometer to capture the transmitted light or reflected light. Once there is a defect like cracks, scratches, voids or surface unevenness, either the transmitted light intensity or reflected light intensity will change in certain degree [7]. This technology is the most frequently used in the manufacturing industrial. The both the spatial resolution and the time resolution of optical inspection will be very high. With an optical microscope, the spatial resolution of a visual camera can get to 0.2μm [8]. The data sampling speed can exceed Gb/s. Apparently, the visual inspection will be able to detect the defects buried in the tested sample only if the material is transparent. Or else, the optical inspection can just focus on the surface defects, which may be not sufficient for the early age detections.

Radiographic Testing (RT), a nondestructive testing method of hidden defect detection, uses the ability of short wavelength electromagnetic radiation (like X-ray, γ Ray) to penetrate various materials. This technology predicts the hidden flaw size and location by analyzing changes of intensity of the transmitted short wavelength electromagnetic radiation at the back of tested material. The Radiographic testing can easily find out voids in the material [9 , 10]. However, others failed in detection of voids with this method. Evermore, the X-Ray detection may have difficulties in find the cracks, de-bonding or delamination in the composite material [10, 11]. In 2003 review, Carrivea still considers X-Ray has limited capacity in the de-bonding detection [11]. Yet, in a recent new review, it seems that the CT technology advanced radiographic testing by improving its crack detection with help of dyes [12]. Yet the largest problem which prohibits X-ray testing applied in the industrial is the cost and the potential hazard it may bring in due to radioactive ray leakage.

Ultrasound inspection methods are commonly used NDT testing methods and has an advantage over radioactive method by getting free of potential radioactive pollution because ultrasound, in fact, is wave-like acoustic energy with a frequency exceeding the human hearing range. It is possible to get a high resolution by choosing high frequency (100 kHz to 40 MHz). In ultrasonic testing, acoustic waves are injected into the material or component as an examination source and then a transmitted / reflected beam is used to monitor the resonance of ultrasound in the material.

Ultrasonic inspection works well in the metallic material inspection. It can be used to detect almost all kinds of defects [10]. With the help of ultrasonic guided wave, this

method can travel along the tested material, especially metal with a long distance [13]. Ultrasonic inspection can achieve a high resolution, but the resolution which it can achieve quite depends on the model chose [13]. Another very interesting application of guided wave analysis can be considered for coated structure detection, for example, steel in the concrete or steel coated with tars. This ability will save money by reducing the process to remove 'coated materials' [13]. However, as the attenuation for ultrasound is relative high in the composite material, the contrast between the defect and the surrounding material is relative low during ultrasonic inspection for these materials. Thus, to obtain an acceptable contrast between defects and surroundings, the frequency of input ultrasonic wave should exceed 1MHz for defects smaller than 0.1mm. Frequencies much lower than "0.1 MHz would not produce wave interactions appropriate to the specimen microstructure" [14]. Also, Gros has reported C-scan limited in find out delamination buried in 1.1mm Carbon fiber composite [14]. Obviously, ultrasonic inspection gets problem with small defect detection in the polymeric composite materials.

Thermography is a non-destructive method concerned with the measurement of temperature on the surface of the zone. The basic idea of thermography is that the heat conduction in the solid material similar to the wave propagation under a certain input thermal wave. The magnitude of the input may follow a step function, a pulse function, and a periodic sinusoidal, or other kinds of function of time. According to whether an extra thermal excitation is applied to the tested sample, thermography technologies can be categorized as passive thermography and active thermography. Passive thermography, as its name indicated, does not apply extra thermal source to heat up test samples but just use

the source emitted by the samples themselves. Thus, it can just be applied to inspect objectives with a temperature different from the ambient, like a tank, a vehicle engineer or a human body. On the other, active thermography employs an external heat source for excitation. Hence, it can inspect many objects without an internal heat source.

According to the shape of the excitation wave, active thermography can be classified as pulsed thermography, modulated thermography and time-resolved thermography. Pulsed thermography uses an instantaneous heat pulse, like an optical laser pulse, a flash lamp pulse or an eddy current pulse, as a heat source [14]. Due to the instantaneous heat flux, heat cannot conduct in an equilibrium way. The surface temperature of a semi-infinite slab with a thickness at L will change following the error function format. The detection capacity of pulsed thermography depends on the changing rate of input energy. So does that of time-resolved thermography. Yet, the time-resolved thermography also requires the surface temperature change larger than the noise equivalent temperature of the camera. Thus, the detection capacity of time-resolved thermography also depends on input energy amplitude. On the other, the pulsed thermography and time-resolved thermography has limited capacity in detecting large depth to diameter ratio defects [15-17].

The costs of different non-destructive testing methods require significantly different for the same type of defects in different materials due to the prerequisite of NTD methods: a 'sharpen boundary', should lies between the defective area and the bulk material. The 'sharpen boundary' here refers to an interface where the penetrable mediums (like ultrasonic wave in ultrasonic NDT, visual light in visual inspection, radiation in X-ray,

Table I.1   Different NDT coating measurement instruments

production name	principle	accuracy	adaptive range	substrate material	price($)
Defelsko	Magnatical +eddy currency	± (0.01 mm + 1%) 0 - 2.5 mm, ± (0.01 mm + 3%) > 2.5 mm	thick coatings	all metals	1175
ultra-sonic gauge for non-metal substrate	Ultrasonic	± (2 um + 3%)	1-1000 micron	non-metal	2695
PosiTector® 6000 N1 S	eddy currency	±(1 um + 1%) 0 - 50 um, ± (2 um + 1%) > 50 um	non-conductive coating 0-1500	conductive substrate	695
Filmetrics	optical/spectrum analysis		silica	unknown	>20K
Fluorescent X-Ray Coating Thickness Gauge	x-ray	50nm			>20K
Atd Mask-Less Direct Write Too	Light source: KrF Lase	80nm	not specified	not specified	>20K

Table I.2   Comparison of various NDT methods' capacity in detecting defects in Carbon fiber reinforced Composite

	Time(per round)	delamination	voids	cracks
Eddy current	1 s (50 mm by 50 mm)	Yes, for shallow mounted ones in weak conductive TRM (CFRP) [18]	NA	Yes, for near surface ones in weak conductive TRM (CFRP) [18]
Magnetic	NA	NA	NA	NA
NDT optical inspection	NA	NA	NA	NA
Radiographic Testing	10-150 min	limited, only with dyes [10, 12, 18,19]	Yes[10, 12, 18-20]	Acceptable [10, 12, 18-20]
Ultrasound	$10\mu m$ per 0.3mm by 0.3 mm	Limited in finding delamination near holes [21, 22]	Yes, limited while Vc<1% [23, 24]	Limited, rare industrial application[10, 19]
Thermography	1s-160s	Yes, good for finding delamination near holes , [25-28]	Yes comparable to Ultrosonic, [29]	Yes [2, 30-33]

heat flux in thermography) will be absorbed, reflected or refracted significantly. For example, Ultrasonic inspection usually works well in the metallic material inspection [11]. However, as the attenuation for ultrasound is relative high in the composite material, the contrast between the defect and the surrounding material is relative low during ultrasonic inspection for these materials [11]. The Radiographic testing can easily find out voids in the material [9, 19]. Evermore, the X-Ray detection may have difficulties in find the cracks, or delamination without dyes in the composite material since these defects cannot reduce enough irradiance [10, 19]. A comparison of the cost of non-destructive testing methods in non-metallic coating thickness measurement is compared in Table I.1. It can be observed thermography is an attractive NDT method.

Thermography is an attractive NDT method for non-mantellic materials [34-36]. Current non-destructive technologies cannot address all the issues in the non-metallic material testing and measurements [11]. Table I.2 summarizes the capacity of several NDT methods carbon fiber composite defect detection. For example, the capacitive of automotive optical inspection to detect pin-holes in visual transparent is limited because the method can only generate a small contrast between the health area and the defective area [37]. Moreover, this small contrast may be degraded by the inappropriate view angles [38].

I.2 The nature of detection and coating thickness measurements with NDT

In general, defect detection is a process to identify and locate an area where the measured targets behaves differently from the major part of the tested samples under a designed excitation, (like radioactive waves, eddy currents, magnetic field, visual lights

and acoustic waves) since a type-X defect may generate a clear 'tested boundary '(an interface where difference in the measured targets between the top surface of the defect and the adjacent bulk material is large enough to be captured.) The basic principle behind a successful NDT technology is that the defect will change the amplitude, the frequency, the phase angle of the inputted wave-like signal by reflection, refraction or, even, absorption. The wave-like signal used in the NDT can be optical light, x-ray, elastic wave, ultrasound wave, ultra-violent wave, alternative electrical field, magnetic field and thermal wave[39-41].
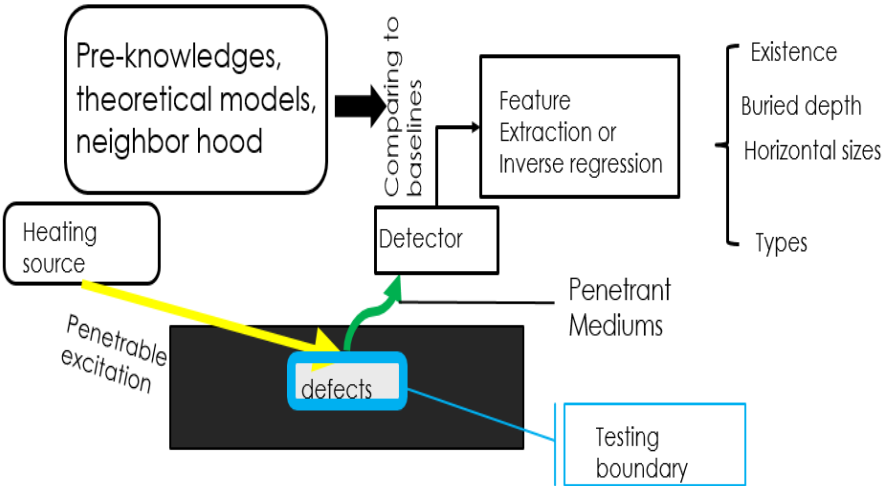
Figure I.1   The nature of non-destructive defect detection

Several major components are included in a thermal NDT defect detection process (As shown in Figure I.1) (also, known as thermography detection, suggested by Vavilov [42]): "

- modelling defect situations and optimizing both heating and data acquisition,

10

- choosing a proper hardware (both an IR imager and a heater),

- conducting a test and collecting an IR image sequence,

- preliminary data processing (correcting object 3D shape, enhancing signal-to-noise ratio and making decision on presence/absence of defects in tested areas),

- .advanced data processing—determine the existence of defects by producing binary maps of defects and evaluating defect parameters in lateral dimension and in depth, and

- making a final decision on sample quality by applying approved acceptance/rejection criteria".

As Bues [43]and Vavilov [42] have pointed, NDT usually cannot provide a direct images about the defects. In fact, the measured data from thermography is thermal responses. These responses may not reveal the depth information of defects directly. Therefore, a model which predicts the thermal response changed by defect of type x is required. Inspection patterns then need to be formulated both for contrast enhancement and for determining the existence of defects.

Coating thickness Measurement can be treated as a special case of defect detection where the defect size buried h depth beneath the coating surface with semi-infinite size. By having this point, the steps to detect defects with thermography can be used to measure coating thickness with some modification.

Criteria (Baseline) must be set up before detection is conducted in order to determine the non-defective area and defective area. A cured composite part may contain a multitude of internal defects [44]. These internal defects can be voids, delamination, fiber mis-

orientations, and non-uniform fiber distribution [44]. It's believed that a good quality polymeric composite will contain voids whose volume is less than 0.5% volume of the total. Wisnom also points out the length of the defect will affect the strength of the material significantly [45]. His experiments show that the inter-laminar shear strength reduces between 8% and 31% when discrete defect growth from 0.28 mm diameter void to 3 mm long crack. The delamination area should be controlled within certain proportional of the total area [44]. However, there are no standards for the critical size of delamination in Carbon fiber composite [44]. For the pin- holes in the AR films in the display application, The pin-hole defect size is one of the dominant factors in quality control of anti-reflective coating. Up to authors' knowledge, a lot of AR manufacturers for viewing application set a limitation about the maximum tolerable pinholes sizes [46-49]. A commonly acceptable pinhole size for AR film designed for displays is set to be 0.1mm [46-49]. Thickness of thin coating is a quite important quality control in many industrial fields, such as pharmacy, aerospace, power generation, electronics industrial and others [4, 31, 50, 51]. And this technology is gaining importance due to the narrowing market and competition [52]. The current common used non-destructive detection method and classified them according to their principles: a) Geometric part measurement ,b) Gravimetric analysis ;c)Pull-off force analysis; d) Acoustic emission analysis; e)Ultrasonic impulse echo analysis; f) Magnetic induction analysis; g)Eddy-current analysis; h)X-ray fluorescent analysis; i)Beta-Backscatter analysis; j)X-ray diffractometer.

I.3 The overall outline of the dissertation

In summary, the cost of the production failures, the cost of product yields and the cost of inspection technics motivate the author to conduct the current study in the non-metallic coating thickness measurement and material defects detection by using thermography. The nature of NDT detection and coating thickness measurement has been introduced with details on the critical size of the defects. In the next chapter, a detailed review about thermography is given. It has been shown that building analytical models and formulating inspection patterns are necessary steps for thermography to characterize defects and measuring coating thickness. A comparison between the existing models for thermography and between commonly used inspection patterns will be given in the next chapter. By reviewing these, the gap between the current state of thermography and the need of improvements will be illustrated. Based on the review, the research question, the objectives, the research scopes and detailed research task will be discussed and displayed in Chapter III. From Chapter IV to Chapter VII, the theory background, proposed methodology and experimental results will be described and discussed. In Chapter 8, the summary of finding and conclusions will be displayed and future work will be discussed.

CHAPTER II

LITERATURE REVIEW

The chapter here provides readers a detailed review about the current state of three major components in thermography technics: the analytical models for the thermography and inspection patterns currently used. By reviewing these components, the gap between the current methods and the needs will be discussed and displayed. The need of proposed objective will be reinforced.

II.1 The models for thermography defect detection and coating thickness measurement and their applications

The section reviews the evolution of the models for thermography defect detection and the coating thickness measurement. The models are compared with each other based on their complexity and their assumptions. The reasons behind the evolutions are presented. Therefore, the needs and the direction of evolution of thermography in the future will be discussed.

The first trials in using thermography to detect discontinuous in materials can be dated back to late 1970s. Henneke's work [53] should be recognized. They have conducted a serial conceptual experiment to demonstrate the possibilities of thermography to detect various defects in both isotropic and anisotropic material. Their studies have displayed different thermal patterns of cracks, internal defects due to loads and delamination. However, the study did not provide an efficient theory to predict thermal patterns for different defects. Later on, various experiments have been applied to different materials

to explore the capacity of thermography. Early researchers usually simplify the thermography detection process into 1D heat conduction problems in homogenous materials with one side as adiabatic surface under a pulse excitation [54]However, the model follows the experimental results in limited conditions: when the pulse is shorter than dozens of milliseconds; the defect is relatively large that the lateral heat conduction can be neglected; the heat leakage from the bottom surface can be neglected and the surface heat excitation is absolutely homogenous. Vavilov [42] has figured out, the heat leakage from the bottom surface should not be neglected when the tested sample is thermally thin. A comprehensive review of the models used in thermography has been summarized in Vavilov's reviews [42, 55]. A supplementary comparison is listed in Table II.1. It can be found that early researchers prefer to use a simple 1D models since the defects in tested samples are relatively large or say thermally different from the bulk. Later researchers like Ludwig[56]figured out that the 3D effect of refractive thermal waves cause a large bias in lateral dimension between the predicted one and the directly measured value, and, therefore, have added an approximated thermal diffusion due to refraction although the estimation is semi-empirical. Baddour [57] later developed a model which can be adaptive to both pulse thermography and lock-in thermography. However, the model is built to evaluate the diffraction effect and no experiments have been conducted to demonstrate the capacity of the model. Although researchers have noticed that the homogeneous heating source is not realistic in the thermography and the detection results are degraded by them, its effect is not included or discussed in the model for thermography.

Table II.1   Comparison of different heat conduction models used in thermography

Author	Mode	Temporal profile of excitation	Dimension considered	Blurred by 3D	Assumptions 3D diffusion	SNH
Steinberger [54]	Transmit.	Pulsed	1D -trainsient	Yes		No
Busse [58]	reflective	pulse	1D transient	Yes	No	No
Mulaveesala [35, 59-61]	reflective	MF	1D transient	Most of	No	No
Avdelidis [62]	reflective	Pulse/ step	Lumped transient	Yes	No	No
Petal [63]	reflective	Lock-in	1D transient	Yes, 3D of defect	No	No
Osiander [64]	reflective	Pulse/ step	1D transient	Yes	No	No
Ludwig[56]	reflective	pulsed	1D transient with lateral adjust	Empirical corrected	yes	no
Vavilov [55]	reflective	pulsed	1D	*	Yes	no
Baddour [57]	reflective	Pulsed/lock-in	3 D	corrected A	Yes	NA
Erturk [65]	Refl./tran.	constant	3D	Corrected iterative inverse	Yes	NA
Vavilov [66, 67]	Refl./tran.	pulse	1D/2D/3D	No	Yes	no

However, it does not mean that no researchers have noticed the negative effect of non-homogeneous heating nor methods to reduce this effects are not attractive. In fact, a lot of trials have been conducted to reduce the negative effect due to non-homogeneous heating by developing different informative patterns. These efforts will be summarized and discussed in the next section.

II.2 The current detection patterns in thermography and their limitations

The section here discusses the existed efforts in formulating informative patterns in thermography and their limitations. The need in enhancing the contract between defective area and non-defective area and in extracting characteristic information drives researchers to generate various detection patterns. Based on the principle behind formulating informative patterns, the patterns can be classified into two categories: the empirical informative patterns, and the model-based patterns. The empirical informative patterns are generated empirically based on the statistical characters in the surface temperature response. Some of the variances used as input to the patterns are determined empirically. Principle component analysis [68] is a typical empirical informative pattern. Compared to the empirical informative patterns, the model-based empirical informative patterns are generated based on the heat conduction mechanisms. The current researchers are more interested in the second kind of patterns since they can be adaptive to those problems which share common principles with each other.

Vavilov [42, 55] has compared and summarized several commonly used informative patterns: temperature increments, early detection correlations, phase-grams. The table one compares several commonly used informative patterns which are not discussed in

17

Vavilov's review dated at 2002 and summarized in Table II.2. Including those discussed in Vavilov's review, there are no model-based patterns can be applied to all kinds of excitation. That is to say, the current model-based informative patterns are highly depending on the assumptions made in the thermography models from which they are derived. An informative pattern may not be able to be adaptive to other thermography technics rather than the one it derives from. For example, Shepard's Logarithm reconstruction [69] is developed based on the pulse excitation assumption and it will violate its basic if the pattern is applied into either step heating thermography or lock-in thermography, let along the FM thermography. Besides, the Hilbert analysis developed by Mulaveesala [61] is based on the assumption that FM thermography is applied.

Although researchers have generated several informative patterns based on 1D models to eliminate the effect of non-homogenous heating sources, the efficiency of these informative patterns should be examined carefully. For example, although conventional phase images are believed to be independent of heat excitation spatial distribution, several sets of experiments shows that its independence is conditional to lock-in thermography [70, 71]. The figures from Almond's[70, 72] researches show that the spatial diffusion in the conventional phase image blurred the contrast between defective area and non-defective area. The coefficient images seem to eliminate the non-homogenous a little bit. However, the coefficient is determined semi-empirical by fitting the temporal temperature by a polynomial curve. Author previous researchers also demonstrated that the non-homogenous spatial distribution of heating source cannot be neglected for deeply buried defects. Therefore, a theoretical model to understanding the non-homogenous distribution

18

of the heating source should be developed in order to figure out a widely adaptive method to eliminate the negative effect of non-homogenous heating.

Another issue in the thermography is that the lateral diffusion caused by limited defect size biased from the 1D assumptions. As a result, the 1D defect size assumption caused a difficulty in characterizing the lateral size small defects. Recently, researchers began to consider formulating informative patterns with 3D diffusion effects involved in [17, 57, 66, 73]. Omar[17, 74] has developed a deconvolution filter based on the numerical simulation of surface temperature under a Gaussian point heat conduction. Holland [73] reconstructed the method with a heat conduction model based on uniform heating deposited on thin slabs to mock the detection process with vibro-thermography. The existing researches show that by doing so, the detection capacity of thermography has been enhanced in detecting and characterizing defects with significant lateral diffusion. However, they are aiming at to discuss effect of the deconvolution methods in reducing the lateral heat diffusion effect. The discussing about the effect of deconvolution effect on identifying solid area under non-homogenous heat is missing. Moreover, iterative method requires the measured surface temperature to be noise free. And the diffractive analysis requires an experimental demonstration. Comparing to Laplacian models, the 3D Fourier analysis proposed by Baddour [57] provides a stable numerical solution. Also, several kinds of lateral effect restoring filters (mentioned as restoring filters) are developed for vibrothermography [73, 75].

The spatial profile based patterns refers to those patterns which are used to determine the defective or non-defective area, or the depth of the defects based on the thermal distri-

Table II.2   The current reconstruction methods to enhance the contrast beyond Vavilov's summarization

Author	Method	Excitation	Dimension	Approximation	Bottom
Maldague [76]	Pulsed phase	pulse	1D		adiabatic
Shepard [69]	Synthetic Signal Processing /Logarithm	Pulse excitation	1D		Semi-infinite
Mulaveesala [61]	Hilbert analysis	Modulated Freq.		Digital -> continuous	Semi-infinite
Lugin [77]	Iterative echo comparison	Pulse			Adiabatic
Almond [78]	Temporal polynomial coef.	Lock-in	1D		Semi-infinite
Omar[54]	PSF deconvolution	Pulse	3D		Numerical kernel
Holland [73]	Heat source intensity estimation	vibrothermogrpahy	3D	Noise free	
Rajic[68]	Principle component analysis	pulse	Empirical		
Baddour [57]	3D Fourier transform	Lock-in	3D		Semi-infinite
Delpueyo [75]	Derivation of Gaussian filter	Mocked vibrothermography	2D		

bution along the surface rather than the time. Bisson [79] has shown a method based on the spatial thermal profile to estimate the diffusivity of a slab. Bison [80]has summarized several spatial-based thermography method to determine the thermal diffusivity of thin coats or slabs . As Bisson has pointed out, the method using spatial distribution of thermal profile requires neither the initial time nor the beam radius. However, the detraction should not be neglected during the method [79].

II.3 The evaluation system of detection patterns

There are three indexes to describe an image. The first one is the standard deviation over the entire image. It measures the uniformity of the back ground. If the variation in a processed image is only caused by noises in the background, its overall standard deviation in the non-defective area will be relative small. Inversely, if the image's main index varies along spaces (distributed non-homogenously), the overall deviation of the non-defective area will be relatively large.

The second one is signal-to-noise ratio. It is one of the most important index to evaluate the efficiency of the inspection patterns [81]. However, in the previous work, the noise is evaluated based on uniform background, which is hard to obtain in the step heating thermography. The common definition of the signal to noise ratio (SNR) can be written as:

$$SNR_G = \frac{\sum\sum I(i,j)^2}{[\sigma(N(i,j))]^2} \qquad \text{(II.1)}$$

Where $I(i,j)$ is the signal values inside the defective area well the $\sigma(N(i,j))$ is the standard deviation of noise. In the previous studies, the standard deviation of the noise is determined based on the variation of the Intensity in the non-defective zone (sound zones)

[17, 81, 82]. However, by such a definition, there are two challenges which should be solved in or der to obtain a good approximation to the real standard deviation of the noise: first, the intensity in the sound zones should be uniform; moreover, the solid zone need to be known. Identification of Sound zone identification is a problem in thermography [81].

Basically, there are two methods to identify the sound zones: empirical method, and model based method. In the empirical method, the solid zones are arbitrarily determined. However, it doesn't mean unjustified. The method is suitable for testing subjects with complex inner structures [17]. In the model based method, the zones whose thermal responses are strictly stick to a pre-known thermal model are considered as solid zones. However, when the heating source is not uniform and the thermal properties of the material is anisotropic, the method will cause problems [81, 82]. Shepard et al. [83] has developed a method, later called "self-referencing thermography" [84, 85], to automatically detect defects. The method do not need any prior knowledge of the existing non-defective areas but whose principle lies in comparing the temperature rise of a given pixel to the mean of the pixels in its neighborhood. The so-calculated contrast is compared to the noise evaluated for the neighborhood. Based on the principle, another index to evaluate the SNR, called local SNR is introduced. The definition of local SNR has the exactly the same expression as show in Equation (II.1), the differences are lies in the way to evaluate the signal level and the standard deviation of noise level: the standard deviation of noise is evaluated based on the overall standard deviation of the neighbor-hood standard deviation. The method gives best estimation to the real noise level when the spatial intensity variance

rate are uniform over the entire field of view. In another words, the local SNR works well for small variance across the image.

II.4 Summary

Based on the literature review and comparisons between different models for thermography and between existed informative patterns in thermography, several points can be summarized:

- As the requirements on thermography increased, the lateral non-homogenous distribution of thermal excitation cannot be neglected,

- The non-homogeneity affects the identification of the solid zones as well, which is important in the certainty of defect detection.

- There are several widely-adaptive inspection time-resolved patterns like surface temperature, phase angle, and temperature temporal derivatives, however, they are all highly influenced by the spatial distribution of thermal excitation.

- There is a need in developing a model-based pattern which can be applied to all kinds of excitation and be independent to lateral distribution of thermal excitation.

- In the depth characterization, the time-resolved patterns requires high sampling rate

- Space-resolved patterns has been demonstrate to be attractive in thermal diffusivity measurement with thermography.

CHAPTER III

THE OBJECTIVE AND DETAILED TASKS

Based on the literature review from the second chapter, it has been concluded that the non-homogenous heating source degrades the detection results and bring in difficulties in identifying solid zones when basing on the widely used homogenous heating source models. One draw-back of the thermography lies in the mode-based inspection patterns used for detection depends on both on the temporal profile of excitation and its spatial distribution. All the trials in formulating inspection patterns is guided by the rule that the inspection patterns of defective area should be as different from those in the healthy areas as much as they can. A homogeneous heat excitation is preferred in thermography since under this condition; the surface temperature may display most recognizable differences between the defective area and non-defective area. However, the absolute-homogenous spatial distribution is hard to available in real application and as a result, the contrast of inspection patterns between the defective area and non-defective areas are blurred with a model which excludes the non-homogenous spatial distribution effects. Based on the reviewing in the Chapter II, it has been found that although several existed inspection patterns can reduce the blurring effects due to spatial non-homogeneity of heating source, they cannot eliminated the effect of non-homogenous heating without scarifying certain detectability and are limited to the temporal excitations based on which the models are derived. If a widely-adaptive model-based pattern would be built, a better understanding in the non-homogenous effect of heating and in generating inspection patterns can be

achieved. It may be possible to find a new inspection patter which base on spatial profile to detect and characterization defects. To achieve these goals, a problem should be understood and answered first: What does the exactly role of spatial non-homogeneous excitation play on in the thermography and can a restoring inspection pattern derived based on models to improve the thermography's recolonization on the geometry dimensions of defects? To answer such a question, the thermal wave propagation mechanism need under spatial non-homogenous heat excitation should be understood. The current chapter introduces the research objective based on the question, the detailed research task.

The study is aim at understanding the effect of spatial-based inspection patterns (restored heat flux by temporal-spatial Fourier mask) in AR film defect detection, coating thickness estimation and defect characterization in carbon fiber composite.

Spatial restored patterns can be used to improve the detection by reducing the effect of non-homogenous heating and providing a method to identify solid zones in AR film defect detection, coating thickness estimation and defect characterization in carbon fiber composite.

The research is limited to study the effect of non-homogenous heating in three cases: pin-hole detection in anti-reelection film, non-metallic coating thickness measurement, and planar defect detection in CRFC. The AR film are opaque to the Long-wave IR radiance. The heat source should be located outside of the field of view in AR tests. Also, thermography works when there is a thermal boundary between the coating and substrate. The term thermal boundary means the interface where thermal properties between the

coating and the substrate are different. In coating thickness measurement, the thermal boundary lies between coating and substrate in coating thickness estimation. The coating thickness studied in this study varies from 2.5 mil to 22.5 mil since most packaging industries are interested in the coating thickness within this range [4, 5, 52, 50].

Table III.1 Research scopes of experimental design

Applications	Coating thickness measurement	Defect detections	
Bulk material	substrate	Anti-reflection film	Carbon-fiber composite
Defects/ coatings	Non-metallic paintings	Pin holes	Foreign lmplants-FEP and Teflon
Testing Method	Thermography	Thermography	Thermography
Excitation Heat			
Spatial	Spot like	Uncontrolled	Proposed to be uncontrolled or motion
Temporal	Constant within a short time	Constant within a short time	Proposed to be either Constant within a short time or Frequency modulated

These three cases are selected because the dimension of geometry characteristics are 2D, 1D and 3D respectively. The detailed scopes of the research are listed in the table above (Table III.1). In details, they are described as following:

- The Derivation of the filter based on the surface temperature in Fourier-Hankel domain and theoretical validations of the restoring kernel.

- Heat conduction theories behind thermography and Image processing

    o Methodologies: deriving and modifying the spatial patterns for pinholes in AR film

    o experiment set-ups

    o Data Process and results-- comparison the spatial patterns with temporal patterns

    o Discussing about the dimension of Sub-pixel Defect Recognition Algorithm

- The heat conduction and non-homogenous heating in non-metallic coating thickness measurement.

    o Heat conduction model for coating thickness estimation

    o Understanding how the spatial patterns varies with coating thickness theoretically

    o Set up experiments

    o Comparison the spatial patterns with existed temporal patterns

- The heat conduction and non-homogenous heating in composite material.

    o Heat conduction model for coating thickness estimation

o   Understanding how the spatial patterns varies with coating thickness theoretically

o   Set up experiments

o   Comparison the spatial patterns with existed temporal patterns

CHAPTER IV

THE DERIVATION OF THE FILTER AND THEORETICAL VALIDATIONS[1]

IV.1   Heat conduction in thermography and derivation of restored heat flux

Considering a heat flux $q(t, x, y)$ heating on the surface semi-infinite thermally isotropic block, the 3D Fourier transformed surface temperature of the bulk can be obtained by doing Fourier transform in both spatial directions and temporal direction:

$$T(\xi, 0, \omega) = \frac{q(\xi, \omega)}{k} \frac{1}{\sqrt{\xi^2 + \frac{i\omega}{\alpha}}} \qquad (IV.1)$$

, where

$$\xi^2 = u^2 + v^2, \qquad (IV.2)$$

, and,

$$T(x, y, t) = \int_{-\infty}^{\infty} \int_{-\infty}^{\infty} \int_{-\infty}^{\infty} T(\xi, \omega) \exp(iux) \exp(ivy) \exp(i\omega t)\, du\, dv\, d\omega, \qquad (IV.3)$$

α stands for the thermal diffusivity of the bulk, and k stands for the thermal conductivity of the bulk.

The Equation (IV.3) is equivalent to the convolution of thermal response under simultaneous spot heating over the given heat source:

$$T(x, y, 0, t) = \int_0^t \int_{-\infty}^{+\infty} \int_{-\infty}^{+\infty} \frac{q(x', y', t')}{\sqrt{4\pi\rho c(t-t')^3}} \exp\left(-\frac{(x-x')^2 + (y-y')^2}{4\alpha(t-t')}\right) dx'\, dy'\, dt' \qquad (IV.4)$$

A variable, named restored pseudo heat flux (RPHF), can be obtained by doing inverse Fourier transform of the product between the 3D Transformed surface temperature response over a time t and the filter $\sqrt{\xi^2 + \frac{i\omega}{\alpha}}$. The RPHF, theoretically, is proportional to $1/k$.

The surface temperature of a coated sample under a laser spot can be expressed as Equation (IV.5) in the 3D Furrier transformed domain:

$$v_1 = \frac{\bar{q}(s,\xi)\left(1 + R\,exp\left(-2z_0\sqrt{\xi^2 + \frac{i\omega}{\alpha_1}}\right)\right)}{k_1\sqrt{\xi^2 + \frac{s}{\alpha_1}}\left(1 - R\,exp\left(-2z_0\sqrt{\xi^2 + \frac{s}{\alpha_1}}\right)\right)} \qquad (IV.5)$$

By applying the filter to the surface temperature of coated samples, a pseudo heat flux RPHF (restored heat flux) will be generated, it always equals to the convolution of heat flux and the refraction caused by the thermal boundary between coatings and the substrate when the heat flux flows out of the FOV is zero.

$$RPHF = \int_{-\infty-\infty i}^{+\infty+\infty i} e^{i\omega t} \int \frac{exp\left(-\frac{\xi^2 B^2}{8}\right)\left(1 + R\,exp\left(-2z_0\sqrt{\xi^2 + \frac{i\omega}{\alpha_1}}\right)\right)}{4\pi R^2\,(i\omega)k\left(1 - R\,exp\left(-2z_0\sqrt{\xi^2 + \frac{i\omega}{\alpha_1}}\right)\right)}\xi J_0(r)d\xi\,ds \qquad (IV.6)$$

At r=0, the pseudo heat flux can be written as:

$$RPHF(t,0) = \int_{-\infty-\infty i}^{+\infty+\infty i} e^{i\omega t} \int \frac{exp\left(-\frac{\xi^2 B^2}{8}\right)\left(1 + R\,exp\left(-2z_0\sqrt{\xi^2 + \frac{i\omega}{\alpha_1}}\right)\right)}{4\pi R^2\,(i\omega)k\left(1 - R\,exp\left(-2z_0\sqrt{\xi^2 + \frac{i\omega}{\alpha_1}}\right)\right)}\xi J_0(0)d\xi\,ds \qquad (IV.7)$$
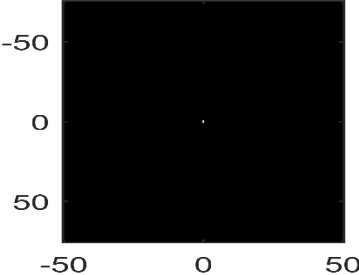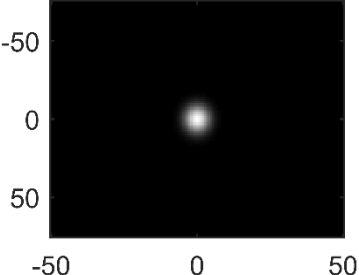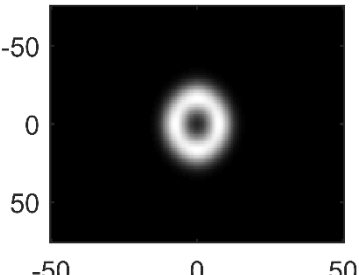
The pseudo heat flux can be normalized by dividing the pseudo heat flux at the center of laser pulse.

IV.2   Theoretical validation and effect of noises

To validate the effect of the proposed filter on restoring heat flux from surface temperature collected from a time after the zero moment when the heating begins, a set of numerical simulated surface temperature data are used. These data are simulated under several heat source with several spatial distribution listed in the table below. Several reasons makes numerical simulation rather than experimental data being used here. Comparing to experimental data, the noise numerical simulated data can be well controlled; the examined samples can be perfect in isotropic and defect-free; and the probable uncertainty brought in by thermal diffusivity can be eliminated from the numerical simulation. The tested heat flux are listed in the table below (Table IV.1). The first one is an idea point heating source which is instantaneous at moment zero. The second one is a heat sour with Gaussian spatial distribution and delta temporal profile. It mocks a laser beam heating and the third one is a circle like heat source with whose spatial distribution across the width of circle band has a Gaussian shape. Based on the theory which has been discussed in the previous sections. The surface temperature under a heat source can be calculated by convoluting the surface temperature under a delta spot pulse with the heat source. The surface temperature at 1s, 10s, 20, 30s and 40s after the heating begins are showing in the Figure IV.1. As the time goes on, the surface temperature diffuses. Even heating with a perfect spot like source, the heat will disperse and affect other areas of the material.

Table IV.1 The heat source profiles used to test the RPHF filter

Heat flux no.	Heat flux expression	Normalized spatial distribution
1	$q(x, y, t) = A\delta(x)\delta(y)u(t)$	
2	$q(x, y, t) = A \exp\left(-\dfrac{x^2 + y^2}{4\sigma^2}\right)u(t)$	
3	$q(x, y, t)$ $= A \exp\left(-\dfrac{(x - x_i)^2 + (y - y_i)^2}{4\sigma^2}\right)u(t)$ $[x_i, y_i] \in [(x_i - x_0)^2 + (y_i - y_0)^2$ $= R^2]$	
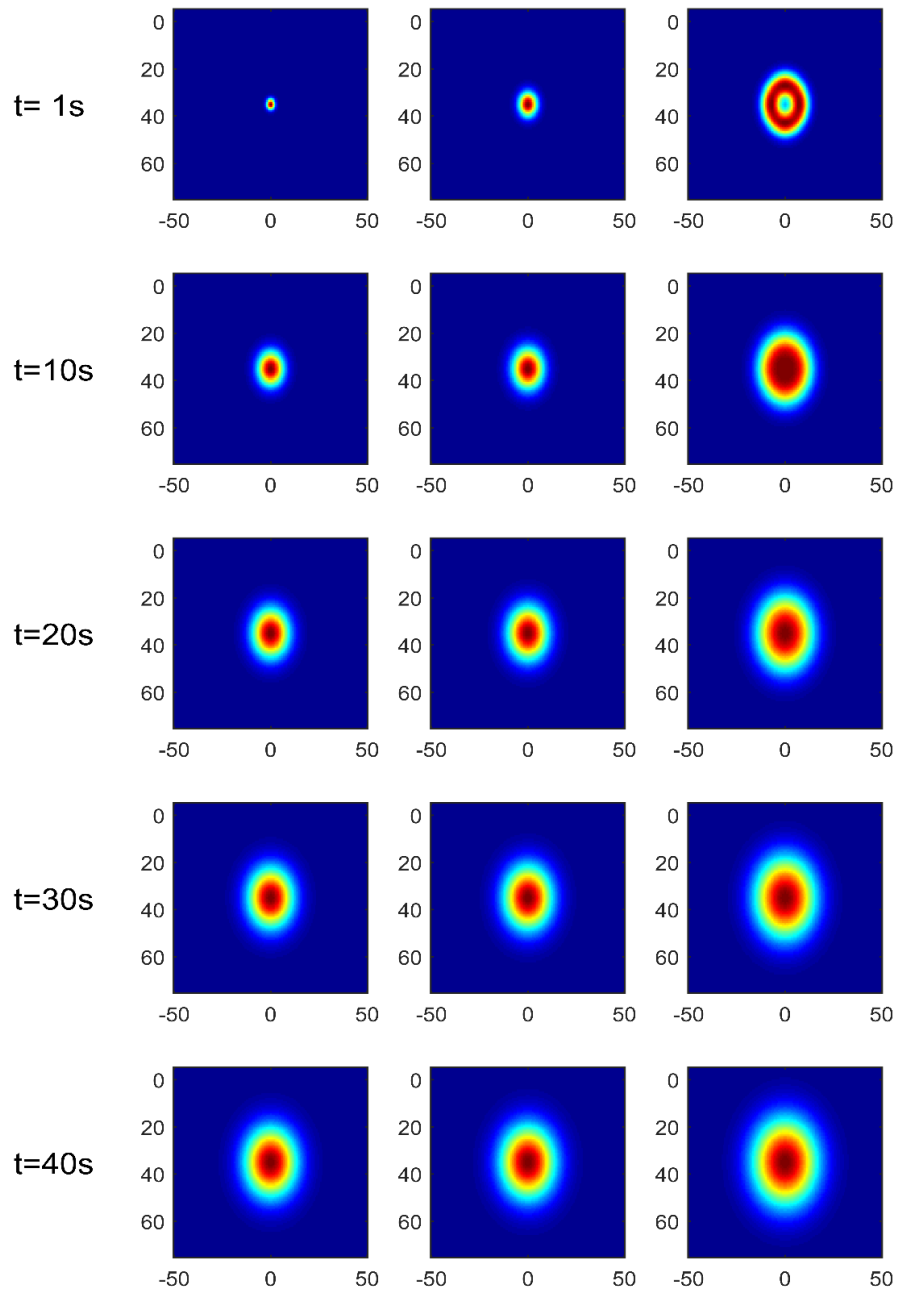
Figure IV.1 Surface temperature distribution at different time

The deconvolution filter is coded and compiled with MATLAB as MATLAB provides

a strong math library with stable FFT transform algorithms. The deconvolution results are

shown in Figure IV.2 below. It can be observed that with the proposed filter, the heat flux spatial distribution can be obtained (known as restored heat flux). Comparing both the normalized spatial profile of the restored heat flux (RPHF) and that of surface temperature to the normalized spatial profile of the heat source, it can be observed that RPHF has a spatial profile almost the same with that of heat source while surface temperature has a diffused profile.
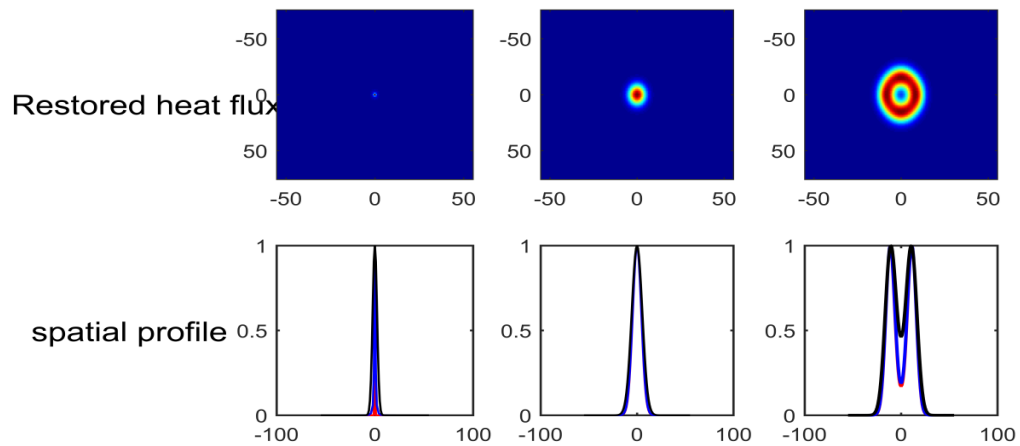
Figure IV.2 Comparison the profile of heat flux restoration (blue) with that of heat flux (red) and surface temperature (black)

However, the above results are obtained at an idea condition that no noise is shown up during data collection. In the real experiments, the Gaussian noises can seldom be eliminated from the measured surface temperature. Therefore, the effect of Gaussian noises should be discussed. The following images shows the RPHF from surface temperature under spot delta pulse with no noise, Gaussian white noise whose standard derivation at 0.01, 0.05, 0.1, 0.5, 0.9 separately (Figure IV.3). With light noise, the

proposed filter still works and the restored heat flux spot can be easily found from the image. However, when the standard derivation goes up to 0.1, it's difficult to tell the restored spot source from the noise. Thus, Gaussian blur filter should be used to reduce the standard deviation of noises in the image.
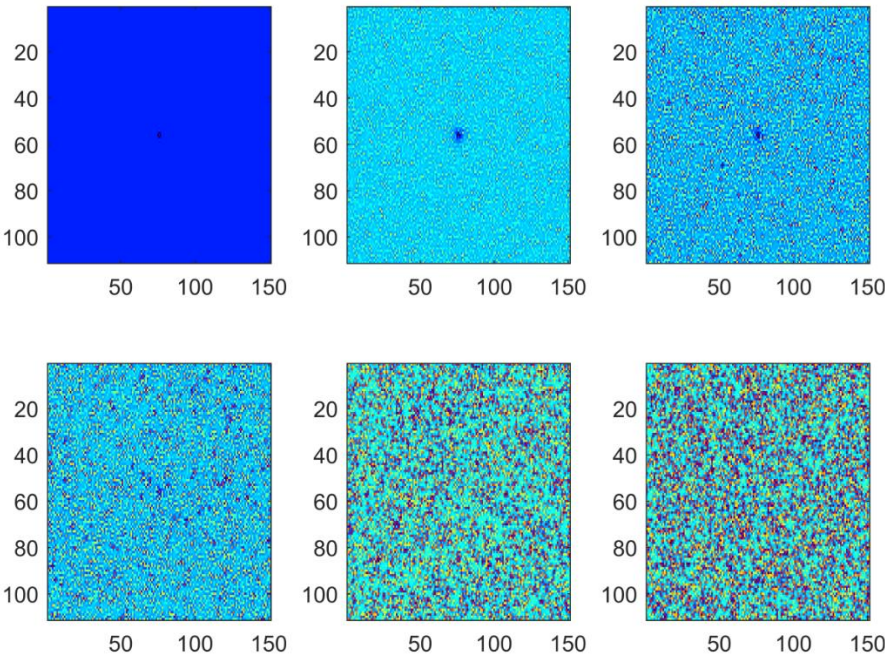
Figure IV.3 The noise effect on the RPHF (first row, left—zero noise; mid --- Gaussian noise with 0.01 std; right ---0.05 std; the second row, left—0.1 std, mid - 0.5 std, right—0.9std

CHAPTER V

THE EFFECT OF SPATIAL PROFILE BASED PATTERNS IN DETECTING PIN-HOLES ON AR FILM[1]

V.1 The theory behind detection surface defects- pinhole detection in AR film

If the heat source caused by chemical reaction, heat convection, or phase change at surface can be neglected, the heat source due to radiation can be written as:

$$S = g(r)f(d)u(t) - S_{em} + S_{ab}, \tag{V.1}$$

where $g(x,y)f(d)u(t)$ represents the heat absorbed from the bulbs across the surface at different times; S_e the emitted heat from the film; and S_{ab} the energy absorbed from the ambient.

According to the Beer–Lambert law, the volumetric heat absorption in attenuated media can be expressed as [32]

$$f(d) = \int \frac{\beta_e(\lambda)_i I_0(\lambda)}{2k_e} \exp(-\beta_e d) \ d\lambda, \tag{V.2}$$

, where β_e is defined as the effective absorption coefficient for the Anti-reflective film with thickness at d. β_e is tested based on total attenuation reflective Fourier transform Infrared spectroscope (ATR-FTIR).

---

[1] Part of the data reported in this chapter is reprinted with permission from"Using active thermography to inspect pin-hole defects in anti-reflective coating with k-mean clustering" by Hongjin Wang, et.al , 2015. *NDT & E International*, Volume 76, Pages 66-72, Copyright [2015] by Elsevier B.V. or its licensors or contributors

$$I_0(\lambda) = \frac{\varepsilon 2hc^2}{\lambda^5} \frac{1}{\exp\left(\frac{hc}{\kappa_B \lambda(\theta_s+\theta_0)}\right)-1} \qquad (\text{V.3})$$

, where h and K_B are Planck's constant and Boltzmann's constant respectively; c is the speed of light in vacuum; λ is the wave length; and the θ_0 is the reference temperature that is equal to the initial temperature of the film. It also equals to the ambient temperature.

Under the experimental conditions used in this study, the heat source is a step function of time:

$$u(t) = \begin{cases} 1 & t \geq 0 \\ 0 & t < 0 \end{cases}. \qquad (\text{V.4})$$

The heat gain from the bottom side of the film can be expressed as:

$$S_{em} = F_b(x,y)\varepsilon_e \sigma((\theta + \theta_0)^4), \qquad (\text{V.5})$$

$$S_{ab} = F_b(x,y)\varepsilon_e \sigma((\theta_{ab} + \theta_0)^4), \qquad (\text{V.6})$$

, where F_b is the view factor.

During heating, although the temperature of the AR film increases by 20°C, the heat loss due to radiation is smaller than the heat gain. The lumped temperature of the AR film can be solved by applying the Fourier transform temporally and the Hankel transform spatially

$$\tilde{\theta} = \frac{\tilde{S}(\xi,\omega)}{k_e\sqrt{\xi^2+\frac{i\omega}{\alpha}}} \qquad (\text{V.7})$$

. Transferred back to the time and spatial domain:

$$\theta = \int \frac{\beta_e I_0}{2k_e} \exp(-\beta_e d) d\lambda \int_{-\infty}^{\infty} -\frac{i}{\omega}\left[K_0\left(\sqrt{\frac{i\omega}{\alpha}}r\right) * g(r)\right] e^{i\omega t} d\omega, \qquad (\text{V.8})$$

, where $K_0(x)$ is a modified Bessel function of the second kind at zero order:

$$K_0(x) = \int_0^\infty \frac{\cos(xt)}{\sqrt{t^2+1}} dt; \tag{V.9}$$

, $*$ is the convolution operator. The temperature of the AR film is observed to increase as the film thickness decreases.

The temperature readings $\theta_{reading}$ from a bolometer infrared camera depend on both the surface temperature and the transparent radiance from an incident source for a semi-transparent film at a pixel, since the energy sensed by a single bolometer cell M is the sum of emitted radiance and transparent radiance:

$$\theta_{reading} = \Delta\theta_r + \theta_{reference} + \varepsilon_r \tag{V.10}$$

$$\Delta\theta_r = M \cdot G \tag{V.11}$$

$$G = F_b \varepsilon_e \sigma(\theta^4 - \theta_{ab}^4) + \int F_b T(\lambda) I_0(\lambda) \, d\lambda, \tag{V.12}$$

, where

$$T(\lambda) = 10^{-\beta_e d}, \tag{V.13}$$

ε_r is the random error introduced by the characteristics of micro-bolometer cell.

From Equation (V.7), it can be observed, in the thermography detection of thin film, the surface temperature of the film is a product of heat flux and the term $\dfrac{1}{\sqrt{\xi^2+\frac{i\omega}{\alpha}}}$ in the 3D Fourier transformed domain. In this equation, $\tilde{S}(\xi, \omega)$ is the 3D Fourier transform of the heat flux. By multiplying the term $\sqrt{\xi^2 + \frac{i\omega}{\alpha}}$, the Fourier transform of heat source can be restored. As the temporal profile of excitation is well controlled, it can be known that there is a defective area once its local temporal profile of excitation is different from the others.

However, the temperature reading from infrared camera is not equal to the surface temperature due to heating for pin-hole area, where the transmitted radiance cannot be neglected. For the healthy area the readings are approximated to the surface temperature since the material is opaque to the IR radiance. As a result, the deconvolution filter may be able to reduce the effect of inhomogeneity on the measured temperature in the healthy area although some side effects may be brought in by the defective area where the heat diffusion rule does not dominates.

By substituting Equation (V.7), (V.11-13), and Equation (V.8) into Equation (V.10), one can find that the bolometer readings increases as the film thickness d decreases owing to the increase in both the temperature and the transmitted radiance; in contrast, visual inspection can only detect defects based on the change in transmittance at the defect area. Moreover, the transmittance of visual light is affected little by the film thickness as AR films with thickness of the order of 100 μm are usually transparent to visual light.

IR camera readings $\theta_{reading}$ described in Equation (V.10) is smooth if there is no random errors. In other words, a harsh change in the spatial gradient of the temperature indicates the boundary of a defective area or noise at this location. However, if an uneven heating source is applied, IR camera readings $\theta_{reading}$ is uneven even though there is no random errors. Under this condition, IR camera readings $\theta_{reading}$ bends spatially following a certain curve described by Equation (V. 8-13) for non-defective areas. The unevenness of infrared readings causes a problem [2, 33, 86]. when using spatial derivations, which were used to detect the edge of defective areas [1, 30, 32] , to detect defects in the film: once the main trend of the derivations of the thermal image is close to

the level of the change caused by a defect, the defect edge may become blurred based on derivations. The contrast of thermal images is affected by non-homogenous heating Equation (V.8) [2, 33, 86]. This occurs frequently for small-sized defects. Therefore, a method to reduce the impact of non-homogenous heating on the image should be applied. The phase image is commonly used for this purpose [2, 33, 86]. However, recent numerical simulations have shown that the phase image has limited capability to eliminate the effect of a temporal step-wise non-homogenous heating source [71].

V.2 Semi-empirical polynomial approximated de-trend filter

According to an analysis of thermography processing, the trend of the thermal image can be estimated. Based on the definition of the exponential function: $\exp(x) = \lim\limits_{n\to\infty} \sum_{n=1}^{\infty} \frac{x^n}{n!}$, the temperature at a given time t can always be approximated by a high-order two-dimensional polynomial equation within a given area as $\lim\limits_{n\to\infty} \frac{x^n}{n!} \to 0$. In other words, the general trend of the Infrared camera reading can be approximated by a high-order polynomial equation. If the order of polynomial equation is high enough, the fitted model $\theta(x,y)_{vf}$ should be able to represent the Infrared camera readings $\theta_{\text{reading}}(x,y)$ [40-41]. The value of random noises should take a large portion of the residuals between the thermal readings and the fitted values:

$$\varepsilon_{\mathrm{r}}(x,y) \approx \tilde{\theta}(i,j) = \theta(x,y)_{vf} - \theta_{\text{reading}}(x,y), \qquad (\text{V.14})$$

$\tilde{\theta}(i,j)$ also refers to the de-trended temperature in the following paragraphs.

That is to say, the residuals from a good fitting model should follow normal distribution [40-42]. In this research, the average of ninth order polynomial fittings along x and y direction separately was selected to fit the image based on least square regression:

$$\theta(x,y)_{vf} = \frac{1}{2}\left(\theta_j(y)_{vf} + \theta_i(x)_{hf}\right) \tag{V.17}$$

$$\theta_i(x)_{hf} = \sum_{k=1}^{9} b_k x^k \tag{V.18}$$

$$\theta_j(y)_{vf} = \sum_{k=1}^{9} a_k y^k \tag{V.19}$$

, with constrains:

$$J_j(\phi) = \min\left(SUM\left(\left(\theta(i,j)_{Measured} - \theta_j(i)_{vf}\right)^2\right)\right) \quad j = 1,2,\dots N, \tag{V.20}$$

$$J_i(\phi) = \min\left(SUM\left(\left(\theta(i,j)_{Measured} - \theta_i(j)_{hf}\right)^2\right)\right) \quad i = 1,2,\dots M. \tag{V.21}$$

The order of the model is determined by F-test [40-41]. The sum of squares due to error (SSE) is calculated to evaluate the goodness of each fitting: $SSE = \sum_{i=1}^{n} w_i(y_i - \hat{y}_i)^2$. For all fittings for 90 tested areas in this study, the maximum SSE is 0.271. The residuals of each fittings from non-defective area are randomly positive and negative based on runs tests [87, 88]. The distribution residuals of the model were tested with Shapiro-Wilk test [89-91]. Test results shows that the residuals from the non-defective area follows normal distribution as expected. The proposed curve fitting models fit each images well.

The above process is also called de-trend filter. After de-trending, the defective pixel should be separated from the background so that the size of the pinhole can be calculated.

Sobel edge detection is commonly used to extract a defective feature from inspection images. Sobel edge detection for each thermal image can be expressed as:

$$G_i = \sqrt{G_{x,i}^2 + G_{y,i}^2} \qquad i = 1,2,3 \dots 65 \qquad \text{(V.22)}$$

$$G_{x,i} = h_x * A_i, G_{y,i} = h_y * A_i \qquad \text{(V.23)}$$

, where G_i stands for the edge detection image based on Sobel approximation for de-trended images derived at each data point, and h_x, h_y are so called Sobel kernels. A_i is the de-trended image derived at each data point.

For each single image, the Sobel edge detection algorithm detects the boundaries of defects as well as, occasionally, some noise. However, as white noise does not appear at the same pixels along time, the defect edges take heavy weights in the sum of binary images over time while the noise will be eliminated automatically. Thus, a new binary $G_{credit}(x, y)$ image is generated for each pinhole with the equation below:

$$G_{credit}(x, y) = \sum_{i=1}^{65} G_i(x, y). \qquad \text{(V.24)}$$

K-means clustering is a widely used centroid-based clustering algorithm [92, 93-95]. It aims to separate all n observations ($x_1, x_2, x_3, \dots x_n$) into k (k < n) clusters, $\{S_1, S_2, S_3 \dots S_k\}$, in such a way that each observation belongs to the cluster with the nearest mean. In other words, in k-means clustering, the square sum within one cluster is minimized:

$$\arg \min_S \sum_{i=1}^{k} \sum_{x \in S_i} \|x - \mu_i\|^2, \qquad \text{(V.25)}$$

, where μ_i are the mean points of S_i. To achieve this minimization objective, several general steps should be followed [2].

V.3 3D Fourier deconvolution filter

From Equation (V.7) ,it can be observed, in the thermography detection of thin film, the surface temperature of the film is a product of heat flux and the term $\frac{1}{\sqrt{\xi^2 + \frac{i\omega}{\alpha}}}$ in the 3D Fourier transformed domain. In this equation, $\tilde{S}(\xi, \omega)$ is the 3D Fourier transform of the heat flux. By multiplying the term $\sqrt{\xi^2 + \frac{i\omega}{\alpha}}$, the Fourier transform of heat source can be restored. As the temporal profile of excitation is well controlled, it can be known that there is a defective area once its local temporal profile of excitation is different from the others.

However, the temperature reading from infrared camera is not equal to the surface temperature due to heating for pin-hole area, where the transmitted radiance cannot be neglected. For the healthy area the readings are approximated to the surface temperature since the material is opaque to the IR radiance. As a result, the deconvolution filter may be able to reduce the effect of inhomogeneity on the measured temperature in the healthy area although some side effects may be brought in by the defective area where the heat diffusion rule does not dominates.

V.4 Experiment set-ups

All the experiments were tested with the set-up showing in the Figure V.1. A Compix 222 infrared camera (Compix Inc.) with focal plane arrays at a size of 160 by 120 pixels was set about 3.8 cm above the surface of tested samples. The detectors sensed to light ranging from 7µm to 14µm. As a result, a 0.106 mm by 0.106 mm was obtained. The camera was calibrated to achieve a noise equivalent temperature difference (NETD) at 0.1K and an accuracy at ±2ºC or 2% whichever is larger.
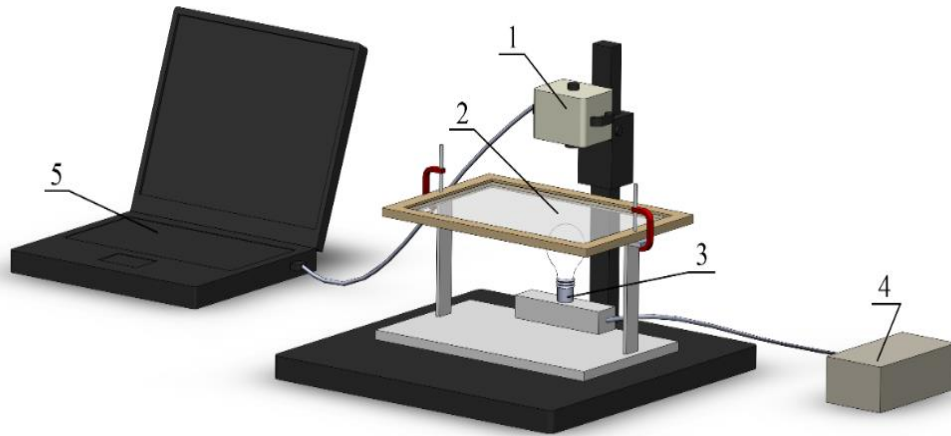
Figure V.1 The experiment set-ups. 1- Compix 222 infrared camera, 2- the tested AR film with pinhole, 3- heating bulbs; 4- the control box; 5-data analysis center

Samples were multiple-layer anti reflective coatings for flat panel display (by Dexerials Corporation). The films were at a thickness of 160 μm in average and were designed to be anti-reflective to the light whose wavelength ranges between 450 nm and 670 nm [48]. The emissivity of the Anti-reflection (AR) film was tested under ASTM code [96] with a value at 0.88.

The samples were cut by a PLS6.120D carbon-dioxide laser system (Universal Laser Systems). The size of pinholes varied from 4 mm to 0.03mm as it is shown in Table V.1. A 60 W incandescent lamp was used as heating source for the thermography testing located about 5 cm below the sample. The center of the lamp was set outside of the field of view. The lamp was kept on for 65 seconds. During this time, thermal images were taken at a rate of one frame per second.

Table V.1   The dimension of pinholes

Diameter (mm)	4	3	2	1	0.7	0.4	0.2	0.08	0.03
No.	10	10	10	10	10	10	10	10	10

V.5 Methodology of image processing

In general, several steps are applied to identify, extract, and estimate the diameter of pinhole area as it is shown in Figure V.2. The trend of original images were estimated with high order polynomial curves based on the thermal response under thermography as the method descried in section V.2. The de-trend images are prepared. Later, edge detection based on Sobel approximation was applied to extract the boundary of defective area. Considering noises in thermal images, the Sobel edge detection method was applied to each of the de-trended image. As the algorithm was implanted by MATLAB, the threshold for the Sobel edge detection is determined by MATLAB automatically [95, 97] . Later, the binary images of edges based on Sobel approximation were convoluted over each image sampled at each second after heating begins. The new images were used as the input of k-mean clustering. After that, the diameter of the defective area was measured based on the method described in Hsieh's study [98]. K-means clustering returned defective clusters and non-defective clusters as results. The coordinates of pixels in defective clusters were stored for diameter calculation.
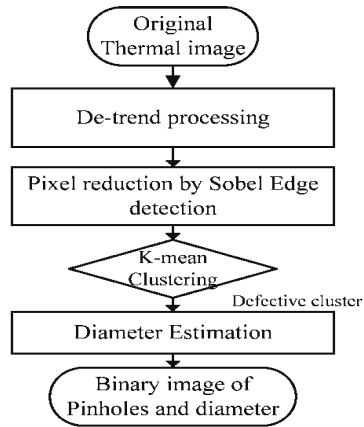
Figure V.2 The process of image processing

V.6 Data process and results

The original image is shown in the left picture in Figure V.3. Obviously, the background area was not uniform due to the non-homogenous heating. By applying the de-trend filter described in the section V.2, the background becomes flattened (uniform with noise). (The right image in the Figure V.3)
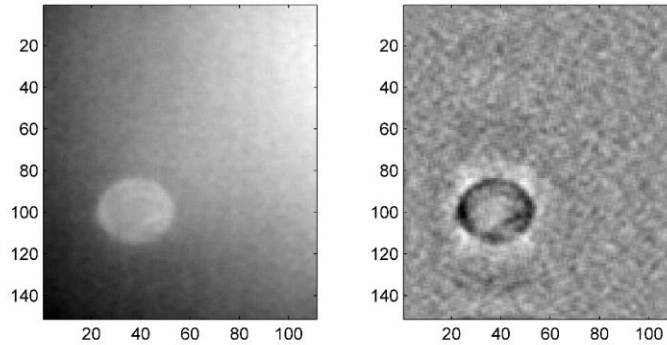
Figure V.3 The raw thermal image (on the left) and the de-trended thermal image (right)

We noted that when the defective area was relative large, (in Figure V.3, the diameter of defective area is about a third of the width of the image), the polynomial curve may followed the trend inside the defective area. However, due to the sharpen change of temperature over space, the polynomial curves was forces out of the trend at the boundaries between defective and non-defective areas. After the de-trend process, the edge of the defect area is extremely clear. The edge of the defect (the dark circle in the right image of Figure V.3) significantly differed from the average of readings of all pixels.
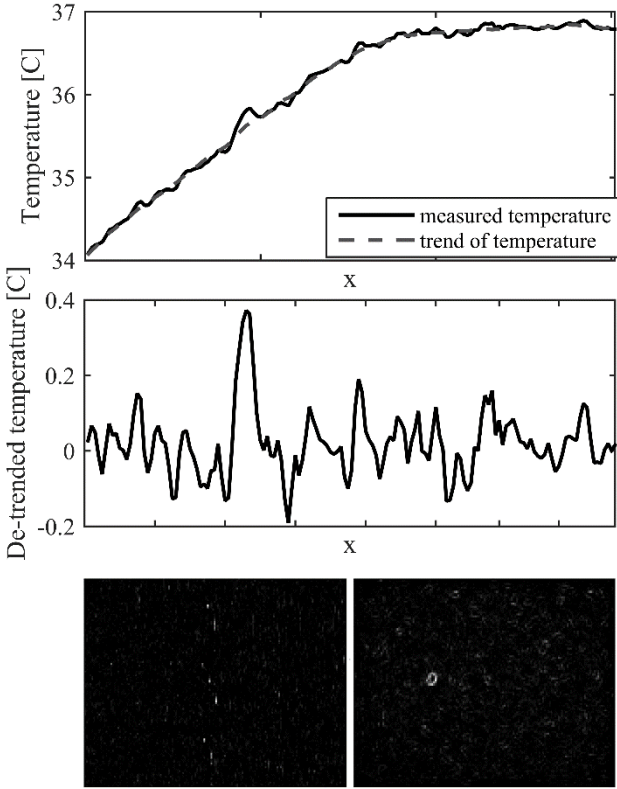
Figure V.4 The thermal profile of measured temperature vs de-trended temperature and the edge detection results of them.

The de-trend filter is essential for small size pinhole detection. The top figure in Figure V.4 compares the horizontal thermal profile of pinholes with diameter at 0.08mm and the estimated trend based on polynomial curves. Polynomial curves approximated the trend of surface temperature well. By subtracting the estimated trend from the thermal image, the de-trended thermal profile was obtained and shown in the middle figure of Figure V.4. Comparing to the variance between healthy pixels, the difference of de-trended temperature between the defective pixels and the average of healthy pixels was obviously in the de-trended thermal image (Figure V.4 middle). Our study showed the binary edge image based on de-trended temperature (Figure V.4 bottom right) showed the boundary of defect clearly while that based on original image (Figure V.4 bottom left) failed to indicate the position of the defect.
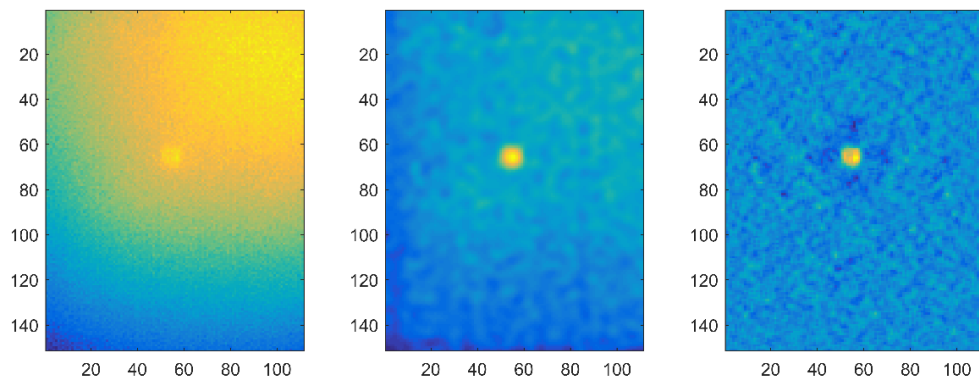
Figure V.5 The measured temperature increment (right) vs restored pseudo heat flux (left) for a sample of pin-hole 5

In the Chapter IV, it has been theoretically shown that the proposed filter can enhance the contrast between the pin-hole defects and their neighboring area. In this section, the proposed filter will be applied to the thermal images gathered from thermography

detections on the AR film. The figure below (Figure V.5) compares surface temperature

at 65seonds (right) with the restored heat flux at the same time (Left). It can be seen that

the restored heat flux gives a better vision contrast.
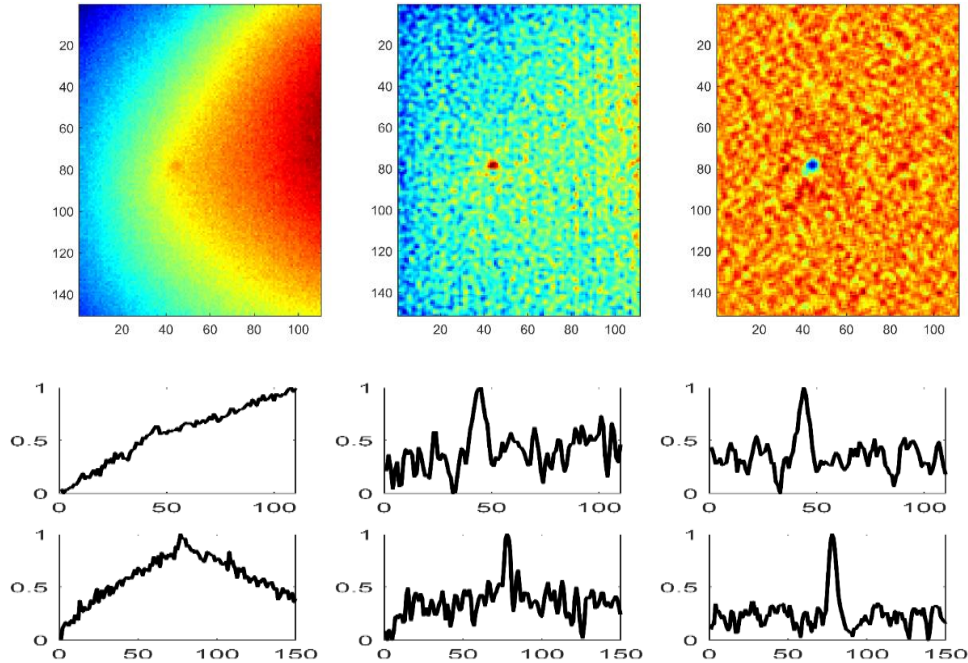
Figure V.6 Comparison between de-trended data (left column), restored heat flux (mid column) and measured surface temperature increment (right column) in color map (first row), profile across the defect horizontally (mid row) and vertically (bot row) based on a sample with pinhole 6

Figure V.6.gives a comprehensive comparison between the empirical de-trending

(first rows left), the restored heat flux (first row middle) and the surface temperature (first

row right) at 65s for the pinhole 6, whose diameter is 0.2 mm. The second row and the

third row exhibit the horizontal and the vertical line profile across the defect. The empirical

de-trending filter gives the best spatial contrast. It can been seen that after de-trending, the

background   area   only   contains   noises   and   the   defective   signal   soared   out   of   the

background noise. With the proposed filter, the restored heat flux can be obtained. Comparing to the normalized surface temperature increment (NSTI), the restored heat flux image gives a better contrast between the defect and its neighboring area although the restored heat flux images did not a noise-only background as the de-trending filter did. Due to the proposed restore filter is derived based on the model for heat conduction in a semi-infinite area, the filter created aliases at the boundary of the images when the field of view is smaller than the thermal desperation area. In all the 9 by 10 samples examined in the study, the aliases do not degrade the contrast between the defect and its neighboring area.
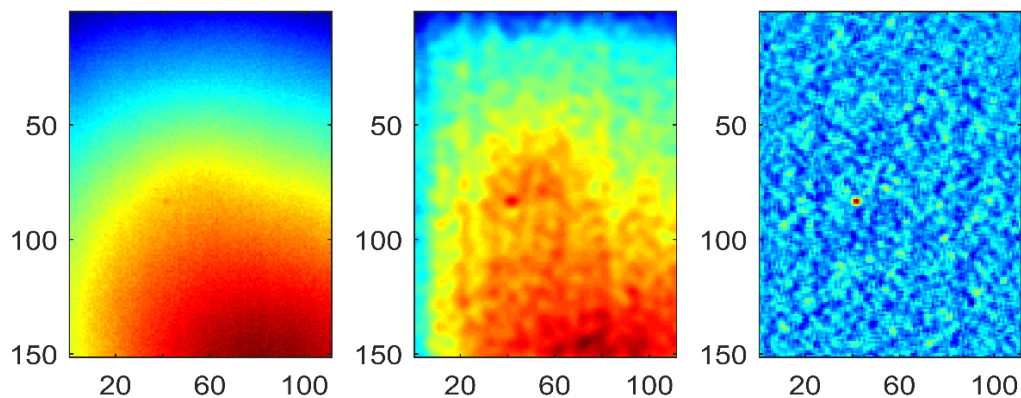
Figure V.7 Comparison between de-trended data (left column), restored pseudo heat flux (mid column) and measured surface temperature increment (right column) in color map (first row), based on a sample with pinhole 9

The de-trend filter, RPHF filter is essential for small size pinhole detection. Figure V.7 and Figure V.8 show the results of de-trending filter, RPHF and surface temperature for one of the pin-holes with diameter at 0.03 mm. The two binary images are the edge detection result based on RPHF image (left) and de-trended image (right). In this sample,

it looks like that the RPHF image has a better local signal to noise ration than the residual images and the NSTI image. It can be seen that with Restored heat flux image, the edge is detected for the detective area while it fails based on the de-trended data. However, the effect of the filters should be measured quantitatively. Figure V.9 shows that with a complex geometry, RPHF forms better than de-trend data since the latter one will bring in a distortion at non-defective area
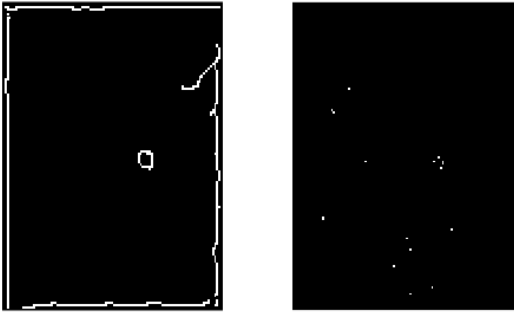
Figure V.8 Edge detection result based on RPHF (left) and de-trended data based on one of the sample with pinhole 9
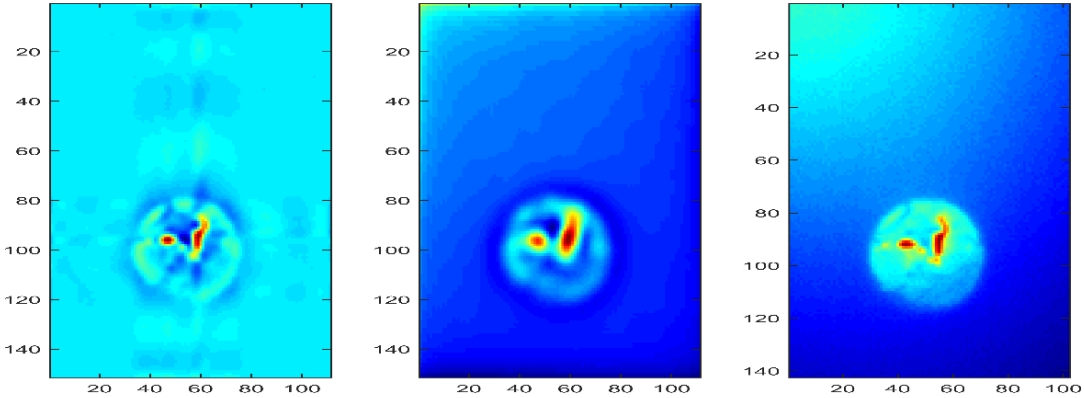
Figure V.9 Comparison between de-trended data (left), RPHF (mid) and measured surface temperature increment (right) for pinholes with complex geometries

Figure V.10 compares the standard deviation for the non-defective area over the entire field of view (STD over FOV). The solid line are the means of STD over FOV based on ten samples for each kind of pinholes. It can be observed that the processed data (both RPHF and the de-trended data) exhibit a good uniformity in the back ground while the NSTI images exhibit a large variation over the FOV. In the examined cases, the uniformity of the background in RPHF is comparable to those obtained based on de-trending process.
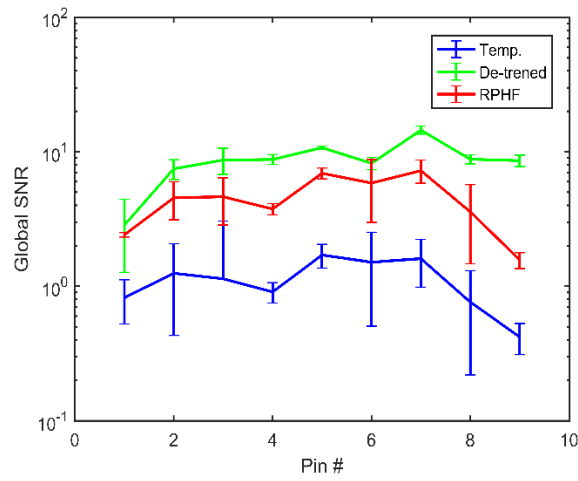
Figure V.10   Comparison of STD for overall FOV

The second criteria introduced in is the global SNR over the entire image. The criteria is defined as following:

$$SNR_G = \frac{\sum \sum I(i,j)^2}{\left[\sigma\big(N(i,j)\big)\right]^2} \tag{V.26}$$

, where $I(i,j)$ is the signal values inside the defective area well the $\sigma\big(N(i,j)\big)$ is the standard deviation of noise. In the study, the $\sigma\big(N(i,j)\big)$ for all the three methods are evaluated based on the overall standard deviation of the images values. By such a method,

the evaluated variance of noise in the de-trended data are the one most approximate to its true value in all the three method since the background of the de-trended images are noises. On the other side, the standard deviation of noises may be overly estimated in both RPHF and NSTI since they contains index variations into noises variation as well.

To give a better measurement of the SNR in the NSTI and RPHF, another criteria is introduced in: local signal to noise Ration , which has the same formula as the global one but uses local standard deviation to measure the defective area's local contrast

$$SNR_l = \frac{\sum \sum_w I(i,j)^2}{[\sigma(N_W(i,j))]^2} \tag{V.27}.$$

The signal is measured based on the variances between the normalized detecting index in defective areas and its local average within the windows. The comparison results based on local SNR are shown in Figure V.11.
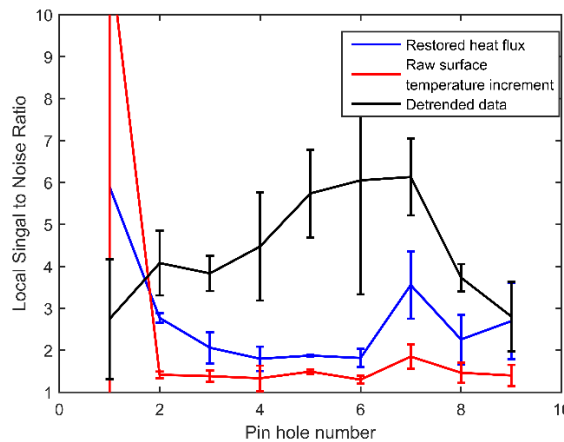
Figure V.11   Comparison of local SNRs

Although the de-trended method seems provide the best SNR among the three method, however, to calculate the de-trended data, is very time consuming. The MATLAB needs about 4 minutes to compute the de-trended filter based on the data from MATLAB

performance evaluator. And it just takes less than 1 second (0.239s) to compute the restored heat flux. Moreover, the restored heat flux images give a better performance in false positive/negative error test. (As shown in Table V.2) Also, it has been found that de-trended method may give a false alias when the defect shape is complex while the restored heat flux did not.

The calculated pinhole diameter based on thermography was illustrated in the Table V.3. Obviously, diameters estimated by the proposed method responded to the variance of pinhole diameter for those greater than 0.2mm. However, pinholes whose diameter smaller than 0.2m is detectable but not recognizable based on the method described here since they are smaller than one-pixel. For the pinholes smaller than 0.2mm, the infrared camera can just reveal them as a 0.2mm diameter holes in the image, with a predicted diameter at 0.27 mm. At the same time, the estimated size of pinholes whose diameter is greater than 0.2mm approximate to the named defect size. The difference between the average of estimated diameter and the named diameter for those 0.03mm pinholes can be as large as 700%. However, this number drops down to 3% for the pinholes with diameter at 4mm. For pinholes whose diameter is varying from 0.2mm to 1mm, the estimated diameter is always about 25%-33.3% larger than the named diameter in average. Besides, in all the 90 test, the proposed method predicted pinhole diameter greater than the actual sizes. The standard deviation for the estimated diameters of pinholes at 0.03mm was 0.004mm; that for pinholes at 0.08mm was 0.0165mm; for pinholes at 0.2mm was 0.015mm. The algorithm estimates the multiple-pixel defects with an acceptable accuracy. However, it

overate the diameter of sub-pixel defects. Therefore, an algorithm to recognize the subpixel defects should be developed and described in the next section.

Table V.2   False negative error and false positive error for each pinhole

RPHF

Diameter (mm)	4	3	2	1	0.7	0.4	0.2	0.08	0.03
Tested times	10	10	10	10	10	10	10	10	10
False positive	0	0	0	0	0	0	0	0	0
False negative	0	0	0	0	0	0	0	1	1

NSTI

Diameter (mm)	4	3	2	1	0.7	0.4	0.2	0.08	0.03
Tested times	10	10	10	10	10	10	10	10	10
False positive	0	0	0	0	0	0	0	0	2
False negative	0	0	0	0	0	0	0	0	2

De-trend

Diameter (mm)	4	3	2	1	0.7	0.4	0.2	0.08	0.03
Tested times	10	10	10	10	10	10	10	10	10
False Positive	0	0	0	0	0	0	0	0	2
False negative	0	0	0	0	0	0	0	0	2

Table V.3   Estimated diameter (est. dia.), their standard deviation (std. of est. dia.) and average estimation bias based on algorithm

Pinhole dia. (mm)	est. dia. (mm)	Std. of est. dia. (mm)	Average Bias (%)
4	3.91	0.25	-2.17
3	2.96	0.06	-1.48
2	2.17	0.27	8.67
1	1.16	0.13	15.91
0.7	0.89	0.07	26.50
0.4	0.53	0.05	33.32
0.2	0.25	0.02	26.42
0.08	0.26	0.02	227.59
0.03	0.27	0.00	801.25

V.7 Discussions on the dimension of sub-pixel defect recognition

The sub-pixel defect can just irradiate part of a pixel or irradiate 2by2 pixel partially. Therefore, the measured temperature from the infrared camera will be underrated. For a sub-pixel defect to be recognized from thermal image, the temperature change caused by the defect should be greater than the noise equivalent temperature.

An interest phenomenon were observed during experiment. The pinhole area did not illuminate the FPA detectors as soon as the heating source turned on. Instead, even the

largest defect took about 10 seconds before it become recognizable from the thermal image. The time required by sub-pixel defects may longer than large defects. The image below comparisons the time required to show 0.2 mm pinholes (lager than IFOV) and that for 0.08mm pinholes and 0.03 mm (smaller than IFOV). The tests were conducted nine times on pinholes with diameter at 0.03mm, 0.08mm and 0.2 mm separately. The y axil showed the time after the heating source had been turned on. After the defect were recognized according to the method described in the section above, the significance of the defect at each sampling point was determined by the Sobel edge detection algorithm. The brightness in Figure V.12 shows how much percentage of the defect boundaries were detected by Sobel operator at each sampling point for each samples. That is to say, if a pure white bar were seen in a trial at some sampling point that means a complete boundary was shown up at that time in that trial. A conception called critical time is introduced in here. It is defined as the first time, 70% of a defect edge can be observed continuously for 5 seconds. The research shows that the critical time for edges of the 0.2mm pinhole are no later than 20 seconds. It required 25-35 seconds for pinholes with diameter from 0.08mm to get 70% of their edges continuously detectable on the thermal image. However, the edges of 0.03mm pinholes may appear earlier than those of 0.08mm pinholes but late than those of 0.2mm pinholes.
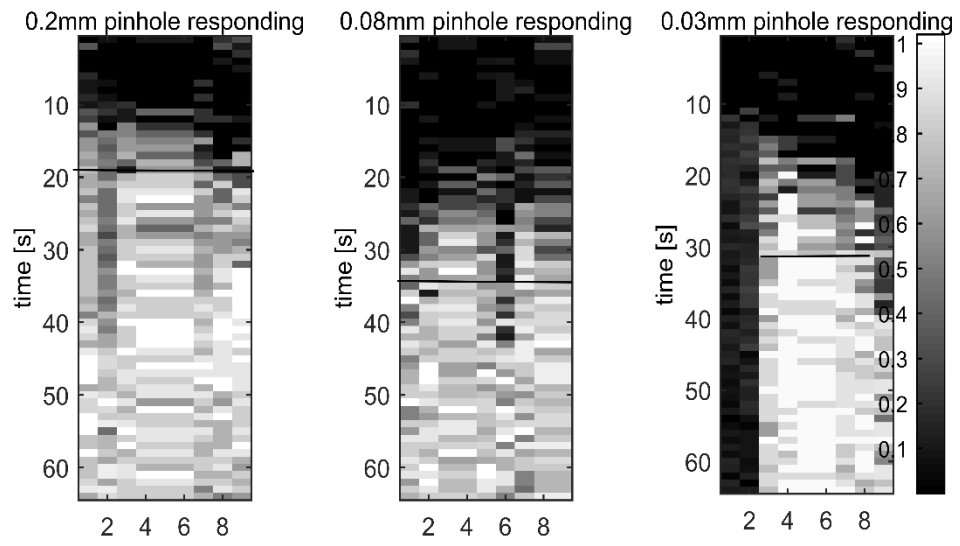
Figure V.12 Time sequence for appearance of defect boundary in thermal image

CHAPTER VI

THE HEAT CONDUCTION AND NON-HOMOGENOUS HEATING IN NON-METALLIC COATING THICKNESS MEASUREMENT[1]

VI.1   The theory behind thickness characterization

The v_1 can be solved expressed as Equations (IV. 5) for the coating under a laser spot shooting (check Appendix A for further information):

$$v_1 = \frac{\bar{q}(\omega,\xi)\left(1 + R\,exp\left(-2z_0\sqrt{\xi^2 + \frac{i\omega}{\alpha_1}}\right)\right)}{k_1\sqrt{\xi^2 + \frac{i\omega}{\alpha_1}}\left(1 - R\,exp\left(-2z_0\sqrt{\xi^2 + \frac{i\omega}{\alpha_1}}\right)\right)}$$

, where $R(\xi,s) = \frac{\sqrt{\xi^2 + \frac{i\omega}{\alpha_1}} - \chi\sqrt{\xi^2 + n^2\frac{i\omega}{\alpha_1}}}{\sqrt{\xi^2 + \frac{i\omega}{\alpha_1}} + \chi\sqrt{\xi^2 + n^2\frac{i\omega}{\alpha_1}}}$, n is the thermal diffusivity ratio between the

substrate and coating $n = \sqrt{\frac{\alpha_2}{\alpha_1}}$, χ for a thermal conductivity ratio of $\chi = \frac{k_2}{k_1}$. The

above result is consistent with those of previous studies [99-101]. The subscript 1 and 2 stand for the coating material and the bulk material separately; z_0 is the thickness of the coatings.

---

[1] The data reported in this chapter is reprinted with permission from:
   (1) "Non-metallic coating thickness prediction using artificial neural network and support vector machine with time resolved thermography" by Hongjin Wang, et.al , 2016. *Infrared Physics & Technology*, Volume 77, July 2016, Pages 316-324, ISSN 1350-4495,Copyright [2016] by Elsevier B.V. or its licensors or contributors
   (2) "Evaluating the performance of artificial neural networks for estimating the nonmetallic coating thicknesses with time-resolved thermography" by Hongjin Wang, et al, 2014. *Optical Engineering*, Volume 53, 083102 , Copyright[2014] by SPIE

For the laser spot shining constantly over time, $\bar{q}(s, \xi)$ can be expressed as Equation (VI.1) if light penetration through the coating surface is neglected [32, 34]:

$$\bar{q}(\omega, \xi) = A \frac{1}{2i\omega} \exp\left(-\frac{\xi^2 B^2}{8}\right) / 4\pi B^2 \qquad \text{(VI.1)}.$$

When the filter has been applied to the gathered surface temperature, a coating thickness modified Restored heat flux can be observed. It equals to the convolution between the original heat flux spatial profile and the coating thickness factors

$\dfrac{\left(1 + R\,exp\left(-2z_0\sqrt{\xi^2 + \frac{i\omega}{\alpha_1}}\right)\right)}{\left(1 - R\,exp\left(-2z_0\sqrt{\xi^2 + \frac{i\omega}{\alpha_1}}\right)\right)}$. In another world, it can be expected that coating thickness can be

revealed from both the spatial profile of surface temperature and that of restored heat flux.

To examine the effect of variances in coating thicknesses on surface temperatures under general conditions, a non-dimensional analysis is conducted. When introducing a 'root' thickness on the order of the coating thickness, several non-dimensional variables can be defined:

$$\xi^* = z_r\xi, \; s^* = \frac{sz_r^2}{\alpha_1}, \; zn = \frac{z_0}{z_r} \sim 1, \; r^* = \frac{r}{z_r}, t^* = t\alpha_1/z_r^2 \,. \text{ If a 'root' temperature is}$$

defined as: $T^0 = \dfrac{A}{4\pi B^2 z_r k}$, a non-dimensional temperature level can be defined as: $T^* = T/T^0$. According to this definition, non-dimensional temperature levels are independent of thermal properties but depend on thermal conductive and thermal diffusivity ratios. By adding the above non-dimensional to Equation (VI.2), the following is obtained:

$$T^*(r^*, t^*) = \int_{-\infty-\infty i}^{\infty+\infty i} \int \frac{\exp\left(-\frac{\xi^{*2}B^2}{8z_r^2}\right)\left(1 + R\exp\left(-2zn\sqrt{\xi^{*2}+s^*}\right)\right)}{s^*\sqrt{\xi^{*2}+s^*}\left(1 - R\exp\left(-2zn\sqrt{\xi^{*2}+s^*}\right)\right)} \xi^* J_0(r^*\xi^*)d\xi^* \; e^{\frac{\alpha_1}{z_r^2}s^*t} ds^* \quad \text{(VI.2)}$$

Figure VI.1 shows non-dimensional surface temperature changes with non-dimensional time. The substrate exhibits a stronger thermal conductive capacity level than that of the coating. Rather, $\chi > 1$ ($\chi = 5$) and n<1 (n=0.5). The thickness root is 2 mil (50.2 μm) at the same level for most protective or non-conductive coatings [102, 103]. When the substrate is more conductive than the coating material, the surface temperature increases as the coating becomes thicker. Equation (VI.2) shows that a surface temperature increment caused by a 10% thickness change in the coating can be sensed by a NET at 0.1K IR camera with a laser spot power level at an order of 1 mW and with a spot diameter of 2 mm.
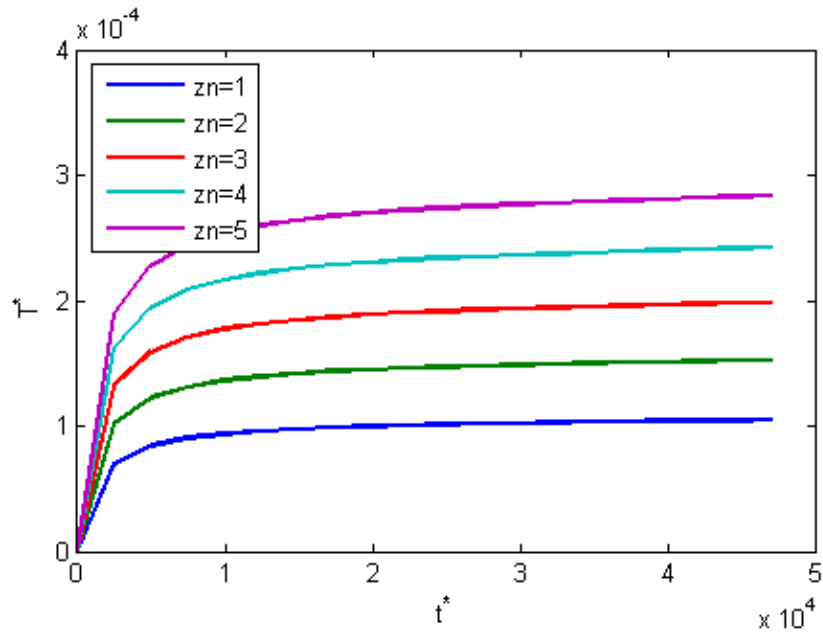
Figure VI.1 The non-dimensional temperature T^* vs. non-dimensional time t^*

Figure VI.2 shows that non-dimensional temperature varies with the thermal diffusivity ratio. The thermal diffusivity ratio increases by 0.1 for each line in the direction shown in the figure. As the thermal diffusivity ratio approaches a value of one, non-

dimensional surface temperature changes caused by the thermal diffusivity ratio are small. Non-dimensional surface temperatures are nearly doubled when the thermal conductivity ratio decreases from 0.2 to 0.1.

In a summary, if it's required to build up a correlation between the surface temperature and the coating thickness, either the problems should be transformed into a domain that the relationship between transformed surface temperature and the coating thickness can be approximated by a basic function; or non-linear regression models should be introduced in. Although high spot energy is preferred to obtain a good sensitivity to the coating thickness in the thermography, to avoid surface melting for coatings at 120 micrometre thick, the spot energy should be controlled with in 30-50 mW.
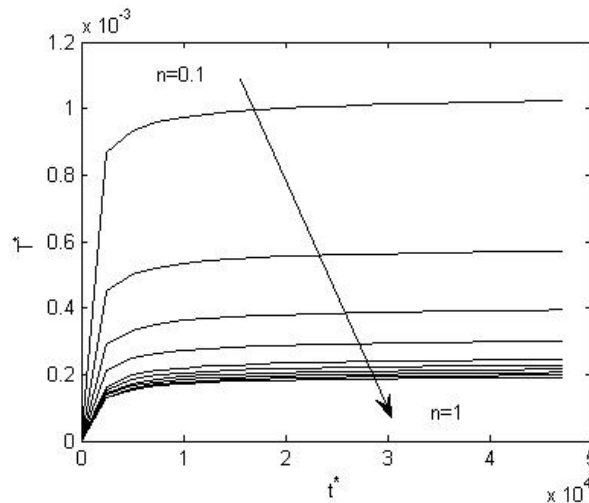
Figure VI.2 The non-dimensional temperature T^* vs. non-dimensional time t^* changes with different thermal diffusivity ratios

VI.2   Experiment set-up

Sixty-one sets of experiments on paint-coated samples were conducted to collect data and to establish regression models. Samples were tested on the test rig shown in Figure

VI.3. A BWF-1-785-450E model laser was used as a heating source. The laser reached a maximum output of 50 mW. To generate results comparable with those of previous studies, the same r experimental set-up used in previous studies was used in the present study [19].
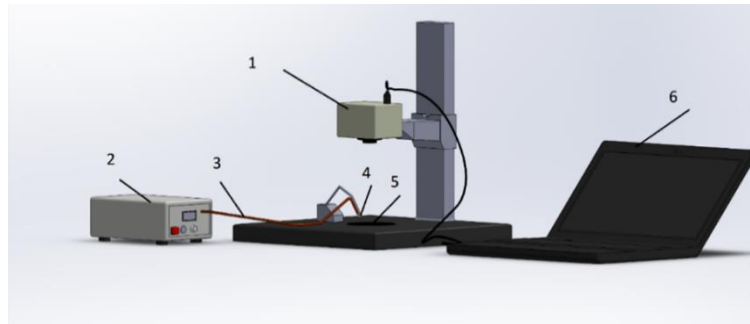
Figure VI.3Experiment set-ups 1- Compix 222 infrared camera; 2- laser emitter; 3- optical fiber; 4 --laser terminator; 5- tested samples

Substrates of the sixty-one samples were made from the same tin steel foil material with a thickness of 7.5 mil±0.3 mil (190.5μm±7.62μm). KRYLON black carbon paint was used to coat the samples owing to its widespread industrial use and re-printability. To further demonstrate the Capacities of the proposed method in estimating coating thicknesses, we divide the 61 paint-coated samples into four groups based on their coating thicknesses: 2.5 mil, 7.5 mil, 12.5 mil and 22.5 mil (63.5μm to 571.5μm). Variances and the number of samples in each level are listed in the table below (Table VI.1). Samples in a certain level are designed to represent a particular coating thickness. However, manufacturing processes causes coating thicknesses to vary according to a particular coating thickness. However, the nominal standard variance is controlled within 1.6 mils

(as shown in Table VI.1). All the coating thicknesses are examined by a G-mouth micrometre with a resolution at 0.1mil.

Table VI.1 Coating thickness of paint-coated samples for model training

Nominal coating thickness (mil)	2.5	7.5	12.5	22.5
Nominal standard variance	0.5	0.9	0.8	1.6
Number of samples	15	15	15	16
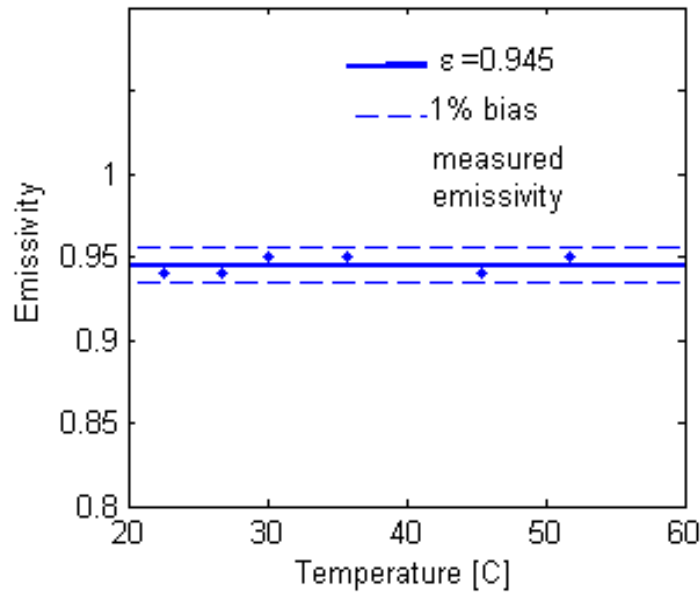
Figure VI.4 Tested painting emissivity according to ASTM standard E1933

The output laser power amplitude was set to 85% of the maximum output to prevent detection surface damage. During each measurement, samples were heated for 60 s. The entire process was recorded using a Complex 222 model infrared camera. Thermal images were taken at a rate of one frame per second. The spatial resolution of the camera was set

to 160*120 pixels. The accuracy of the camera was set to ±2ºC or 2% (whichever was higher). The NETD value was set to 0.1K. The emissivity of the black paint was measured according to ASTM Standard E1933[92]. The coatings were heated up by a Tokai Hit OLYMPUS, Shizuoka, Japan thermos-plate for 20 min to ensure that both the thermocouple and the coating samples were in a steady state. The measured emissivity was 0.945 ± 0.05 (as shown inFigure VI.4). At the start of the heating process, the heat source may have been unstable.

VI.3   Thermography data analysis

Sixty-one sets of data were collected for the paint-coated samples. Differences between the samples of varying coating thickness (solid lines) and variance levels among the samples of the same coating thickness (error bars) are shown in Figure VI.5

Figure VI.5 shows the maximum surface temperature increment for samples with different coating thickness. The solid lines stand for the average maximum surface temperature increment while the short vertical bars presents the deviations among different samples with the same nominal coating thickness. The T test results show that means of samples with the same nominal coating thickness are different from those with a different coating thickness with a significant greater than 90% when the heating is longer than 15 seconds.Samples with 2.5-mil coatings generated the lowest temperature increments of all four groups of samples of different coating thicknesses (Figure VI.5). The temperature increment at each time point increased as its coating thickness increased, as predicted by Equation (VI.2). The standard deviation among samples with 2.5 mil coating thicknesses was found to be relatively smaller than that of the samples with thicker

coatings. It is evident that the standard deviation recorded under increasing temperatures is larger than that recorded for data collected during the stable period. Camera behaviours can serve as a reasonable explanation: infrared staring arrays integrate sensed lights into temperatures over a certain period. Thus, more severe temperatures challenge camera capacities.
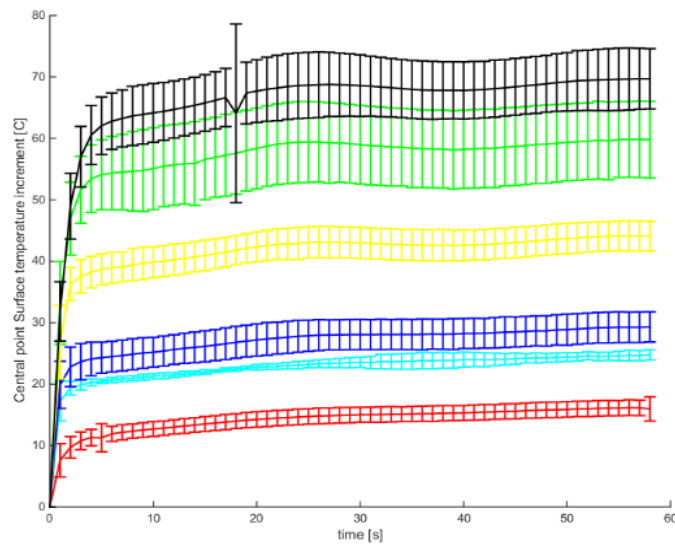
Figure VI.5 The maximum temperature increment

However, if the amplitude did not hold constantly for each testing, then the surface temperature of samples with same coating thickness may differ from each other significantly. And it would be hard to see the difference between the means of maximum surface temperature increment gathered from samples with different coating thickness (as shown in Figure VI.6 right). Comparing to the maximum surface temperature increment, the spatial patterns—normalized restored heat flux spatial profile and the normalized

66

spatial profile of surface temperature increment is independent from the heating source amplitude. It can be observed that with the heat flux restoration filter, the spatial profile has one more inflection point than the surface temperature profile.
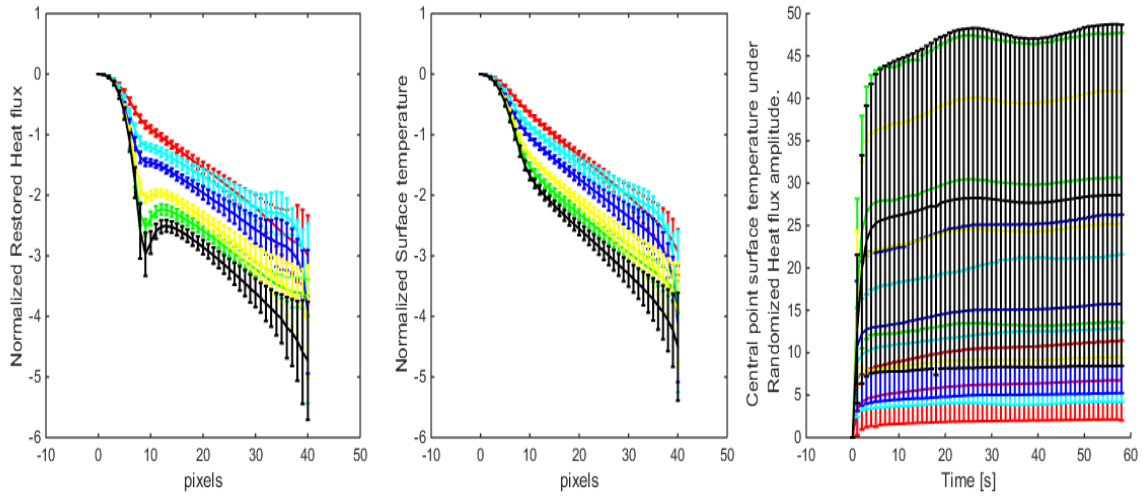
Figure VI.6Normalized spatial profile of restored heat flux (left) vs. that of surface temperature increment (mid) and the maximum temperature increment (right)

VI.4   Regression model set-up

The relationship between surface temperatures and coating thicknesses is implicit and inflexible during industrial use. Therefore, several regression models such as and SVM [104-108]should be considered when conducting the measurements.

Overfitting issue can be observe when using a test set to evaluating different settings to determine 'hyper-parameters' (e.g., the C coefficient), which must be manually set for an SVM [109] for regression models, as parameters can be altered during training until a given estimator performs optimally. To solve this problem, another part of the dataset

should formed as a so-called 'validation set' [110]. Rather, training proceeds on the training set, and then evaluations are performed on the validation set. When the experiment appears to be successful, a final evaluation (i.e., testing) can be performed on the test set [110]. However, by partitioning the available data into three sets, we drastically reduced the number of samples that can be used to learn the model, and the results can depend on a particular degree of random choice for the pair of (train, validation) sets.

Cross-validation (CV for short) serves as another solution to this dilemma [111, 112]. A test set should still be created for final evaluation, though a validation set is no longer needed when conducting CV. For this basic approach referred to as *k*-fold CV, the training set is divided into *k* smaller sets. The following procedure is followed for each *k* 'fold': [113, 114]

- a model is trained using the kth of the folds as training data;

- The resulting model is validated for the remaining data (i.e., it is used as a test set to compute a performance measure (e.g., accuracy)).

The performance determined via k-fold cross-validation is the average of the values computed for the loop. While this approach can be computationally expensive, it does not waste excessive amounts of data (as is the case when fixing an arbitrary test set). This constitutes major advantage relative to problems such as those of inverse inference, where the number of samples is very small.

VI.5   Support vector regression

The principle of SVM can be described as follows: a linear decision surface can be constructed in a feature space by mapping input vectors to a very high-dimensional feature space [115]. However, for a given n of training examples $\{x_i, y_i\}$, i= 1,…,n, with d inputs $(x_i \in \mathbf{R}^d)$, several hyper-planes in the $\mathbf{R}^d$ domain with a transform vector ($\mathbf{w}$) can be drawn and be expressed as $\mathbf{w} \cdot \mathbf{x} + b = 0$ to separate the examples into two classes $\{-1, +1\}$. Rather, for all examples in domain $\mathbf{R}^d$, the hyper-plate should cause them to satisfy the following relationship: $y_i((\mathbf{w} \cdot x_i) + b) \geq 1$.

Therefore, SVM, as a supervised learning algorithm, is designed to determine suitable $\mathbf{w}$ and b values to maximize the geometric distance from the hyper-plane to the closest data examples. The distance from the hyper-plane to the closest data examples is also known as 'margin'. An optimal hyper plane can be mathematically obtained as a solution to optimization problems to minimize $\tau(w) = 1/2 \|w\|^2$ subject to $y_i((\mathbf{w} \cdot x_i) + b) \geq 1$, i=1,2, ⋯, l, as the following decision function is well expressed for all data points belonging to either 1 or -1: $f(x) = \text{sign}((\mathbf{w} \cdot \mathbf{x}) + b)$. In cases of regression, f(x) is continued.

The SVM algorithm was constructed based on Chang's LibSVM [116]. Although several researchers [116] have found that SVM may generate superior regression results when the target label has been normalized to a range of between [-1 1] or [-10 10], it has been shown that the root mean square error with a measured coating thickness used as a training label is similar to (and sometimes even better than) the scaled training label once training parameters (e.g., kernel types, kernel degrees and kernel shift coefficients) have been scaled. K-folder cross validation is used to identify the best hyper-parameters in a

space where C varies from 3e-5 to 6e-5 and where gamma varies from 0.15 to 0.17. Based on a 50-step interval in C and a 10-step interval in gamma, when C=3.8e-5 and gamma= 0.17, the SVM performs best through all ten folders than it performs with other C and grammar values. The regression coefficient of the SVM model in turn reaches a value of 0.99. The Root Mean Squared Error (RMSE) for the entire training set is recorded at 0.80 mil on average. The performance of both models is comparable during training. The maximum difference between the predicted and specified coating thicknesses on from SVM is recorded at 2.9 mil.

VI.6   Model testing

As a model over-fits training data (i.e., a model generates a perfect score during training but fails to predict useful information for unknown data), it is always a methodological mistake to determine parameters of a prediction function and to apply them to the same data [50]. To avoid this, a set of data typically referred to as a test set is used [50].

Table VI.2   Coating thickness of the test set

Specified coating thickness (mil)	2.5	5	17.5	22.5
Specified standard variance	0.5	0.5	0.9	1.2
Number of samples	8	6	7	7

On the other hand, it is also impossible to consider all thicknesses varying from 2.5 mil to 22.5 mil, wherein a set of complete unknown data collected from samples with

thicknesses from 5 mil and 12.5 mil is used to test the external validity of SVM models (see Table VI.2).
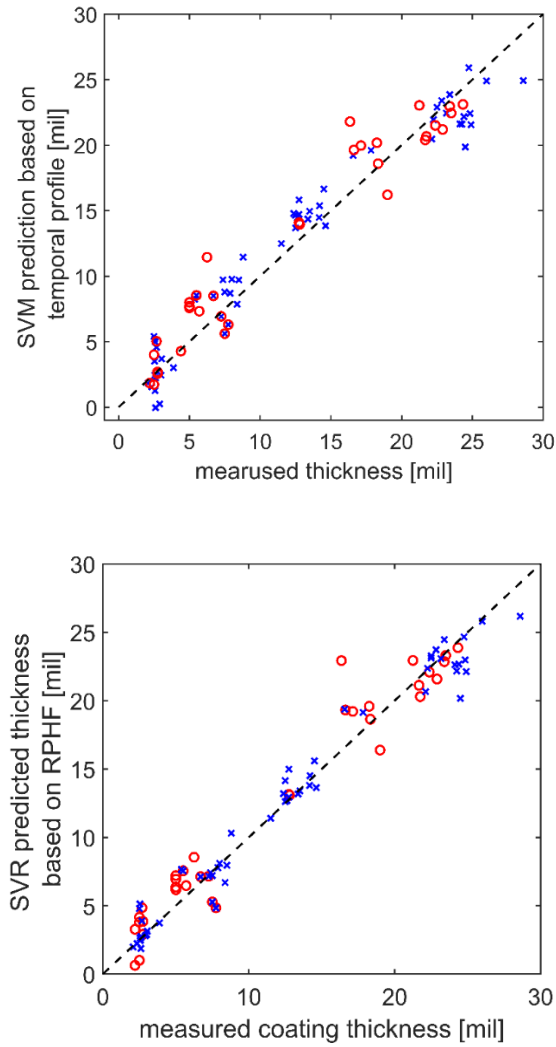
Figure VI.7SVR results based on spatial profile of RPHF vs temperature temporal profile

VI.7 Experiment findings

An analytical expression of surface temperatures is obtained based on Fourier-Hankel transformed mechanisms. Non-dimensional analyses are employed to examine the effects of thermal diffusivity ratios and power amplitudes on surface temperatures. The analysis results show that a decline in the thermal diffusivity ratio may cause a considerable change in non-dimensional temperatures when the conductivity difference between the coating and substrate is significant. Surface temperatures can be used to estimate coating thicknesses when using a relatively stable heating source. SVM and neural network models are developed for various coating thickness and surface temperature increments, which are gathered from 61 painting-coated samples via k-folder cross validation to optimize the model coefficients. The correlation and neural network models are validated with another 28 unknown paint-coated samples. The test results shows (in Figure VI.7) that unlike the temporal profile based inspection patterns, the spatial profile of RPHF are insensitive to the heat flux amplitude change. With 50% variances in heat flux amplitude, the RPHF based SVR model gives a regression coefficient at 0.93 while temporal profile based one gives a value at 0.87. The SVR prediction accuracy dropped from 25.3% to 40.7% when changing the input from spatial profile based data to temporal profile based data.

CHAPTER VII

DEFECT DETECTION ON PLANAR DEFECTS IN CARBON FIBER COMPOSITE[1]

Pulsed Thermography has been considered as a mature NDT technology for defects detection in carbon fiber composite [117-120]. the basic principle of pulse thermography detection lies in the fact that the subsurface defects distort regular flowing of heat fluxes which appear due to either external thermal stimulation or routine object operation [53, 54, 56-58, 121]. The current thermography test standard for carbon fiber composites [120] takes thermal response calculated from 1-D homogeneous heating model under a pulse of heat whose duration is less than 5 microseconds as the reference. In another words, the standard test requires a homogenous heating source and a fast response infrared camera However, there are two issues associated with the practice: an absolute homogeneous heating is almost impossible in real practices and the flashes causes an optical hazard to the inspectors [85, 117, 120, 122-124]. With uneven heating, the results obtained according to standard processes will be biased [56-58, 118-121]. Moreover, the short strong-insensitivity light exploration is uncomfortable, even harmful to human eyes.

To solve the first issue, researchers have contributed a lot of effort in developing different reconstruction methods. Based on whether these processing methods choose a references relative theoretical heat conduction models, they are classified into theoretical

---

processing methods and experimental ones. The experimental ones, like Morphological enveloping filtering[122], principle decompose[123], self-referencing filter[85], and normalizations[124], choose the pseudo background reconstructed based on neighboring area or arbitrary selected area as references.

In this study, we have developed a way to estimate the heat flux at the surface, mentioned as restored Pseudo heat flux (RPHF) in the paper, by using Fourier transform analysis for Inverse heat conduction problems. And we figured out this estimated heat flux RPHF can be used as a detection index for thermography. To demonstrate this, we first built a numerical simulation for the case that using thermography to detecting the back drilled holes in composite boards under equipment noise free condition, and compared the RPHF results with other five existed methods. The numerical method also shows that the end image of RPHF gives a good approximation to the distribution of stimulation heat source. Later, two set experiments are conducted to test the effect of uneven heating and that of thermal diffusivity on RPHF based thermography detection. The comparison shows that proposed method has an advantage in revealing deep buried defects in an earlier time. Comparing to other restoring algorithms, the RPHF shows a better senility to the defect material and depth.

VII.1   Theoretical models and principles

Figure VII.1 shows a general model for planar foreign objects between the plies of carbon fiber composite. The foreign materials are thin planar layers with a thickness at d_1 and width at W. The defects are buried d_0 deep below the exanimated surface. A special condition is considered when a spot heat flux pulse is imposed upon a point on the surface

above defects, where the side boundary of the defect is so far that the heat flux at the side defect boundaries are kept to be zero within a time τ. In this case, the condition described in Figure VII.1a) can be simplified into Figure VII.1 b). A set of heat conduction governing equation can be written:

$$\frac{\partial T_1}{\partial t} = \alpha_{11} \frac{\partial^2 T_1}{\partial x^2} + \alpha_{11} \frac{\partial^2 T_1}{\partial y^2} + \alpha_{12} \frac{\partial^2 T_1}{\partial z^2} \tag{VII.1}$$

$$\frac{\partial T_2}{\partial t} = \alpha_{21} \frac{\partial^2 T_2}{\partial x^2} + \alpha_{21} \frac{\partial^2 T_2}{\partial y^2} + \alpha_{22} \frac{\partial^2 T_2}{\partial z^2} \tag{VII.2}$$

$$\frac{\partial T_3}{\partial t} = \alpha_{11} \frac{\partial^2 T_3}{\partial x^2} + \alpha_{11} \frac{\partial^2 T_3}{\partial y^2} + \alpha_{12} \frac{\partial^2 T_3}{\partial z^2} \tag{VII.3}$$

, with boundary conditions:

$$T_{1,z=d_0} = T_{2,z=d_0} \tag{VII.4}$$

$$k_{12} \frac{\partial T}{\partial z}_{1,z=d_0} = k_{22} \frac{\partial T}{\partial z}_{2,z=d_0} \tag{VII.5}$$

$$T_{1,z=d_0+d_1} = T_{2,z=d_0+d_1} \tag{VII.6}$$

$$k_{12} \frac{\partial T}{\partial z}_{3,z=d_0+d_1} = k_{22} \frac{\partial T}{\partial z}_{2,z=d_0+d_1} \tag{VII.7}$$

$$k_{12} \frac{\partial T}{\partial z}_{1,z=0} (x_0, y_0, 0) = q_0 \tag{VII.8}$$
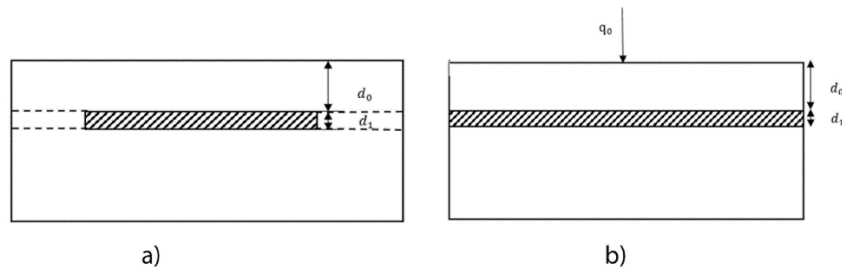
Figure VII.1 **The geometry of tested materials with planar defects inserted in.**

By transforming the equation set above into Fourier Domain, then the partial equation

sets will be converted into linear equation sets:

$$i\omega \bar{T}_1 = \alpha_{11}u^2\bar{T}_1 + \alpha_{11}v^2\bar{T}_1 \, \alpha_{12}\frac{\partial^2 \bar{T}_1}{\partial z^2} \qquad \text{(VII.9)}$$

$$i\omega \bar{T}_2 = \alpha_{21}u^2\bar{T}_2 + \alpha_{21}v^2\bar{T}_2 \, \alpha_{22}\frac{\partial^2 \bar{T}_2}{\partial z^2} \qquad \text{(VII.10)}$$

$$i\omega \bar{T}_3 = \alpha_{11}u^2\bar{T}_3 + \alpha_{11}v^2\bar{T}_3 \, \alpha_{12}\frac{\partial^2 \bar{T}_3}{\partial z^2} \qquad \text{(VII.11)}$$

, where $\bar{T} = \iiint_{-\infty}^{+\infty} T e^{i\omega t} e^{iux} e^{ivy} \, dx dy dt$.

The temperature at top surface of tested samples can be solved:

$$\bar{T}_1 = \frac{q}{k_1\eta_1\sqrt{\frac{i\omega}{\alpha_{11}}+\xi^2}} G(\xi,\omega) \qquad \text{(VII.12)}$$

, where $r = \left(\frac{F_1 k_1 w_1}{F_2 k_2 w_2}\right)$, $F_1 = \sqrt{\frac{i\omega}{\alpha_{11}} + \xi^2}$, $F_2 = \sqrt{\frac{i\omega}{n^2\alpha_{11}} + \xi^2}$, $\xi^2 = u^2 + v^2$, $w_1 = \alpha_{11}/$

a_{12} $w_2 = \alpha_{21}/\alpha_{22}$ and

$$G(\xi,\omega) = \frac{(1+\frac{2e^{2d_0 F_1 w_1}\left(1+e^{2d_1 F_2 w_2}\right)}{\left(-1+e^{2d_1 F_2 w_2}\right)\left(1+e^{2d_0 F_1 w_1}\right)r} + \frac{\left(-1+e^{2d_0 F_1 w_1}\right)}{\left(1+e^{2d_0 F_1 w_1}\right)}r^{-2}}{(\frac{-1+e^{2d_0 F_1 w_1}}{1+e^{2d_0 F_1 w_1}} + \frac{2e^{2d_0 F_1 w_1}\left(1+e^{2d_1 F_2 w_2}\right)}{\left(-1+e^{2d_1 F_2 w_2}\right)\left(1+e^{2d_0 F_1 w_1}\right)} + r^{-2})} \qquad \text{(VII.13)}$$

. Obviously, $G(\xi,\omega)$ is a function relative to the dimensions of defects along the depth

and to the ratio between thermal properties of defects and that of bulk materials.

If the defect is large enough $W \gg d_1$, the heat flux refraction at the side boundaries of

defect can be neglected with in a time τ. That means the heat flux outside the defective

area does not affect the surface temperature inside the defective area， vice versa. If the

heat flux applied to the surface can be described by a function $q(x,y,t)$, then the surface

temperature can be approximated by:

$$\overline{T}_1 \approx \frac{\bar{q}(\xi,\omega)}{k_1\eta_1\sqrt{\frac{i\omega}{\alpha_{11}}+\xi^2}}\overline{G}(\xi,\omega)\overline{f}(\xi) \tag{VII.14}$$

, where $\overline{f}(\xi,\omega)$ is the lateral geometry function of the defects,

$$f(x,y) = \begin{cases} 1, (x,y) \in \Omega_{defect} \\ 0, \ otherelse \end{cases}. \tag{VII.15}$$

A variable, named restored pseudo heat flux (RPHF), can be obtained by doing inverse Fourier transform of the product between the 3D Transformed surface temperature response over a time t and the filter $\sqrt{\xi^2 + \frac{i\omega}{\alpha}}$:

$$\overline{RPHF}(\xi,\omega) \approx \frac{\bar{q}(u,v,\omega)}{k_1\eta_1}\overline{G}(u,v,\omega)\overline{f}(u,v). \tag{VII.16}$$

, in another format:

$$RPHF = \iiint_{-\infty}^{\infty} \frac{\bar{q}(u,v,\omega)}{k_1\eta_1}\overline{G}(u,v,\omega)\overline{f}(u,v)e^{iux}e^{ivy}e^{i\omega t}dudvd\omega \tag{VII.17}$$

The new function, RPHF is a convolution of the lateral geometry and depth temporal-geometric function with the heat flux function.

VII.2   Discussion on the determination of thermal diffusivities and the effect of noises and truncated data

The definition of RPHF in Equation (VII.17) is derived based on the assumption that the tested sample is infinite large in the horizontal planar, which means the heat flux at the boundary is zero in the planar direction. However, restrictedly by the field of view (FOV) of cameras, it cannot be guaranteed that the heat flux at the boundary is zero in the planar direction. Therefore, a truncation error will be brought in and affect the performance of the RPHF. RPHF is not evenly attributed at the boundary of images even though heat flux is even at the boundary at the boundary. To solve this issue, the implantation of RPHF is

adapted based on discrete and spatial truncated surface temperature. Take the function

showing in the Figure VII.2 below as an example:
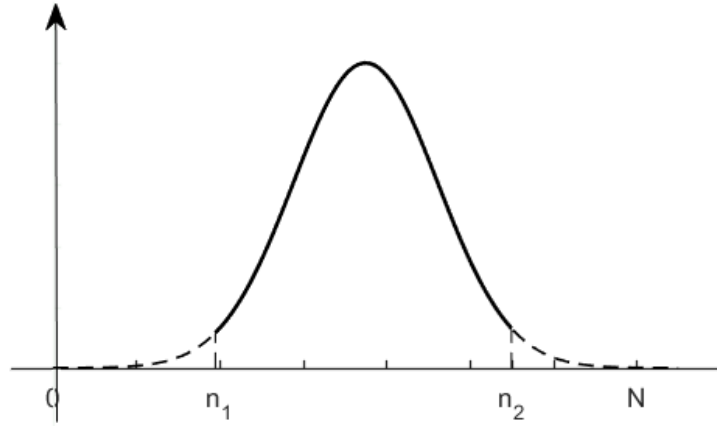
Figure VII.2   Illustration of truncation caused by FOV and introduced phase distortion

At x=0 and x= N, the gradient of function as well as the value of function

approximated to zero. It can be considered that the function shown in Figure VII.2 with

thick dash lines (denoted as $f(x)$) can be considered as a periodical function with a

period N. In this view, the fast Fourier transform of function f(x) , FFT(f(x),j) keeps

constant with its continuous Fourier transform

$$\mathcal{F}(\mathrm{f(x)}, \omega) = \int_{-\infty}^{\infty} f(x) \exp(-ix\omega) \, dx \ = \int_{0}^{NT} f(x) \exp(-ix\omega) \, dx \qquad (\text{VII.18})$$

$$\mathrm{FFT}(\mathrm{f(x)}, \mathrm{j}) = \sum_{k=0}^{N} f(k) \exp(-\frac{2\pi i(k-1)(j-1)}{NT}) \qquad (\text{VII.19})$$

However, due to limited FOV, function f(x) has been truncated into function$f_1(x)$,

shown as the solid line, the fast Fourier transform calculated based on function $f_1(x)$

cannot present the continuous Fourier transform function since:

78

$$\text{FFT}(f_1(x), j) = \sum_{k=n_1}^{n_2} f(k) \exp(-\frac{2\pi i (k-1)(j-1)}{(n_2 - n_1)T}). \qquad \text{(VII.20)}$$

Therefore, another function is constructed as an approximation to the original function $f(x)$, denoted as $f_2(x)$:

$$f_2(x) = \begin{cases} f_1(x) & n_1 \leq x \leq n_2 \\ 0 & otherwise\ of\ [0\ N] \end{cases} \qquad \text{(VII.21)}$$

, or say $f_2(x) = f(x)\Pi\left(\dfrac{x - \frac{N}{2}}{n_2 - n_1}\right)$, where $\Pi(\frac{x}{L})$ stands for a windows function which is centered at x=0 with a width of L .

The fast Fourier transform of function $f_2(x)$ can be expressed as:

$$\text{FFT}(f_2(x), j) = \sum_{k=n_1}^{n_2} f(k) \exp(-\frac{2\pi i (k-1)(j-1)}{NT}). \qquad \text{(VII.22)}$$

It's a better approximation to the continuous Fourier transform of the function $f(x)$ since the phase angle shift is the same with that of $\text{FFT}(f(x), j)$.

In the previous proposed method, RPHF is calculated based on the fast fourier transform of truncated images. Let G(u,v) as the previous proposed frequency domain filter

$$G(u, v, \omega) = \sqrt{u^2 + v^2 + \frac{i\omega}{\alpha}} \qquad \text{(VII.23)}$$

. That means

$$FFT(RHF) \cong \left\{ FFTShift\left(\sum_{k=n_1}^{n_2} f(k) \exp\left(-\frac{2\pi i (k-1)(j-1)}{(n_2 - n_1)T}\right)\right) G(u, v, \omega) \right\} \neq$$

$$\left[\sum_{k=0}^{N} f(k) \exp\left(-\frac{2\pi i (k-1)(j-1)}{NT}\right)\right] G(u, v, \omega). \qquad \text{(VII.24)}$$

That's explains the uneven spatial distribution at the boundary of the image.

To solve this phase shift caused by finite field of view, several revolutions have been proposed in the following paragraphs and their performance have been compared under ideal conditions. The first trial is to define another function $f(x_2)$ based on the original function $f(x_1)$ but extended to a larger field of view to a range where the exact function $f(x)$ converges to zero by reparative padding. By using $\text{FFT}(f_2(x), j)$ instead of $\text{FFT}(f_1(x), j)$, the discretized RPHF can be calculated as :

$$FFT(RPHF) \cong \left\{ \left[\sum_{k=0}^{N} f(k) \exp\left(-\frac{2\pi i(k-1)(j-1)}{NT}\right) \right] * \right.$$

$$\left. \left[\sum_{k=0}^{N} \Pi(k) \exp\left(-\frac{2\pi i(k-1)(j-1)}{NT}\right) \right] \right\} G(u, v, \omega). \tag{VII.25}$$

Still, the revolved RPHF is not approximating to the Heat flux, which is theoretically equal to $\int \int_{-\infty}^{\infty} f(x) \exp(-ix\omega) \, dx \cdot G(\omega) \exp(ix\omega) \, d\omega$.

In the second method, we use $\text{FFT}(f_2(x), j)$ instead of $\text{FFT}(f_1(x), j)$, and define $G_1(\boldsymbol{\omega}) = \sqrt{u^2 + v^2 + \frac{i\omega}{\alpha}} * (\frac{uv}{\sin u \sin v})$. The Fourier transform of RPHF is considered as a product of Fourier transform of $f_2(x)$ and $G_1(\boldsymbol{\omega})$:

$$FFT(RHF) \cong \left\{ FFTShift\left(\sum_{k=n_1}^{n_2} f(k) \exp\left(-\frac{2\pi i(k-1)(j-1)}{NT}\right) \right) \sqrt{u^2 + v^2 + \frac{i\omega}{\alpha}} * \right.$$

$$\left. (\frac{uv}{\sin u \sin v}) \right\}. \tag{VII.26}$$
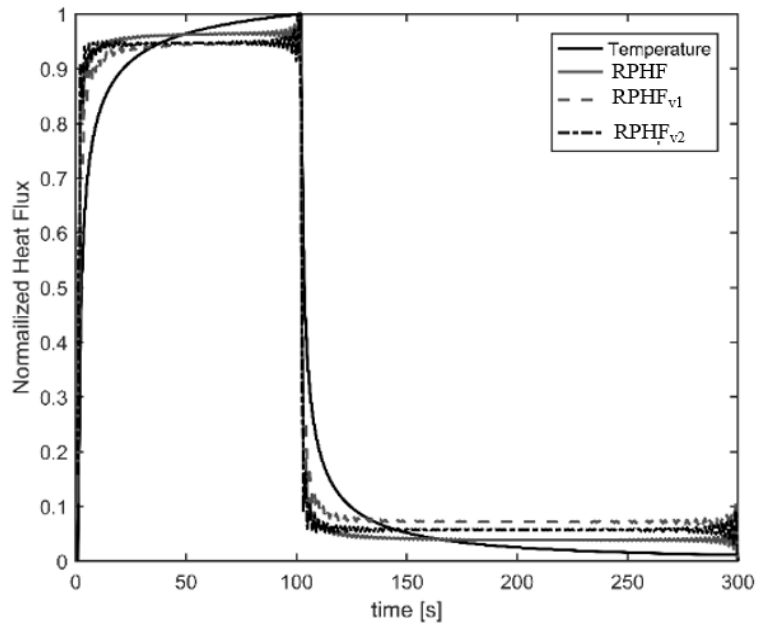
Figure VII.3   Comparison of different revolutions of RPHF in restored temporal profiles

Figure VII.3 shows the temporal profile of restored heat flux by different methods comparing to the input temperature (dash lines) .As the Figure VII.3, the heat flux temporal profile which is restored with the second restoring method exhibit best restoring. With the second restoring method, the profile shows a good approximation to right angle at the point heat flux changing rapidly. As shown in Figure VII.4, the first revolved method shows a better performance than the previous version of restoring method. However, the second revolved method generates a significant aliasing similar to Morrie Patterns (As shown in Figure VII.4).
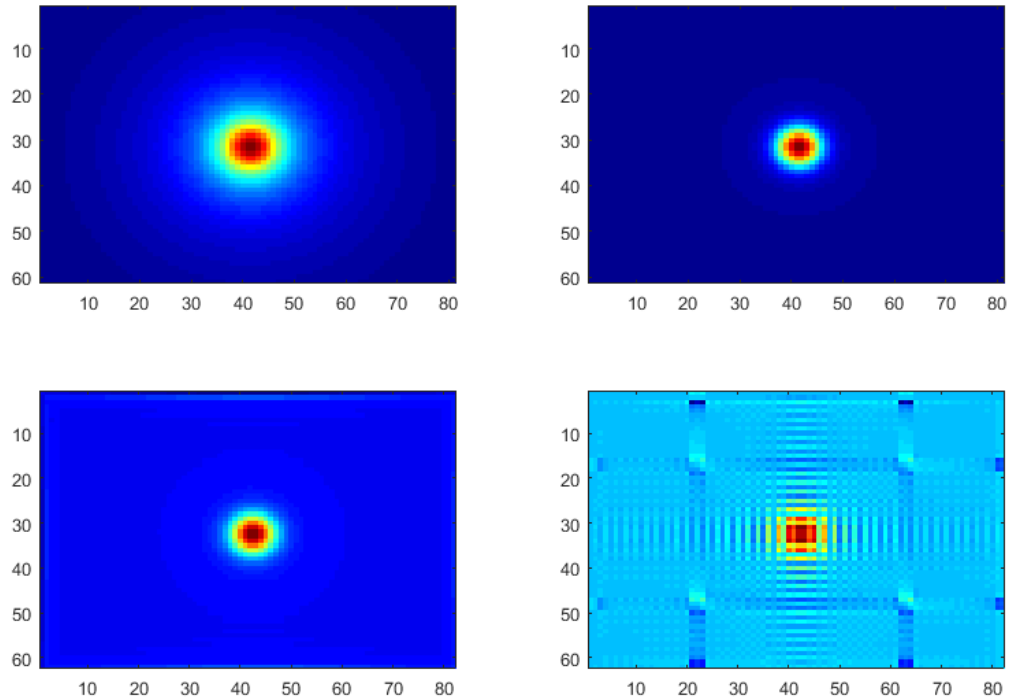
Figure VII.4   Comparison of different revolutions of RPHF in restored spatial profiles

However, all these results are obtained with theoretical simulations. It's not clear whether all these proposed methods will be robust enough for experimental data. Therefore, the proposed methods have been tested with pin-hole data. If there is no smoothing filter applied to the surface temperature, the noises in the restored image are significant when comparing to the defect signals. And the second revolved method provides nothing but aliasing (as shown in Figure VII.4). Therefore, a smoothing filter is chose for the input temperature. After the input temperature has been smoothed by 3 by3 averaging filter, the restored heat flux has been obviously improved in SNR. It can be seen, with the paddings at boundary, the boundary distortion has been reduced.

VII.3   Testing and comparison RPHF with other restoring algorithm based on simulated

data

To testing and comparison the performance of RPHF on eliminating the effect of

uneven heating and on enhancing thermography detection capacity, RPHF are applied to

a set of simulated thermography data. The results are compared to temperature increment

and 4 existed restoring technologies: inverse scattering algorithm proposed by Crowther,

heat flux derivatives along defect depth proposed by Holland, Gaussian Laplacian Filter

proposed by Omar and reconstructed Thermogram.

The aim of the numerical study here is aimed at providing a set of surface temperature

data with zero random noise obtained known and measurable input heat flux. On the other

hand, the true value of heat flux and that of surface temperature are not available during

an experiment.

To achieve this aim and to keep the results from numerical model meaningful in the

real applications, several factors have been considered in the simulation process: uneven

heat flux over the top surface of the tested samples.

The mesh of the simulation area is shown in the Figure VII.5 and Table VII.1. The

simulation zone is proximate to the average size of the samples tested in x and y direction.

The simulations zone is 30.5 mm in width and 30.5 mm in length. The simulated defect

zone is located 4 mm beneath the top surface of the zone with a diameter at 6 mm and 1

mm in thickness. In order to consider in the heat flux leakage at the back surface of the

tested sample, the calculation zone is extended to 20 mm beneath the top surface of the

sample, where the heat flux is approximate to zero after 160s heating based on the

theoretical solution for a non- defective semi carbon fiber bulk with 0.57 mm2/s thermal

diffusion, which is tested based on transient thermal diffusivity testing of the material.

Here, in the simulation, carbon fiber board is simplified as an isotropic material since the

aim of the simulation is to testing the performance of RPHF rather than get a highly

approximation to the surface temperature of carbon fiber board under thermography.

Table VII.1 Properties of materials used in the simulation

CFRB [128]		
Density	1184	Kg/m^3
Cp	298.64	J/Kg-K
Thermal conductivity	2.1	W/m-K
Defects		
Density	840	Kg/m^3
Cp	476	J/Kg-K
Thermal conductivity	0.2	W/m-k
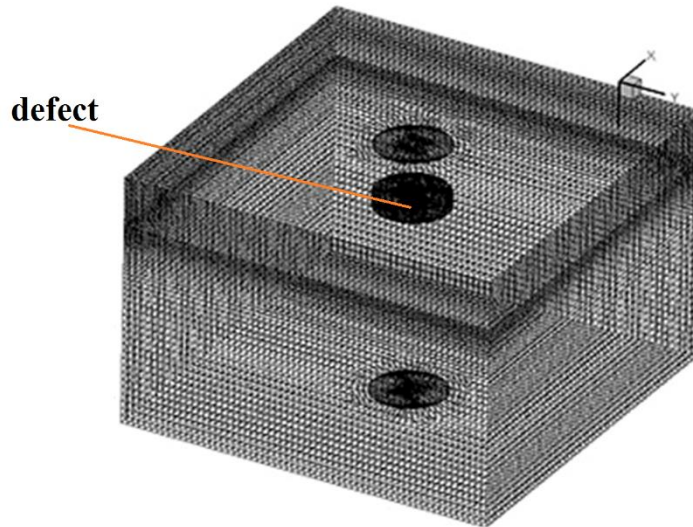
Figure VII.5   The mesh used in simulations

An extremely uneven heating source (shown in Figure VII.10 left), is used in the simulation. Such an uneven heating is hard to available in the real application. But it can help to determine the performance of RPHF to find out thermal property changes by comparing simulated surface temperature to measured surface temperature. The results of RPHF will be compared with other reconstruction methods will be discussed in the section "Analysis and results".

VII.4   Experimental set-ups and samples manufacturing

Two sets of experiments are conducted on two different carbon fiber composite boards with a set-up showing in the Figure VII.6. A Compix 222 infrared camera is set about 65 cm above the surface of the first tested sample and 25cm above the surface of the second tested sample. The Focal Plane Array in the Compix 222 Infrared camera has 160×120 detectors. The instantaneous field of view (IFOV) is 1.81 by 1.81 mm, by using the first set-up described above, and 0.885 by 0.885 mm/ the detectors are sensitive to light ranging

from 7 μm to $14\mu m$. The accuracy of the camera is ±2ºC or 2% whichever is larger. The Noise Equivalent Temperature Difference (NETD) of temperature is 0.1K. The emissivity of the carbon fiber composite has been tested under ASTM code [96]. The emissivity of the surface is 0.93. A 500 W halogen lamp has been used as heating source for both sets of experiments.

The purpose of the first sets of experiment is to test the performance of RPHF under uneven heating source while the second one is aimed at measuring its performance on eliminate the thermal diffusion effect. Therefore, in the first set of experiments, three different heat distribution are created by change the radiance angle between the beam and the tested surface. A thin 4 ply carbon fiber composite are manufactured by wet laying-up method with vacuum bag. With this method, the distribution of the epoxy resin can be control manually to a relative even. The defects inside this samples are inserted in to layers during laying-up. The location and the material of the defects are listed as below. The board has a dimension of 290 x 217mm^2. The gray outline defects are made from 2inch wide (50.8 mm) -6mil (0.152mm) thick copper tape with. The black outline defects are made from 1" (25.4 mm) 6mil (0.152mm) Teflon tape. The size of the defects are drawn in scale in the Figure VII.7 and Table VII.2. The sample has been explored under heating for 65 seconds then follows a 135-second cooling. The images are recorded at a frequency 1 frame per second. The geometry scheme of second sample is shown in Figure VII.8.
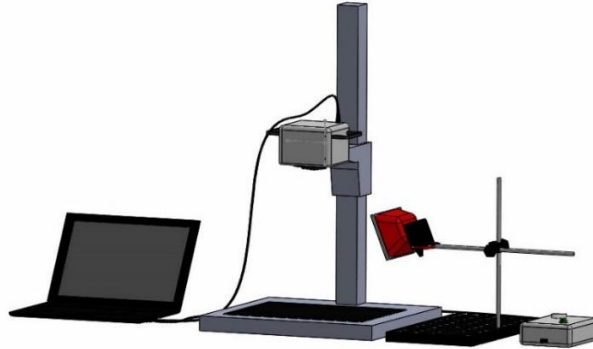
Figure VII.6   Experimental set-up
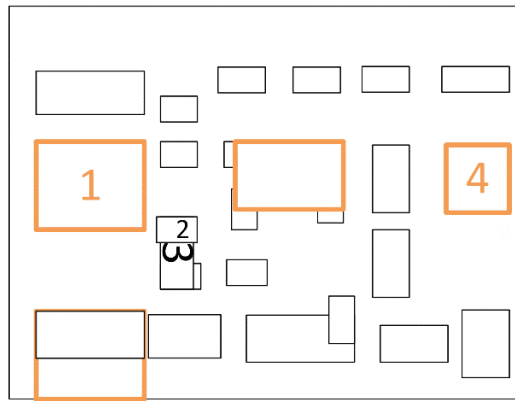
Figure VII.7   The geometric layout of the first sample and heating source distribution

Table VII.2 The heat source distribution used in experiments

	Angle/ degree	distance
set-up 1	42	8"
set-up 2	30	8"
set up 3	90	8"

The second set of experiments are designed to test the performance of RPHF in eliminating the effect of thermal diffusion in both lateral direction and in depth. Therefore, a thicker, 16-ply composite board manufactured with resin-fusion vacuum bag method. As a result, the distribution of resin is uncontrolled. The carbon fiber composite board are anisotropic. An optical image of the board is shown as below. The board is 295mm by 295 mm by 3.5mm in volume. There are six rows of defects cut from 1mil thick FEP, EPL and vinyl resin release sheet. The sheets are cut into about 20mm by 10 mm rectangles. The patch between each column is 55 mm.
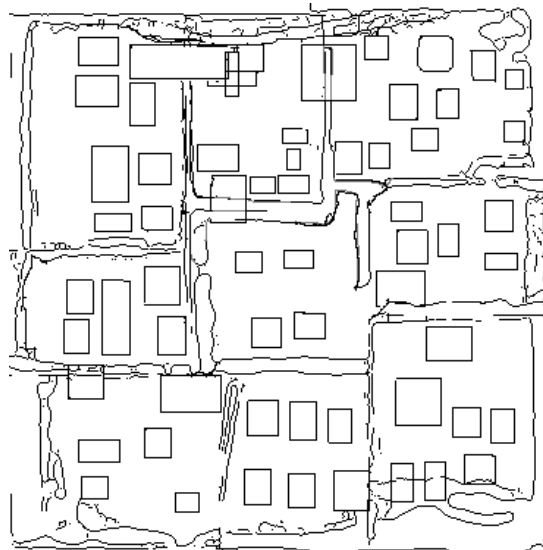
Figure VII.8   The geometric layout of the second sample

VII.5   Analysis and results

This section will analyze the results based on numerical-simulated surface temperature, that sampling from sample 1 and sample 2 separately. All the data are processed following a similar process. The details are documented in the following.

During all the process of the data simulated by numerical data, a normalization based on first image is applied to all the other five reconstruction methods as their author suggested except the RPHF. The RPHF data are normalized by its last image rather than first image. The Figure VII.9 compares the RPHF with the other reconstruction methods mentioned above based on the simulation data. It can be observed that expect the reconstructed Log-scaled temporal derivatives of surface temperature, all the other five reconstruction method display a surface distribution which is close to that of heat flux at an early time (t<30s) although normalization is applied. Meanwhile, Shepard's reconstruction data is affected by uneven heat as well although its distribution is dissimilar
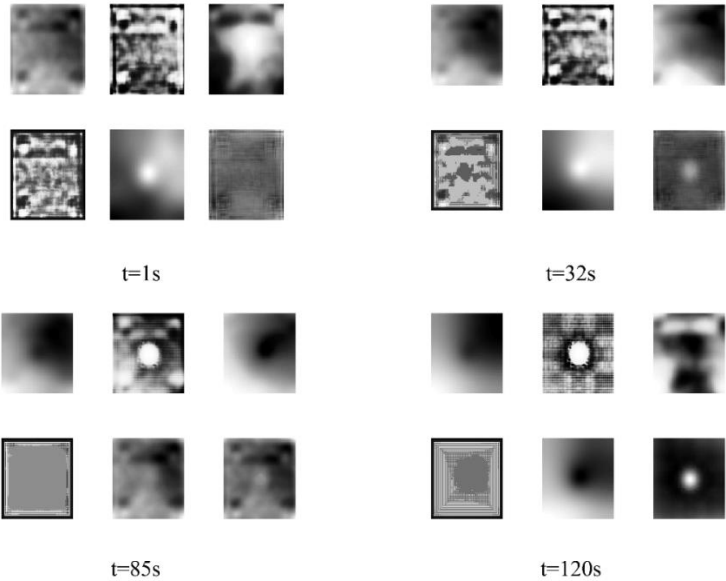
Figure VII.9   Comparison of different reconstruction methods based on simulated data under uneven heating at t=85s (left three column) and t=100s (right three column), top left: normalized surface temperature, mid—Holland heat flux , right—Crowther's inverse scattering method, bottom left – Omar's Gaussian Laplacian filter, mid—Shepard's reconstructed log-scaled first order temporal derivatives, right--- restore pseudo heat flux

89

Figure VII.10   Comparison the estimated heat flux distribution from RPHF (mid) with original heat flux for simulation (left) by using image structural similarity index (right)

with that of heating source. As early as 35 second after heating begins, the defect shape is relieved clearly from RPHF images while its shape stays blur with other reconstruction methods. In addition, RPHF advantages over other reconstruction method by giving a heating-source-independent testing results after the heating is off. (As shown in Figure VII.9) As one of the purpose of numerical simulation is to understand how well the proposed method, RPHF, estimates the input flux, the similarity between the estimated heat flux and the original input is shown in Figure VII.10. It shows that the estimated heat flux from decayed RPHF achieves a 0.93 SSIM value while its maximum is one.

Signal to Noise Ration, (SNR), is a frequently used index to measure performances of reconstruction methods. However, due to the natural of thermography, it won't be possible to evaluate the real random noise in real practices; neither it will be possible to be affected by random noise from measurement equipment in a numerical simulation. Therefore, to considering in the effect of uneven heating, the SNR used here are calculated based on such a way: the signal is determined as the difference between the local standard deviation within defective area and the histogram max of index from non-defective area, the noise

is evaluated from variance of local standard deviation of non-defective area. Such a definition will be useful for real application: if a method give a high SNR, then that means it provide a clear boundary between the defect and non-defective area by using local standard deviation. Figure VII.11 shows the SNR comparison between different reconstruction methods. It can be observed that the SNR from RPHF are increasing as heating goes on. It decrease somehow as the bubble heated into a relative stable period. Once the heat is turned off, the SNR from RPHF method increase significantly for this case.
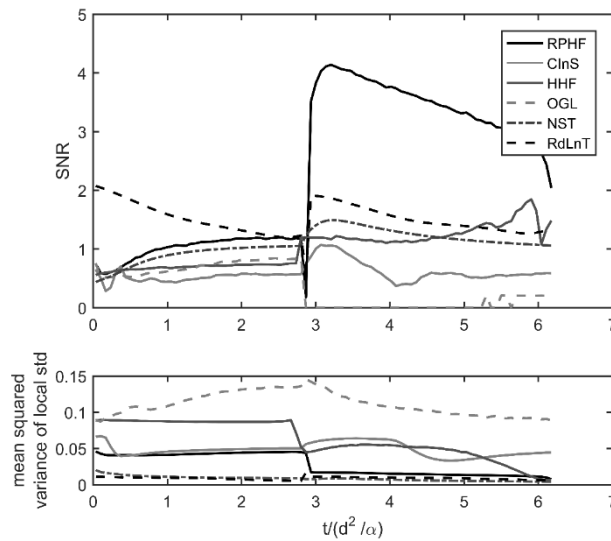
Figure VII.11   SNR from different reconstruction methods based on numerical simulation data

Except the SNR, the computation cost of each method should be considered in real practices. As it requires linear regression along time for the surface temperature of each pixel, the computation coast for Shepard's reconstruction is significantly large. For all the

other methods, the computation coast are comparable to each other. (As shown in Table.VII.3)

Table.VII.3 Comparison of computation cost of different reconstruction methods

	NST	HHF	CIS	OGL	RLndT	RPHF
Calculation Cost /s	0.03	2.359	2.913	0.914	1574.46	1.936

Figure VII.12 and Figure VII.13 compare different reconstruction method under three uneven heating. It can be found that the defects made from copper can be easily detected with a simple normalization. However, the uneven heating degrades testing results with NIST, RdLnT, Cis, and OGL significantly. HHF and RPHF performs similar to each other under different degree of uneven heating although there are some small differences between the results obtained from the same reconstruction method but different uneven heating. For example, with a relative even heating, it can be easily identify four small Teflon defects buried next the left column of copper tapes. With a server uneven heating, only two of them are observed at t=15s. For this set of experiments, as all the defects are shallow buried, Holland's Heat flux provide best contrast to the Teflon tape defects. However, the contrast difference obtained from HHF between Teflon tape defects and copper tape defect does not differ each as much as that from RPHF. The SNR of each method for defects buried at different depth and made from different materials are compared in Figure VII.14.

t=15s

t=65s

a)   b)
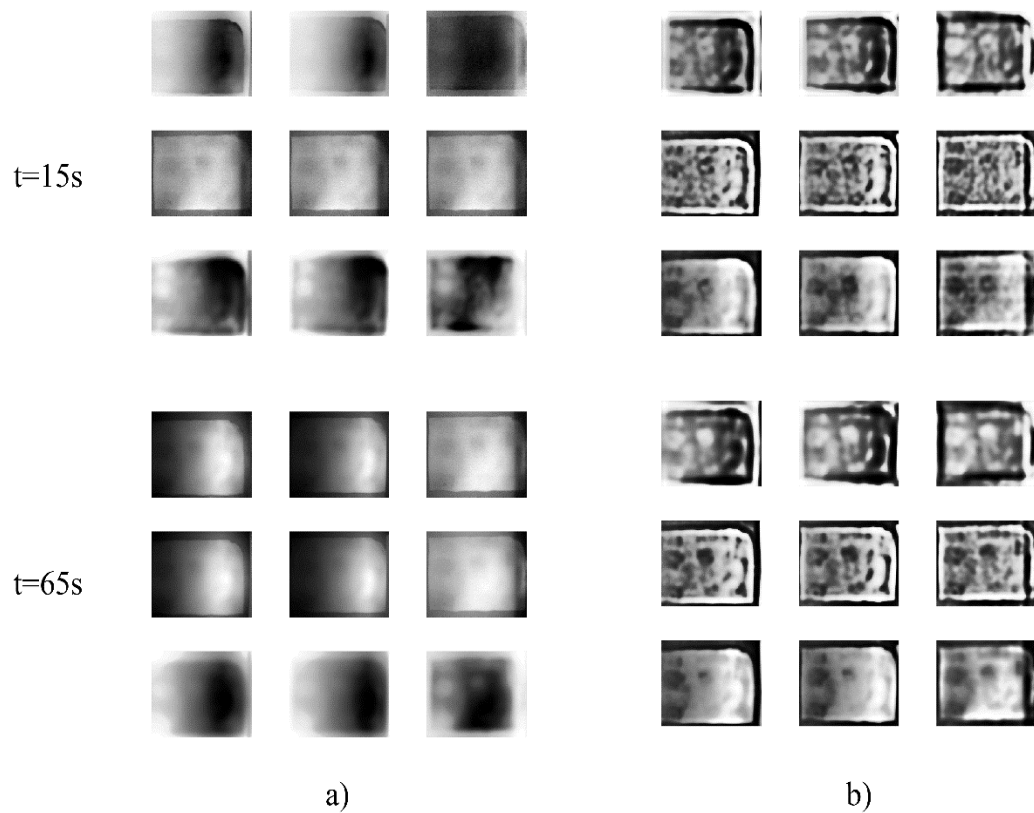
Figure VII.12   Comparison different reconstruction methods under 3 different uneven heating sets: a) Top row—normalized surface temperature, mid row—Shepard's reconstructed log-scaled temporal temperature derivatives, bottom row --- Crowther's inverse scattering algorithm at extremely uneven heating (left) , moderate uneven heating (mid) and near even heating(right); b) Top row—Omar's Laplacian Gaussian, mid row—Holland's heat flux, bottom row --- restored pseudo heat flux at extremely uneven heating (left) , moderate uneven heating (mid) and near even heating(right) at t =15s and t =65s

.

t=75s

t=120s

a)   b)
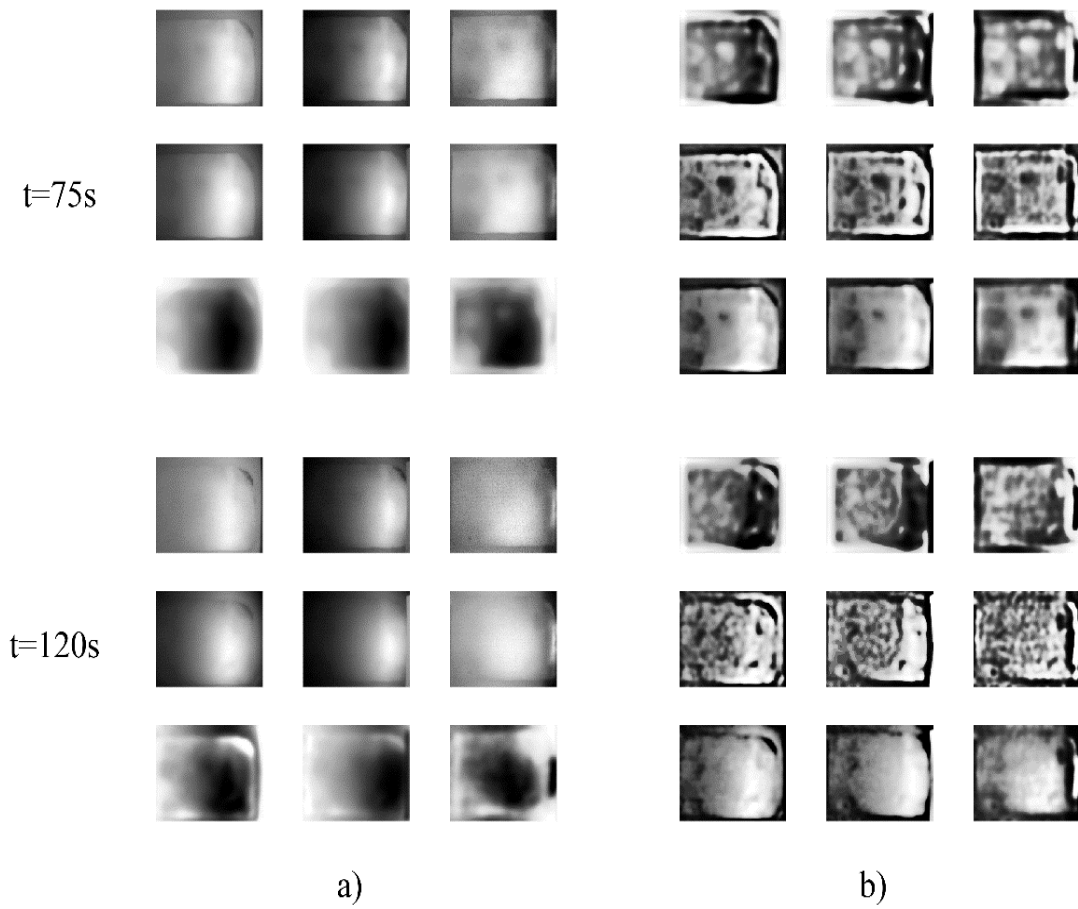
Figure VII.13   Comparison different reconstruction methods under 3 different uneven heating sets: a) Top row—normalized surface temperature, mid row—Shepard's reconstructed log-scaled temporal temperature derivatives, bottom row --- Crowther's Inverse scattering algorithm; b) Top row—Omar's Laplacian Gaussian, mid row—Holland's heat flux, bottom row --- restored pseudo heat flux at extremely uneven heating (left), moderate uneven heating (mid) and near even heating (right) at t=120s

94
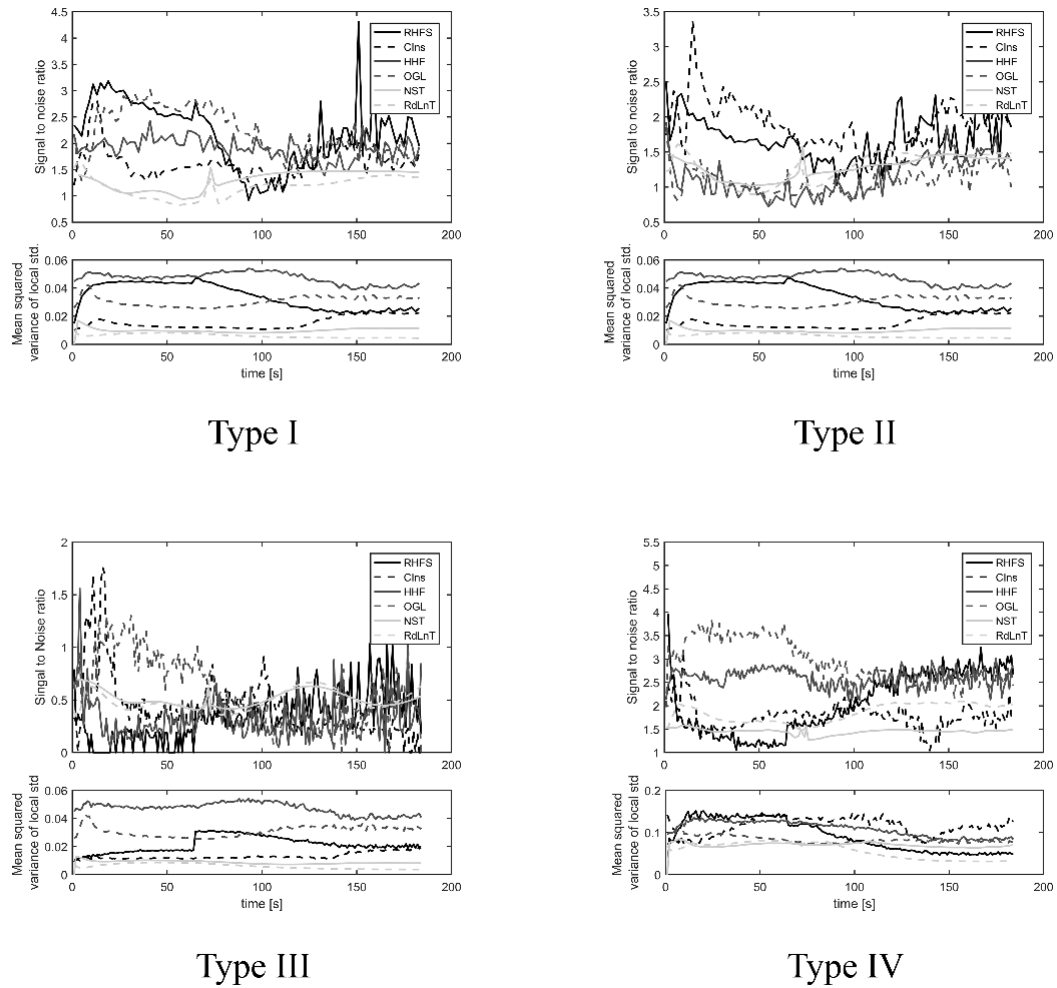
Figure VII.14   Comparison SNR of different reconstruction methods at copper tape (left) and Teflon tape defects (right) buried at different depth

Figure VII.15 compares the six reconstruction results based on experimental data form the second sample. As to achieve a sufficient IFOV, the surface of the board is sectored into 9 areas and a separate testing has been conducted to each area. Then, all the nine images are blundered together according to their position and geometric. Both RPHF and Holland's heat flux gives a good contrast for the shallow buried defects. However, when

comparing the contrast for the deep buried defects in the middle section, and those in the

top right and bottom right corner, RPHF gives a better contrast with obviously less noises.

t=4s   t=8s

t=16s   t=120s
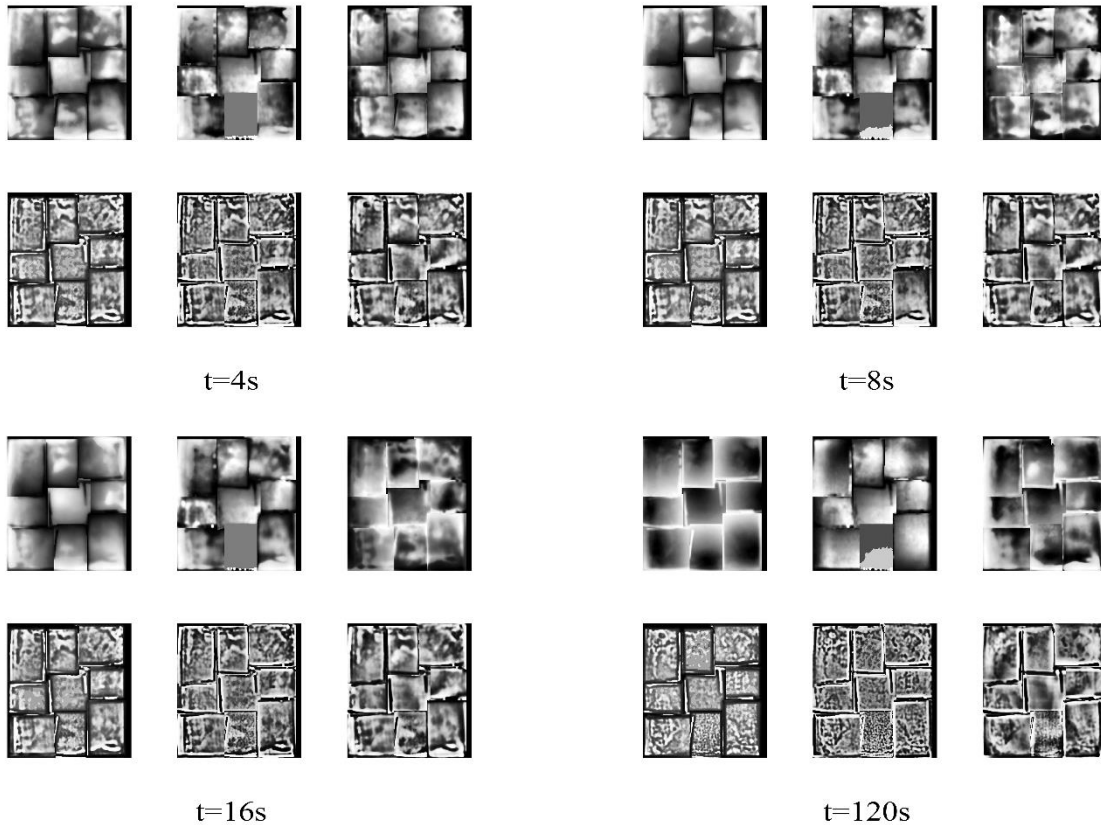
**Figure VII.15   Comparison different reconstructing method top row –
normalized surface temperature (left), Shepard's reconstructed Log-scaled
temperature derivatives (mid), Crowther's inverse scattering algorithm (right);
bottom row—Omar's Gaussian Laplacian filter (left), Holland heat flux (mid) and
restored pseudo heat flux(right) at t =16**

Another very useful information has been obtained from the RPHF method. The last

image of RPHF has been found to be a good inverse image of heating source spatial

distribution (as shown in Figure VII.16). In addition, this image has been used as mask

96

for the surface temperature normalization. It has shown that amount of defects not shown in NIT, which is normalized by the first image of surface temperature. However, no matter the proposed method, or the method existed, neither of them are developed to enhance the detection performance by using human judge but to improve the defection performance based on edge detection. Therefore, a set of machine learning and edge detection process are used, the results are listed in Table VII.4 and Table VII.5.

Table VII.4 False negative and false positive rate for sample 1

		NST	RLndTdt	Crowther's	GOL	Holland (modified)	RPHF (Proposed)
Set 1	FN	23	20	13	7	2	4
	FP	0	0	0	2	2	2
Set 2	FN	22	22	12	9	3	2
	FP	0	0	2	4	4	2
Set 3	FN	20	20	20	7	3	2
	FP	0	0	0	5	4	2

Table VII.5 False negative and false positive rate for sample 2

		NST	RLndTdt	Crowther's	GOL	Holland (modified)	RPHF (Proposed)
Set 1	FN	60	60	38	29	30	17
	FP	0	0	0	2	2	5
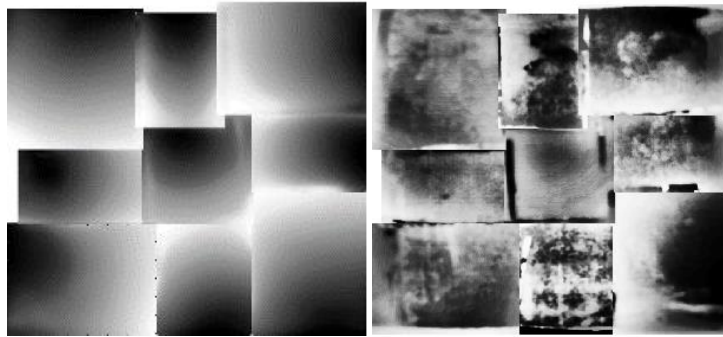
Figure VII.16   Inverse distribution of heat flux in spatial calculated by RPHF (left) and the enhanced surface temperature normalized based on it (right)

VII.6   Summaries

In this test, the proposed reconstruction method has been developed based on the Fourier analysis of heat conduction process. Its performance has been compared to five other commonly used reconstruction methods both numerically and experimentally. The RPHF reconstructed images provide a better contrast than the early time normalized surface temperature, Crowther' inverse scattering method[125] and Shepard's reconstructed temporal temperature derivatives in the case we tested. The RPHF gives a testing result comparable to those from Holland's heat flux and Omar's Gaussian Laplacian filter. Holland's method does give the best contrast to the shallow defects.

However, the RPHF gives a good contrast to the deep buried ones. Unlike OGL or HHF, the contrast of RPHF images varies along time when the defects' depth are different. Moreover, the end RPHF image in a temporal sequence provide a good approximation to the heating source distribution.

CHAPTER VIII

THE SUMMARIES OF RESULTS AND FUTURE WORK

The research are conducted to reduce the effect of two unavoidable effects which decrease the credibility of thermography detection: the uneven heating and the lateral diffusion. The current study has proposed a spatial-temporal profile based restoring reconstruction by evaluating the heat flux deposited onto tested samples based on surface temperature gathered under idea condition at each moment. Then the proposed reconstruction method are tested on three extended condition – on semi-transparent material, on semi-infinite defects (coatings) and on anisotropic materials. The method is evaluated by quality metrics and compared with exist methods. We conclude that the proposed method an efficient performance/ computation cost ratio in all the reconstruction method reviewed in the paper. It reduce the effect of uneven heating by providing a good approximation to the input heat flux at the ending image of the sequence. In the following, detailed findings from each test are explained.

VIII.1   Study 1: testing the pin holes on AR film

Based on the comparison the STD over FOV, global SNR and local SNR between the restored heat flux images, de-trended data and the normalized surface temperature increment images, it can be found that:

The restored heat flux images and the de-trended images give a better uniformity in non-defective area than the normalized surface temperature increment when the heating source is not located in the FOV.

Both the RPHF and de-trended images give a better local SNR and global SNR than the normalized surface temperature increment. As the De-trended data only contains white noise in the background area, de-trended data gives best global SRN in all the test. However, RPHF gives a global SNR at the same order of those from de-trend data.

RPHF gives a lower false positive rate than the de-trended data. However, RPHF may fails in the sub-pixel detection for pinholes with diameter at 0.08mm.

RPHF shows a better performance when a λ shape crack combined on a round blind hole. The de-trended filter created heavy alias and external patterns which misguide the edge detection results.

Comparing on the computation time, the de-trend filter takes 220s to compute on I7 4700 process computers while it takes less than 0.5 seconds for the restored heat flux.

VIII.2   Study 2: the coating thickness study

The statics testing results between the restored heat flux spatial profiles from samples with different coating thickness differs from each other at the inflection point next to the peak

The normalized restored heat flux spatial profile is tested to be independent from the amplitude of the heat source while the temporal patterns are sensitive to it.

The SVR regression has been set up based on both the RPHF and normalized temperature with 50% heat flux variances. The spatial profile based results shows a better r.m.s.e. and regression coefficient than that based on temporal profile based data.

However, the coating thickness variance in the horizontal direction is not discussed in the study yet.

The effect of uncertainty of thermal diffusivity on the restored heat flux should either be studied experimentally or theoretically.

VIII.3   Study 3: planar defects detection in carbon fiber composite detection

The proposed method has an efficient performance/ computation cost ratio in all the reconstruction method reviewed in the paper.

In the carbon fiber composite planar defect testing, the proposed method shows least false positive and false negative testing.

The numerical testing shows the proposed method are robust to at least 50% thermal diffusivity variance to 5000% heating amplitude variance in coating thickness estimation when the temporal based patterns only handling a 50% amplitude variance in coating thickness estimation

Comparing to temperature based methods, the proposed method, like other restoring methods, are less sensitivity to the uneven heat flux

In fact, the method itself provides a good approximation to the heat flux distribution at the end of its temporal sequence.

This approximation to the heat flux distribution can even greatly enhance the detection capacity of surface temperature.

In the Future direction, the detection of subpixel pinholes should be studied and characterized. The current method may not be applicable to thermal-graded materials since the research assumes that a defective area is an area where the thermal properties are different from others. Modified Holland's method has a better SNR than RPHF in shallowly buried defects. This can be explained by the nature of modified Holland's

method in Fourier Hankel domain. It equals to apply RPHF twice to a sample. The RPHF currently shows a better detection in finding deeply buried thin planar defects than other tested methods (including modified Holland's method) and give a relative earlier detection comparing to Shepard's reconstruction and normalized surface temperature. However, it requires further understanding about the relationship between RPHF and buried depth.

REFERENCES

[1]   Kegelmeyer Jr, W. P.,"Method and apparatus for detecting a desired behavior in digital image data", 1997, US Patent, US5633948 A.

[2]   Giorleo, G., and Meola, C., 2002, "Comparison between pulsed and modulated thermography in glass–epoxy laminates," NDT & E International, 35(5), pp. 287-292.

[3]   Marks, L. S., and Baumeister, T., 1922, Mechanical engineers' handbook, McGraw-Hill, New York, United States.

[4]   Fitzgerald, A. J., Cole, B. E., and Taday, P. F., 2005, "Nondestructive analysis of tablet coating thicknesses using terahertz pulsed imaging," Journal of Pharmaceutical Sciences, 94(1), pp. 177-183.

[5]   Dörner, K.-H., Ehbing, H., Hässler, C., Ramthun, J., Stollwerck, G.*, et al.*," Solar modules with a transparent polyurethane front side and a process for producing same," 2006, US Patent, US20020148496 A1.

[6]   Halmshaw, R., Honeycombe, R., and Hancock, P., 1991, Non-destructive testing, E. Arnold, London, UK.

[7]   Bray, D. E., and Stanley, R. K., 1996, Nondestructive evaluation: A tool in design, manufacturing and service, CRC Press, Boca Raton, FL, United States.

[8]   Thomas, A. D., Rodd, M. G., Holt, J. D., and Neill, C., 1995, "Real-time industrial visual inspection: A review," Real-Time Imaging, 1(2), pp. 139-158.

[9]   Harris, B., 1980, "Accumulation of damage and non destructive testing of composite materials and structures," Annales de Chemie--Sciance de Materiaux, 5, pp. 327--339.

[10]   Scott, I. G., and Scala, C. M., 1982, "A review of non-destructive testing of composite materials," NDT International, 15(2), pp. 75-86.

[11]   Carriveau, G. W., 2002, "Non-destructive evaluation and characterization of complex composite structures.", Nondestructive Characterization of Materials XI: Proceedings of the 11th International Symposium, Berlin, Germany, pp. 273-280.

[12]   Stock, S., 2008, "Recent advances in x-ray microtomography applied to materials," International Materials Reviews, 53(3), pp. 129-181.

[13] Rose, J. L., 2002, "A baseline and vision of ultrasonic guided wave inspection potential," Journal of Pressure Vessel Technology, 124(3), pp. 273-282.

[14] Vary, A., and Bowles, K. J., 1979, "An ultrasonic-acoustic technique for nondestructive evaluation of fiber composite quality," Polymer Engineering & Science, 19(5), pp. 373-376.

[15] Heckman, R., 1973, "Finite pulse-time and heat-loss effects in pulse thermal diffusivity measurements," Journal of Applied Physics, 44(4), pp. 1455-1460.

[16] Connolly, M. P., 1991, "A review of factors influencing defect detection in infrared thermography: Applications to coated materials," Journal of Nondestructive Evaluation, 10(3), pp. 89-96.

[17] Omar, M., Hassan, M., and Saito, K., 2005, "Optimizing thermography depth probing with a dynamic thermal point spread function," Infrared Physics & Technology, 46(6), pp. 506-514.

[18] Schulze, M. H., Heuer, H., Küttner, M., and Meyendorf, N., 2010, "High-resolution eddy current sensor system for quality assessment of carbon fiber materials," Microsystem Technologies, 16(5), pp. 791-797.

[19] Prakash, R., 1980, "Non-destructive testing of composites," Composites, 11(4), pp. 217-224.

[20] Bull, D., Helfen, L., Sinclair, I., Spearing, S., and Baumbach, T., 2013, "A comparison of multi-scale 3D X-ray tomographic inspection techniques for assessing carbon fibre composite impact damage," Composites Science and Technology, 75, pp. 55-61.

[21] Gros, X., Ogi, K., and Takahashi, K., 1998, "Eddy current, ultrasonic c-scan and scanning acoustic microscopy testing of delaminated quasi-isotropic CFRP materials: A case study," Journal of Reinforced Plastics and Composites, 17(5), pp. 389-405.

[22] Sun, G., Zhou, Z., Chen, X., and Wang, J., 2013, "Ultrasonic characterization of delamination in aeronautical composites using noncontact laser generation and detection," Applied Optics, 52(26), pp. 6481-6486.

[23] Chambers, A., Earl, J., Squires, C., and Suhot, M., 2006, "The effect of voids on the flexural fatigue performance of unidirectional carbon fibre composites developed for wind turbine applications," International Journal of Fatigue, 28(10), pp. 1389-1398.

[24]   Prakash, R., 1981, "Significance of defects in the fatigue failure of carbon fibre reinforced plastics," Fibre Science and Technology, 14(3), pp. 171-181.

[25]   Meola, C., Carlomagno, G. M., and Giorleo, L., 2004, "Geometrical limitations to detection of defects in composites by means of infrared thermography," Journal of Nondestructive Evaluation, 23(4), pp. 125-132.

[26]   Zauner, G., Mayr, G., and Hendorfer, G., 2009, "Wavelet-based subsurface defect characterization in pulsed phase thermography for non-destructive evaluation," IS&T/SPIE Electronic Imaging, San Jose, CA, United States, pp. 72480D-72488.

[27]   Sripragash, L., Smith, C., Kumaran, G., and Sundaresan, M., 2013, "Monitoring damage development around stress raisers in carbon/epoxy laminates", SPIE Smart Structures and Materials+ Nondestructive Evaluation and Health Monitoring, San Diego, CA, United States, pp. 869404-869408.

[28]   Rantala, J., Wu, D., and Busse, G., 1998, "NDT of polymer materials using lock-in thermography with water-coupled ultrasonic excitation," NDT & E International, 31(1), pp. 43-49.

[29]   Mayr, G., Plank, B., Sekelja, J., and Hendorfer, G., 2011, "Active thermography as a quantitative method for non-destructive evaluation of porous carbon fiber reinforced polymers," NDT & E International, 44(7), pp. 537-543.

[30]   Patel, P., Lau, S., and Almond, D., 1992, "A review of image analysis techniques applied in transient thermographic nondestructive testing," Nondestructive Testing and Evaluation, 6(6), pp. 343-364.

[31]   Sun, J. G., 2009, "Thermal imaging characterization of thermal barrier coatings," Advanced ceramic coatings and interfaces ii: Ceramic and Engineering Science Proceedings, volume28, issue 3, Uwe Schulz, and Zhu, eds., John Wiley & Sons, Inc., Hoboken, NJ, United States, pp. 53-60.

[32]   Lim, T., Ratnam, M., and Khalid, M., 2007, "Automatic classification of weld defects using simulated data and an MLP neural network," Insight-Non-Destructive Testing and Condition Monitoring, 49(3), pp. 154-159.

[33]   Meola, C., Carlomagno, G. M., Squillace, A., and Vitiello, A., 2006, "Non-destructive evaluation of aerospace materials with lock-in thermography," Engineering Failure Analysis, 13(3), pp. 380-388.

[34]   Vavilov, V., Kauppinen, T., and Grinzato, E., 1997, "Thermal characterization of defects in building envelopes using long square pulse and slow thermal wave

techniques," Journal of Research in Nondestructive Evaluation, 9(4), pp. 181-200.

[35] Mulaveesala, R., and Tuli, S., 2006, "Theory of frequency modulated thermal wave imaging for nondestructive subsurface defect detection," Applied Physics Letters, 89(19), pp. 191913-191916.

[36] Straube, H., Breitenstein, O., and Wagner, J. M., 2011, "Thermal wave propagation in thin films on substrate: The time-harmonic thermal transfer function," Physica Status Solidi (B), 248(9), pp. 2128-2141.

[37] Wang, H., Hsieh, S.-J., Zhou, X., Peng, B., and Singh, B., 2015, "Using active thermography to inspect pin-hole defects in anti-reflective coating with k-mean clustering," NDT & E International, 76, pp. 66-72.

[38] Newman, T. S., and Jain, A. K., 1995, "A survey of automated visual inspection," Computer Vision and Image Understanding, 61(2), pp. 231-262.

[39] Carslaw, H. S., and Jaeger, J. C., 1959, Conduction of heat in solids, 2nd, Clarendon Press, Oxford, United Kingdom.

[40] Salazar, A., 2006, "Energy propagation of thermal waves," European Journal of Physics, 27(6), p. 1349.

[41] Hartnett, J. P., and Rohsenow, W. M., 1973, Handbook of heat transfer, McGraw-Hill New York, United States.

[42] Vavilov, V., 2007, "Pulsed thermal NDT of materials: Back to the basics," Nondestructive Testing and Evaluation, 22(2-3), pp. 177-197.

[43] Zweschper, T., Dillenz, A., Riegert, G., Scherling, D., and Busse, G., 2003, "Ultrasound excited thermography using frequency modulated elastic waves," Insight-Non-Destructive Testing and Condition Monitoring, 45(3), pp. 178-182.

[44] Mallick, P. K., 2007, Fiber-reinforced composites: Materials, manufacturing, and design, CRC Press, Boca Raton, FL, United States.

[45] Wisnom, M. R., Reynolds, T., and Gwilliam, N., 1996, "Reduction in interlaminar shear strength by discrete and distributed voids," Composites Science and Technology, 56(1), pp. 93-101.

[46] Eyesaver International (n.d.). ,(March,2012),"Anti-reflective coated glass", Eyesaver International (n.d.). , Hanover, MA, United States., http://eyesav erinternational.com/wp-content/uploads/2012/03/ESI_AR_Glass_Data_Sheet.pdf

[47]   Tariq, M., Mahmoud Abdelhamid, Yuntao Li, Mohammed Omar, and Yi Zhou, 2012, "Fusion of thermal and visible acquisitions for evaluating production-borne scratches and shunts in photo-voltaic PV cells," Journal of Materials Science Research 1, 1(4), p. 57.

[48]   Dexerials Corporation,(2015)," Technical data for antireflection film AR1.5", San Joe, CA, United States, http://www.dexerials.jp/en/products/b1/ar1_5.html.

[49]   Sandia National Laboratories (2000),"Coating on glass technology roadmap workshop.",Sandia National Laboratories, Livermore, CA, United States.

[50]   Ramthun, J. A., Floeder, S. P., Manning, A. T., Harklau, L. L., Kostuch, G. D.*, et al.*,"Low cost thickness measurement method and apparatus for thin coating", June 26, 2001, US Patent, US6252237 B1.

[51]   Liu, B., Zhang, C.-l., Shen, J.-l., Feng, L.-c., Tao, N.*, et al.*, "Nondestructive testing of paint thickness measurement by pulsed infrared thermography," Proc. IRMMW-THz 2006, Shanghai, China, pp. 323.

[52]   Reimche, W., and Duhm, R., 2006, "Non-destructive testing and assessment of coatings," Modern surface technology, Wiley-VCH Verlag GmbH & Co. KGaA, Weinheim, Germany, pp. 297-321.

[53]   Henneke II, E. G., Reifsnider, K. L., and Stinchcomb, W. W., 1979, "Thermography—an NDI method for damage detection," The Journal of The Minerals, Metals & Materials Society, 31(9), pp. 11-15.

[54]   Steinberger, R., Leitão, T. V., Ladstätter, E., Pinter, G., Billinger, W.*, et al.*, 2006, "Infrared thermographic techniques for non-destructive damage characterization of carbon fibre reinforced polymers during tensile fatigue testing," International Journal of Fatigue, 28(10), pp. 1340-1347.

[55]   Vavilov, V., Nesteruk, D., Shiryaev, V., Ivanov, A., and Swiderski, W., 2010, "Thermal (Infrared) tomography: Terminology, principal procedures, and application to nondestructive testing of composite materials," Russian Journal of Nondestructive Testing, 46(3), pp. 151-161.

[56]   Ludwig, N., and Teruzzi, P., 2002, "Heat losses and 3d diffusion phenomena for defect sizing procedures in video pulse thermography," Infrared physics & technology, 43(3), pp. 297-301.

[57]   Baddour, N., 2006, "Fourier diffraction theorem for diffusion-based thermal tomography," Journal of Physics A: Mathematical and General, 39(46), p. 14379.

[58]   Busse, G., Wu, D., and Karpen, W., 1992, "Thermal wave imaging with phase sensitive modulated thermography," Journal of Applied Physics, 71(8), pp. 3962-3965.

[59]   Mulaveesala, R., Arora, V., Siddiqui, J. A., and Muniyappa, A., "Non-stationary thermal wave imaging for nondestructive testing and evaluation," Proc. SPIE Sensing Technology+ Applications, Baltimore, MD, United States, pp. 91050R-91056.

[60]   Mulaveesala, R., and Tuli, S., 2005, "Digitized frequency modulated thermal wave imaging for non-destructive testing," Materials Evaluation, 63(10), pp. 1046-1050.

[61]   Mulaveesala, R., Vaddi, J. S., and Singh, P., 2008, "Pulse compression approach to infrared nondestructive characterization," Review of Scientific Instruments, 79(9), p. 094901.

[62]   Avdelidis, N. P., Almond, D. P., Dobbinson, A., Hawtin, B., Ibarra-Castanedo, C., *et al.*, 2004, "Aircraft composites assessment by means of transient thermal NDT," Progress in Aerospace Sciences, 40(3), pp. 143-162.

[63]   Patel, P., Almond, D., and Reiter, H., 1987, "Thermal-wave detection and characterisation of sub-surface defects," Applied Physics B, 43(1), pp. 9-15.

[64]   Osiander, R., and Spicer, J. W., 1998, "Time-resolved infrared radiometry with step heating. A review," Revue Générale de Thermique, 37(8), pp. 680-692.

[65]   Erturk, H., 2011, "Evaluation of image reconstruction algorithms for non-destructive characterization of thermal interfaces," International Journal of Thermal Sciences, 50(6), pp. 906-917.

[66]   Vavilov, V. P., 2014, "Modeling thermal NDT problems," International Journal of Heat and Mass Transfer, 72, pp. 75-86.

[67]   Vavilov, V. P., 2015, "Dynamic thermal tomography: Recent improvements and applications," NDT & E International, 71, pp. 23-32.

[68]   Rajic, N., 2002, "Principal component thermography for flaw contrast enhancement and flaw depth characterisation in composite structures," Composite Structures, 58(4), pp. 521-528.

[69]   Shepard, S. M., Lhota, J. R., Rubadeux, B. A., Wang, D., and Ahmed, T., 2003, "Reconstruction and enhancement of active thermographic image sequences," Optical Engineering, 42(5), pp. 1337-1342.

[70]   Quek, S., Almond, D., Nelson, L., and Barden, T., 2005, "A novel and robust thermal wave signal reconstruction technique for defect detection in lock-in thermography," Measurement Science and Technology, 16(5), p. 1223.

[71]   Wang, H., and Hsieh, S.-J., 2015, "Comparison of step heating and modulated frequency thermography for detecting bubble defects in colored acrylic glass ", Thermosense: Thermal Infrared Applications XXXVII, 9485, Baltimore, MD, United States, pp. 94850I:94851-94811.

[72]   Zainal Abidin, I., Yun Tian, G., Wilson, J., Yang, S., and Almond, D., 2010, "Quantitative evaluation of angular defects by pulsed eddy current thermography," NDT & E International, 43(7), pp. 537-546.

[73]   Holland, S. D., and Renshaw, J., 2010, "Physics-based image enhancement for infrared thermography," NDT & E International, 43(5), pp. 440-445.

[74]   Omar, M. A., and Zhou, Y., 2008, "A quantitative review of three flash thermography processing routines," Infrared Physics & Technology, 51(4), pp. 300-306.

[75]   Delpueyo, D., Balandraud, X., and Grédiac, M., 2013, "Heat source reconstruction from noisy temperature fields using an optimised derivative Gaussian filter," Infrared Physics & Technology, 60, pp. 312-322.

[76]   Maldague, X., and Marinetti, S., 1996, "Pulse phase infrared thermography," Journal of Applied Physics, 79(5), pp. 2694-2698.

[77]   Lugin, S., and Netzelmann, U., 2007, "A defect shape reconstruction algorithm for pulsed thermography," NDT & E International, 40(3), pp. 220-228.

[78]   Pickering, S., and Almond, D., 2008, "Matched excitation energy comparison of the pulse and lock-in thermography NDE techniques," NDT & E International, 41(7), pp. 501-509.

[79]   Bisson, J., and Fournier, D., 1998, "Influence of diffraction on low thermal diffusivity measurements with infrared photothermal microscopy," Journal of Applied Physics, 83(2), pp. 1036-1042.

[80]   Cernuschi, F., Bison, P., Figari, A., Marinetti, S., and Grinzato, E., 2004, "Thermal diffusivity measurements by photothermal and thermographic techniques," International Journal of Thermophysics, 25(2), pp. 439-457.

[81]   Balageas, D. L., 2012, "Defense and illustration of time-resolved pulsed thermography for NDE," Quantitative Infrared Thermography Journal, 9(1), pp. 3-

32.

[82]   Balageas, D. L., "Defense and illustration of time-resolved thermography for NDE," Proc. Thermo-sense XXXIII, Orlando, FL, United States pp. 22-33.

[83]   Shepard, S., and Ducar, R. J., "Quantitative infrared defect detection in composite aerospace structures," Proc. SAMPE 2000: 45th International SAMPE Symposium and Exhibition, Long Beach, CA, United States, pp. 1282-1290.

[84]   Omar, M., Parvataneni, R., and Zhou, Y., 2010, "A combined approach of self-referencing and principle component thermography for transient, steady, and selective heating scenarios," Infrared Physics & Technology, 53(5), pp. 358-362.

[85]   Omar, M., Hassan, M., Saito, K., and Alloo, R., 2005, "Ir self-referencing thermography for detection of in-depth defects," Infrared Physics & Technology, 46(4), pp. 283-289.

[86]   Meola, C., Di Maio, R., Roberti, N., and Carlomagno, G. M., 2005, "Application of infrared thermography and geophysical methods for defect detection in architectural structures," Engineering Failure Analysis, 12(6), pp. 875-892.

[87]   Dixon, W. J., and Massey, F. J., 1969, Introduction to statistical analysis, McGraw-Hill New York.

[88]   Motulsky, H., and Christopoulos, A., 2004, Fitting models to biological data using linear and nonlinear regression: A practical guide to curve fitting, Oxford University Press, New York.

[89]   Shapiro, S. S., and Wilk, M. B., 1965, "An analysis of variance test for normality (complete samples)," Biometrika, 52(3/4), pp. 591-611.

[90]   Stephens, M. A., 1974, "Edf statistics for goodness of fit and some comparisons," Journal of the American Statistical Association, 69(347), pp. 730-737.

[91]   Razali, N. M., and Wah, Y. B., 2011, "Power comparisons of shapiro-wilk, kolmogorov-smirnov, lilliefors and anderson-darling tests," Journal of Statistical Modeling and Analytics, 2(1), pp. 21-33.

[92]   ASTM E1933-14,(2005),"Standard test methods for measuring and compensating for emissivity using infrared imaging radiometers," West Conshohocken, PA, United States.

[93]   Arthur, D., and Vassilvitskii, S., 2007, "K-means++: The advantages of careful seeding," Proceedings of the eighteenth annual ACM-SIAM symposium on

Discrete algorithms, New Orleans, LA, USA, pp. 1027-1035.

[94]   Spath, H., 1985, "Cluster dissection and analysis: Theory, FORTRAN programs, examples. Horwood," Halsted Press [distributor], Chichester, New York.

[95]   Duda, R. O., and Hart, P. E., 1973, Pattern classification and scene analysis, John Wiley & Sons, Ltd, New York.

[96]   ASTM   E1933-99a,(2010),"Standard   test   methods   for   measuring   and compensating for emissivity using infrared imaging radiometers", ASTM, West Conshohocken, PA, United States.

[97]   Mathworks, I., 2014, " Matlab documentation center: Image analysis," Mathworks, ed.Mathworks, Inc..

[98]   Hsieh, S.-J., Rash, C. E., Harding, T. H., Beasley, H. H., and Martin, J. S., 2003, "Helmet-mounted display image quality evaluation system," Instrumentation and Measurement, IEEE Transactions on, 52(6), pp. 1838-1845.

[99]   Poularikas, A. D., 2010, Transforms and applications handbook, CRC Press, Berlin, Germany.

[100]   Moorhead, M. S., 2009, "Estimating the thermal properties of thin film and multilayer   structures   using   photothermal   deflection   spectroscopy,"   Ph.d dissertation, Cornell University, Ithaca, NY, United States.

[101]   Bison, P., Cernuschi, F., Grinzato, E., Marinetti, S., and Robba, D., 2007, "Ageing evaluation of thermal barrier coatings by thermal diffusivity," Infrared Physics & Technology, 49(3), pp. 286-291.

[102]   Ringermacher, H. I., Archacki Jr, R. J., and Veronesi, W. A.,"Nondestructive testing: Transient depth thermography", 1998, US Patent, US5711603 A.

[103]   Holleck, H., Lahres, M., and Woll, P., 1990, "Multilayer coatings—influence of fabrication   parameters   on   constitution   and   properties,"   Surface   and   Coatings Technology, 41(2), pp. 179-190.

[104]   Thissen, U., Van Brakel, R., De Weijer, A., Melssen, W., and Buydens, L., 2003, "Using support vector machines for time series prediction," Chemometrics and Intelligent Laboratory Systems, 69(1), pp. 35-49.

[105]   Al-Balushi, K., and Samanta, B., 2002, "Gear fault diagnosis using energy-based features of acoustic emission signals," Proceedings of the Institution of Mechanical Engineers, Part I: Journal of Systems and Control Engineering, 216(3), pp. 249-

263.

[106] Mohandes, M., Halawani, T., Rehman, S., and Hussain, A. A., 2004, "Support vector machines for wind speed prediction," Renewable Energy, 29(6), pp. 939-947.

[107] Huang, C.-L., Chen, M.-C., and Wang, C.-J., 2007, "Credit scoring with a data mining approach based on support vector machines," Expert Systems with Applications, 33(4), pp. 847-856.

[108] Acharya, U. R., Ng, E., Tan, J.-H., and Sree, S. V., 2012, "Thermography based breast cancer detection using texture features and support vector machine," Journal of Medical Systems, 36(3), pp. 1503-1510.

[109] Tay, F. E., and Cao, L., 2001, "Application of support vector machines in financial time series forecasting," Omega, 29(4), pp. 309-317.

[110] Huang, G.-B., Zhu, Q.-Y., and Siew, C.-K., 2006, "Extreme learning machine: Theory and applications," Neurocomputing, 70(1), pp. 489-501.

[111] Hsu, C.-W., Chang, C.-C., and Lin, C.-J., 2003, "A practical guide to support vector classification,"https://www.csie.ntu.edu.tw/~cjlin/papers/guide/guide.pdf, pp. 1-16.

[112] Varma, S., and Simon, R., 2006, "Bias in error estimation when using cross-validation for model selection," BMC Bioinformatics, 7(1), p. 1.

[113] Duan, K., Keerthi, S. S., and Poo, A. N., 2003, "Evaluation of simple performance measures for tuning SVM hyperparameters," Neurocomputing, 51, pp. 41-59.

[114] Lei, M., Shiyan, L., Chuanwen, J., Hongling, L., and Yan, Z., 2009, "A review on the forecasting of wind speed and generated power," Renewable and Sustainable Energy Reviews, 13(4), pp. 915-920.

[115] Vapnik, V., and Cortes, C., 1995, "Support vector networks," Machine Learning, 20, pp. 273-297.

[116] Chang, C.-C., and Lin, C.-J., 2011, "Libsvm: A library for support vector machines," ACM Transactions on Intelligent Systems and Technology (TIST), 2(3), p. 27.

[117] Swiderski, W., "The characterization of defects in multi-layered composite materials by thermal tomography methods," Proc. Proceedings of the Tenth Annual Conference of the Materials Research Society of Serbia, Herceg Novi,

Montenegro, pp. 800-804.

[118]   Meola, C., and Toscano, C., 2012, "Nondestructive evaluation of carbon fiber reinforced polymers with ultrasonics and infrared thermography: An overview on historical steps and patents," Recent Patents on Materials Science, 5(1), pp. 48-67.

[119]   ASTM E1934-99a,(2014),"Standard guide for examining electrical and mechanical equipment with infrared thermography," ASTM International, West Conshohocken, PA, United States.

[120]   ASTM E2582-07,(2014)," Standard practice for infrared flash thermography of composite panels and repair patches used in aerospace applications", ASTM International, West Conshohocken, PA, United States.

[121]   Vavilov, V. P., Nesteruk, D. A., Shiryaev, V. V., Ivanov, A., and Swiderski, W., 2010, "Thermal (Infrared) tomography: Terminology, principal procedures, and application to nondestructive testing of composite materials," Russian Journal of Nondestructive Testing, 46(3), pp. 151-161.

[122]   Usamentiaga, R., Venegas, P., Guerediaga, J., Vega, L., and López, I., 2013, "Automatic detection of impact damage in carbon fiber composites using active thermography," Infrared Physics & Technology, 58, pp. 36-46.

[123]   Valluzzi, M., Grinzato, E., Pellegrino, C., and Modena, C., 2009, "IR thermography for interface analysis of FRP laminates externally bonded to RC beams," Materials and Structures, 42(1), pp. 25-34.

[124]   Usamentiaga, R., Venegas, P., Guerediaga, J., Vega, L., and López, I., 2013, "A quantitative comparison of stimulation and post-processing thermographic inspection methods applied to aeronautical carbon fibre reinforced polymer," Quantitative Infrared Thermography Journal, 10(1), pp. 55-73.

[125]   Crowther, D., Favro, L., Kuo, P., and Thomas, R., 1993, "Inverse scattering algorithm applied to infrared thermal wave images," Journal of applied physics, 74(9), pp. 5828-5834.

[126]   Minkina, W., and Dudzik, S., 2009, "Uncertainties of measurements in infrared thermography," Infrared thermography: Errors and uncertainties, Dudzik, ed., John Wiley & Sons, Ltd, Chichester, West Sussex, PO19 8SQ, United Kingdom, pp. 81-135.

[127]   ASTM E1933-14,(2014), "Standard test method for calibration and accuracy verification of wideband infrared thermometers," ASTM International, West Conshohocken, PA, United States.

APPENDIX A

PUBLICATIONS

Published Journal Paper:

Wang, Hongjin, Sheng-Jen Hsieh, and Alex Stockton. "Evaluating the performance of artificial neural networks for estimating the nonmetallic coating thicknesses with time-resolved thermography." *Optical Engineering* 53.8 (2014): 083102-083102.

Wang, Hongjin, Hsieh, Sheng-jen et al. "Using active thermography to inspect pin-hole defects in anti-reflective coating with k-mean clustering." *NDT & E International* 76 (2015): 66-72.

Wang, Hongjin, Hsieh, Sheng-jen et al. "Non-Metallic Coating Thickness Prediction Using Artificial Neural Network and Support Vector machine with Time Resolved Thermography." *Infrared Physics and Technology*. (2016)

Conference Papers:

Wang, Hongjin, Sheng-Jen Hsieh, and Bhavana Singh. "Detection of pinhole defects in optical film using thermography and artificial neural network." SPIE Sensing Technology+ Applications. International Society for Optics and Photonics, 2015.

Wang, Hongjin, and Sheng-Jen Hsieh. "Comparison of step heating and modulated frequency thermography for detecting bubble defects in colored acrylic glass." SPIE Sensing Technology+ Applications. International Society for Optics and Photonics, 2015.

APPENDIX B

SOLVE THE HEAT CONDUCTION GOVERNING EQUATION IN 3D USING

THE HANKEL TRANSFORM

The heat conduction governing equation can be expressed as following after the Laplace transform applied in time and after the Hankel transform applied in space:

$$\frac{s}{\alpha_1} v_1 + \xi^2 v_1 = \frac{\partial^2 v_1}{\partial z^2} \tag{B.1}$$

$$\frac{s}{\alpha_1} v_2 + \xi^2 v_2 = \frac{\partial^2 v_2}{\partial z^2} \tag{B.2}$$

With boundary conditions set as:

$$-k_1 \frac{\partial v_1}{\partial z}(z = z_0) = \bar{q}(s, \xi) = A \frac{1}{2s} \exp\left(-\frac{\xi^2 B^2}{8}\right) / 4\pi R^2 \tag{B.3}$$

$$v_1(0) = v_2(0) \tag{B.4}$$

$$k_1 \frac{\partial v_1}{\partial z}(0) = k_2 \frac{\partial v_2}{\partial z}(0) \tag{B.5}$$

$$k_2 \frac{\partial v_2}{\partial z}(-\infty) = 0 \tag{B.6}$$

Eq.s (A.1) and (A.2) are solved using:

$$v_1 = A \exp\left(-z \sqrt{\xi^2 + \frac{s}{\alpha_1}}\right) + B \exp\left(z \sqrt{\xi^2 + \frac{s}{\alpha_1}}\right) \tag{B.7}$$

$$v_2 = B_2 \exp\left(-z \sqrt{\xi^2 + \frac{s}{\alpha_1}}\right) + A_2 \exp\left(z \sqrt{\xi^2 + \frac{s}{\alpha_1}}\right) \tag{B.8}$$

According to (B.6):

$$B_2 = 0 \tag{B.9}$$

By adding (B.7) (B.8) and (B.9) to Eq. (B.3) (B.4) and (B.5), the following equations are obtained:

$$A \exp\left(-z_0\sqrt{\xi^2 + \frac{s}{\alpha_1}}\right) - B \exp\left(z_0\sqrt{\xi^2 + \frac{s}{\alpha_1}}\right) = \frac{\bar{q}(s,\xi)}{k\sqrt{\xi^2 + \frac{s}{\alpha_1}}} \tag{B.10}$$

$$A + B = A_2 \tag{B.11}$$

$$(B - A) = \frac{k_2\sqrt{\xi^2 + \frac{s}{\alpha_2}}}{k_1\sqrt{\xi^2 + \frac{s}{\alpha_1}}} A_2 \tag{B.12}$$

When Eq. (B.11) is added to Eq. (B.12), A and B are expressed as:

$$B = \left(1 + \frac{k_2\sqrt{\xi^2 + \frac{s}{\alpha_2}}}{k_1\sqrt{\xi^2 + \frac{i\omega}{\alpha_1}}}\right) A_2/2 \tag{B.13}$$

$$A = \left(1 - \frac{k_2\sqrt{\xi^2 + \frac{s}{\alpha_2}}}{k_1\sqrt{\xi^2 + \frac{s}{\alpha_1}}}\right) A_2/2 \tag{B.14}$$

Define $R(\xi, s)$ as the ratio between A and B:

$$R(\xi) = \frac{A}{B} = \frac{\sqrt{\xi^2 + \frac{s}{\alpha_1}} - \chi\sqrt{\xi^2 + n^2\frac{s}{\alpha_1}}}{\sqrt{\xi^2 + \frac{s}{\alpha_1}} + \chi\sqrt{\xi^2 + n^2\frac{s}{\alpha_1}}} \tag{B.15,}$$

where $\chi = \frac{k_2}{k_1}$ and $n = \frac{\alpha_2}{\alpha_1}$.

Add Eq B.14) (B.13) and (B.15) to Eq. (B.10):

$$A\left(1/R - \exp\left(-2z_0\sqrt{\xi^2 + \frac{s}{\alpha_1}}\right)\right) = \frac{\bar{q}(\omega,\xi)\exp\left(-z_0\sqrt{\xi^2 + \frac{s}{\alpha_1}}\right)}{k\sqrt{\xi^2 + \frac{s}{\alpha_1}}} \tag{B.16}$$

$$A = \frac{\bar{q}(s,\xi)\,\text{R}\exp\left(-z_0\sqrt{\xi^2 + \frac{s}{\alpha_1}}\right)}{k\sqrt{\xi^2 + \frac{s}{\alpha_1}}\left(1 - R\exp\left(-2z_0\sqrt{\xi^2 + \frac{s}{\alpha_1}}\right)\right)} \tag{B.17}$$

117

$$B = \frac{\bar{q}(s,\xi) \exp\left(-z_0\sqrt{\xi^2+\frac{s}{\alpha_1}}\right)}{k\sqrt{\xi^2+\frac{s}{\alpha_1}}\left(1-R\exp\left(-2z_0\sqrt{\xi^2+\frac{s}{\alpha_1}}\right)\right)} \tag{B.18}$$

$$v_1 = \frac{\bar{q}(\omega,\xi)\,R\exp\left(-(z+z_0)\sqrt{\xi^2+\frac{s}{\alpha_1}}\right)}{k\sqrt{\xi^2+\frac{s}{\alpha_1}}\left(1-R\exp\left(-2z_0\sqrt{\xi^2+\frac{s}{\alpha_1}}\right)\right)} + \frac{\bar{q}(s,\xi)\exp\left((z-z_0)\sqrt{\xi^2+\frac{s}{\alpha_1}}\right)}{k\sqrt{\xi^2+\frac{s}{\alpha_1}}\left(1-R\exp\left(-2z_0\sqrt{\xi^2+\frac{s}{\alpha_1}}\right)\right)} \tag{B.19}$$

At the surface of coating $z = z_0$, one can obtained:
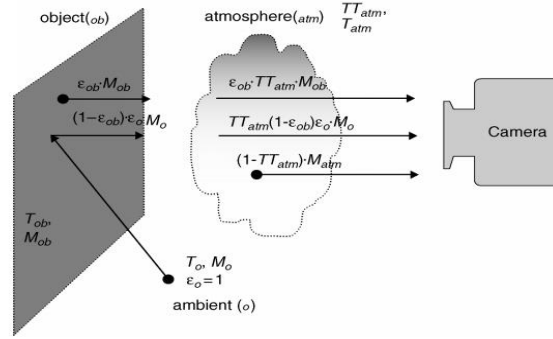
$$v_1 = \frac{\bar{q}(\omega,\xi)\left(1+R\exp\left(-2z_0\sqrt{\xi^2+\frac{s}{\alpha_1}}\right)\right)}{k\sqrt{\xi^2+\frac{s}{\alpha_1}}\left(1-R\exp\left(-2z_0\sqrt{\xi^2+\frac{s}{\alpha_1}}\right)\right)} \tag{B.20}$$

APPENDIX C

CALIBRATION OF INFRARED CAMERA WITH BLACK BODY METHOD

The energy transformation between the detectors and the measured object can be typically illustrated as the figure below [126]. The energy absorbed by a micro-bolometer, s, can be expressed by the sum of radiant heat from several source[126]:

Figure AIII-0.1 Interaction of the radiation fluxes in measurement with an infrared camera cited from Minkina's book [126](copyright2009 by J Wiley & sons,), reprinted with permission

$$s = \varepsilon_{ob} \cdot TT_{atm}s_{ob} + TT_{atm}(1 - \varepsilon_{ob})s_o + (1 - TT_{atm}) \tag{C.1},$$

where s stands for radiant heat signals, ε stands for emissivity, and TT_{atm} stands for the transparency. The subscripts ob and o stands for measured objects and environment respectively.

Signal s_o can be calculated according to the model below:

$$s_o = \frac{R}{\exp\left(\frac{B}{T_0}\right) - F} \tag{C.2},$$

where R, B, F are constants. As the infrared camera are Long-wave IR camera which

sensitive to the IR with wave length from $8\text{-}14\,\mu m$, the R, B, F are determined by manufactories.

Therefore, the object's temperature can be evaluated as:

$$S_{ob} = S\frac{1}{\varepsilon_{ob}TT_{atm}} - [\frac{1-\varepsilon_{ob}}{\varepsilon_{ob}}\frac{R}{\exp\left(\frac{B}{T_0}\right)-F} + \frac{1-TT_{atm}}{\varepsilon_{ob}TT_{atm}}\frac{R}{\exp\left(\frac{B}{T_0}\right)-F}].$$ (C.3)

$$T_{ob} = \frac{B}{Ln\left(\frac{R}{S_{ob}}+F\right)}, K.$$ (C.4)

Based on The equation above, the infrared camera measurement model is defined as a function of ε_{ob}, TT_{atm}, T_o, R, B, and F.

The expanded uncertainty of the IR camera measured objective temperature can be calculated from the sum of chain derivatives of these factors.

The IR camera calibration is quite similar to that calibrates a calibrating an Infrared Thermometers [126, 127].The first scheme described in the ASTM Code E2847-14 has been applied . A flat heating source is used. The setting up of the experiment is shown as figure below. Used sensor, heating source are listed in the table as well. The thermal couple readings are averaged with 3 sequential reading within a second. And the thermal couple is calibrated at ice-water and boiling water points.

Table AIII-1 The sensors, heating source used

Heating source	**Tokai Hit OLYMPUS thermo plate**	**Guaranteed Temperature variance at 'steady state'**	**+/-0.1 C**
Thermocouple	T type	Uncertainty	+/-0.1 C

Figure AIII-0.2 The set-up of calibration experiments

The table below reports standard calibration report suggested by ASTM E E2847-14.

Table AIII-2 The calibration results

Nominal [C]	S. T. [C]	C.T. [C]	d(mm)	Apt.	Source Type	Scheme	Exp. Unct [C]
22.5	22.6	22.6	240	N	Flt. 400x300	I	0.8
27.0	26.8	27.0	240	N	Flt. 400x300	I	0.8
30.0	30.1	30.3	240	N	Flt. 400x300	I	0.9
45.5	45.4	45.3	240	N	Flt. 400x300	I	1.5
52.0	51.6	51.7	240	N	Flt. 400x300	I	1.6

However, more than the accuracy, thermography application are more interested in that how consistency a camera reports the difference between objects with two different

temperature. That means, it requires a good precision in camera readings. Therefore,

reparative readings have been conducted